Understanding the Structure/Property/Processing Inter-relationships in Organic Semiconducting Blends

This thesis is submitted for the degree of

Doctor of Philosophy

at Imperial College London

Department of Physics

Presented by

Paul Westacott

Supervised by Dr. Natalie Stingelin

Sponsored by the Engineering and Physical Science Research Council

Declaration of originality

"The work that is presented within this thesis is original and was conducted by myself, literature reviews and work from others that is reported is referenced. Necessary assistance was kindly given by the staff and students at Imperial College London, University of California Santa Barbara, Université de Montréal and North Carolina State University."

Paul Westacott

Copyright declaration

"The copyright of this thesis rests with the author and is made available under a Creative Commons Attribution Non-Commercial No Derivatives licence. Researchers are free to copy, distribute or transmit the thesis on the condition that they attribute it, that they do not use it for commercial purposes and that they do not alter, transform or build upon it. For any reuse or redistribution, researchers must make clear to others the licence terms of this work"

Abstract

Over the last few years organic semiconductors have seen a dramatic rise in interest from both academia and industry alike. This has been largely due to their promise of low-cost, high-throughput manufacture, combined with many other positive attributes including their: flexibility; semi-transparency and light-weight nature. This combination of factors show that organic semiconductors hold strong potential to compete with inorganic technologies in a number of existing and emerging applications. More specifically, blends comprised of a number organic semiconductors offer significant promise for devices such as organic photovoltaics (OPVs) and organic light emitting diodes (OLEDs), as tuning the chemical nature of the constituting materials can influence the blend's optoelectronic properties. However, during processing, such as blending, complex mixture of phases are formed which renders understanding these systems challenging.

This thesis examines the relationships between the three critical aspects that affect organic semiconducting blends, namely: the processing route selected, the resulting microstructure and, as a consequence, the induced optoelectronic properties. A more comprehensive understanding is developed of how the processing route (solution casting from common solvent *vs.* bilayer fabrication via lamination) can affect the structural formation processes in organic semiconductor systems, such as crystallisation, vitrification *etc.* Additionally, this thesis elucidates how the structural formation processes influence the mixture of phases that evolve and discusses how the microstructure that is created affects the photo-physical processes such as exciton quenching and charge generation, within these systems.

The results within this thesis highlight the sensitive interplay between the three areas of structure, property and processing. Clear insights into how to manipulate these aspects to positively impact the photo-physical processes are conferred. The findings discussed here give, thus, clear guidelines as to how to further enhance understanding and terminally improve the performance of devices such as organic solar cells.

Acknowledgements

Here I would like to express my deep and sincerest gratitude to the people who have helped to make the last three years so hugely enjoyable and productive. Firstly, I would like to thank my supervisor Natalie Stingelin for her continued guidance, motivation, creative input and willingness to let me follow ideas throughout this project. Secondly, I would like to extend my sincere gratitude to all of the academic staff and students whose input has made this project truly possible, there are far too many people to list who have helped and inspired this work, but let's try anyway… The members of the Stingelin group from my first to last day: Gianluca Latini, Manuela Russo, Ester Buchaca-Domingo, Jennifer Nekuda-Malik, Liyango Yu, Christoph Hellmann, Alberto Scaccabarozzi, Neil Treat, Cephas Small and the rest! Additional thanks goes to a number of people whose help and guidance have helped bring everything together. Sarah Fearn, whose assistance and knowledge in all things SIMS has been completely instrumental in completing this thesis. Additionally, Alex Sieval from Solenne BV, as it was only through his openness for collaboration that we have been able to proceed with this work, much of which is ongoing. I would also like to acknowledge the Doctoral Training Centre for Plastic Electronics and all of its members, for providing such a unique academic and social environment over the past four years, which has made the whole time so great. Turning to my family, I'd like to thank my parents for their constant support and for cultivating my academic curiosity, which was one of the key things that lead me to pursue a PhD. Last and certainly not least, I am so thankful to my girlfriend, Natalie (C), your constant understanding; support; patience and encouragement have helped no end to get me through this in one piece!

Scope and survey of thesis

This thesis addresses the structure/property/processing inter-relationships of different semiconductor binary systems in order to develop a more comprehensive understanding of how processing routes can affect the structural formation processes, what the effect of this is on the phase morphology of such systems and, terminally, how this alters the photo-physical properties such as charge generation.

Chapter 1: places in context the recent literature and outlines the challenges related to the three areas of processing, structure and photo-physical processes. **Chapter 2**: summarises the materials and experimental methods utilised in the following chapters. **Chapter 3:** investigates in detail the use of depth profile SIMS within the Plastic Electronics area; outlines the experimental methodology and interpretation of measurements to improve understanding of composition-position within organic semiconducting films; and explains the structural formation processes and resulting phase morphology of multi-component systems. **Chapter 4:** explores intermixed phases in organic BHJs in terms of possible microstructural and photo-physical processes in a prototypical binary of P3HT/PCBM. **Chapter 5:** discusses the role of different fullerenes in the formation of vitrified, kinetically trapped phases, and the resultant effect on device performance in OPV blends. **Chapter 6:** builds upon the understanding gained in Chapters 4 and 5 for polymer:fullerene systems and extends this to polymer/polymer systems. The molecular-weight dependence on the structural formation and macroscopic properties are investigated and clear differences reported between systems. **Chapter 7**: further emphasises the influence of processing on the microstructure and photo-physical properties within all polymer semiconducting blends, especially with respect to energy-transfer processes between the two components.

List of publications

(Correct as of 6th January 2014)

[6] Paul Westacott, Alex Sieval, Neil Treat, Sarah Fearn and Natalie Stingelin. *(to be submitted).*
"The application of SIMS to the Plastic Electronics area"

[5] Paul Westacott, Jonathon Rivnay, Francis Paquin, Mohammed Al-Hashimi, Martin Heeney, Carlos Silva and Natalie Stingelin. *(to be submitted).*
"Controlling energy transfer in polymer-polymer blends"

[4] Paul Westacott, Neil Treat, Mohammed Al-Hashimi, Terry McAfee, Harald Ade, Martin Heeney, Michael Chabinyc and Natalie Stingelin. *(to be submitted)*
"Molecular-weight dependence on structural formation in conjugated polymer-polymer systems"

[3] Paul Westacott, Neil Treat, Sarah Fearn, James Bannock, John deMello, David McPhail, Alex Sieval and Natalie Stingelin. (*to be submitted).*
"Fullerene-induced vitrification of semiconducting polymers directs microstructure and device efficiency"

[2] Paul Westacott, John R. Tumbleston, Safa Shoaee, Sarah Fearn, James H. Bannock, James B. Gilchrist, Sandrine Heutz, John deMello, Martin Heeney, Harald Ade, James Durrant, David S. McPhail and Natalie Stingelin, *Energy and Environmental Science*, **6**, 2756-2764 (2013)
"On the role of intermixed phases in organic photovoltaic blends"

[1] Felix P. V. Koch, Jonathan Rivnay, Sam Foster, Christian Müller, Jonathan M. Downing , Ester Buchaca-Domingo, Paul Westacott, Liyang Yu, Mingjian Yuan, Mohammed Baklar, Zhuping Fei, Christine Luscombe, Martyn A. McLachlan, Martin Heeney, Garry Rumbles, Carlos Silva, Alberto Salleo, Jenny Nelson, Paul Smith and Natalie Stingelin, *Progress in Polymer Science*, **38**, 1978-1989 (2013)
"The impact of molecular weight on microstructure and charge transport in semi-crystalline polymer semiconductors–poly (3-hexylthiophene), a model study"

Table of contents

Declaration of originality 1

Copyright declaration 1

Abstract 2

Acknowledgements 3

Scope and survey of thesis 4

List of publications 5

Table of contents 6

1 Introduction 1

1.1 Background 2

1.1.1 General introduction 2

1.1.2 History of plastic electronics 4

1.1.3 Current challenges: understanding structure/property/processing inter-relationships 9

1.2 OPV operating principle 10

1.2.1 General processes 10

1.2.2 The conventional model for charge generation 10

1.2.3 Different refinements of the theory of charge generation 12

1.2.4 OPV device operation: an electronic perspective 18

1.3 The influence of microstructure 23

1.3.1 Number of phases 23

1.3.2 Nature of phases 25

1.4 Thin film deposition/structure formation 32

1.4.1 Deposition processes 32

1.4.2 Microstructural formation 34

1.4.3 Summary 41

1.5 Scope and survey of thesis 42

1.6 References 43

2 Experimental methods 49
2.1 Materials 50
2.2 Methods 51
2.2.1 Steady-state UV-vis absorption spectroscopy (UV-vis) 51
2.2.2 Steady-state photoluminescence spectroscopy (PL) 52
2.2.3 Transient absorption spectroscopy (TAS) 53
2.2.4 Differential scanning calorimetry (DSC) 54
2.2.5 Wide-angle X-ray scattering (WAXS) 56
2.2.6 Near-edge X-ray absorption fine structure (NEXAFS) 58
2.2.7 Secondary ion mass spectrometry (SIMS) 58
2.2.1 Depth profile – SIMS (D-SIMS) 61
2.3 References 63
3 The application of SIMS to the Plastic Electronics area 65
3.1 Introduction 66
3.2 Understanding binary systems of functional organic materials 69
3.2.1 Blends — RRa-P3HT:D5-PCBM 69
3.2.2 Influence of material selection 76
3.2.3 Bilayers 82
3.3 Conclusions 86
3.4 Materials and methods 87
3.5 References 88
4 The role of intermixed phases in organic photovoltaic blends 91
4.1 Introduction 92
4.2 Results and discussion 95
4.3 Conclusion 109
4.4 Materials and methods 111
4.5 References 114
5 Fullerene-induced vitrification of semiconducting donor polymers 118

5.1 Introduction 119
5.2 Results and discussion 120
5.3 Conclusions 130
5.4 Materials and methods 131
5.5 References 133
6 M_w dependence on structural formation in conjugated polymer-polymer systems 135
6.1 Introduction 136
6.2 Results and discussion 140
6.3 Materials and methods 147
6.4 References 148
7 Energy transfer in polymer-polymer binaries 150
7.1 Introduction 151
7.2 Results and discussion 152
7.3 Conclusions 160
7.4 Materials and methods 161
7.5 References 163
Summary 165
Curriculum vitae 166

Chapter 1

Introduction

1.1 Background

1.1.1 General introduction

Semiconducting and conducting materials form the bedrock of an astounding range of modern devices. These components underpin vast fields of technology upon which modern society is hugely reliant. They find uses in everything from microchips to enormous photovoltaic arrays to different sensors and integrated circuits. The first report of the semiconducting properties of a material came in 1874 from the research of Karl Ferdinand Braun,[1] who discovered that crystals of lead sulphide (PbS) could act as rectifiers, work which contributed to Braun being awarded the 1909 Nobel prize in physics. Around 30 years after this seminal discovery, such crystals were applied to radio receiver devices,[2] thereby opening up new possibilities in terms of wireless communication. Over the next century, research continued to uncover new and exciting fields related to semiconducting technologies, with the predominant focus being on inorganic materials. Inorganic semiconductors remain the leaders in terms of performance in many applications; however such materials are not without their drawbacks, namely, related processing and more recently uncertainty in materials availability.[3, 4] Inorganics typically require very stringent control of purity and doping levels to ensure devices perform as expected. Furthermore the processing of materials such as silicon, require energy intensive processing to create high purity crystals — the starting material for many conventional electronic items. Creating high purity feedstocks, device processing and uncertainty in supply can make many inorganic systems either costly to manufacture or with a significant price volatility incorporated into the cost.

Plastic electronics, which encompass a diverse range of organic small- and macro- molecules can be processed much more easily when compared to many of their inorganic counterparts, most notably by solution processing techniques (detail of various techniques are given in Section 1.4). This attribute promise such materials to be processed roll-to-roll and opens up the potential of high-throughput production. In addition, since the materials are predominantly based on carbon, there is

no intrinsic reliance of scarce materials. There is also the possibility to produce the material feedstocks in a continuous manner.[5] Some of the key markets that plastic electronics could provide step-changes in include: photovoltaics, lighting and flexible/lightweight electronics.

Photovoltaics (PVs): Currently there is huge global impetus to develop renewable energy technologies, for which PV holds significant promise. For example although PV technology only comprises 10% of UK renewable power generation capacity, global agreements and European legislation have put in place a framework to increase the amount of renewable energy generated both in the short term (2020) and mid-term (2050). One of the major barriers to wider exploitation of PV is the initial capital cost of such systems, where there is potential for reduction by utilising OPV.

Lighting: Lighting currently accounts for an estimated 20% of global electricity consumption, and is therefore huge market and one linked with improving energy consumption. Again, organic light emitting diodes (OLEDs) are a technology that offers the promise of lower future production costs in addition to more efficient power usage.

Displays: As we move into an increasingly technology orientated world, one of the key human-interfaces with electronics is via displays; OLEDs have been integrated into small area products for over a decade, however recent improvement in manufacturing have opened up the possibility for larger area products including televisions.

Flexible/lightweight electronics: As the boundaries for what is possible with technology continually evolve, there is increasing demand for devices and components to hold new attributes to fit certain applications. This can include lightweight and flexible devices, for vast ranges of emerging applications for example: for clothing integrated electronics and foldable/roll-able items for portable devices.

As a consequence of these opportunities, the global market for plastic electronics has received over US$10 billion in investments over the last twenty years, and that this market is set to grow to US$25 billion by 2020.[6]

1.1.2 History of plastic electronics

Despite the widely held image of plastic electronics as a relatively new research field, some of the earliest reports of the organic materials exhibiting semiconducting behaviour date back as far as 1952,[7] where Eley *et al*. investigated the semiconducting properties of crystals of various organic compounds including: coronene, anthracene and phthalocyanine (structures shown in Figure 1.1 A-C respectively) — many of which are still investigated today. In this paper it was postulated that this behaviour originated from "*the excited orbitals of the π-electrons in the isolated molecule are combined to give non-localized orbitals stretching throughout the crystal*". In 1960, Kepler set out to measure the charge carriers of high purity anthracene crystals.[8] The results of this study highlighted many interesting findings, notably that holes appeared more mobile in such systems than electrons, and that in lower purity crystals the lifetime of charge carriers was significantly reduced. In 1963, Siemons *et al*. investigated the electronic properties of charge transfer salts formed from tetracyanoquinodimethane (TCNQ) with various cation-forming metals.[9] These measurements revealed the conductivity of organic charge transfer salts.

During the early 1970s, development of new materials for organic electronics[10] was undertaken alongside further investigation of the structures of such materials to try to better understand the origins of these phenomena.[11] The late '70s/early '80s saw a number of pivotal publications that helped to raise the profile of this emerging research field,[12, 13] with the first reports of OLEDs, organic field-effect transistors (OFETs) and OPVs.

To date the most widely commercialised technology is that of OLEDs, the original publication using polymeric emitters came from the Cavendish laboratory in Cambridge, where Burroughes *et al*. discovered the electroluminescence of p-phenylene vinylene (PPV) whilst attempting to drive the material to dielectric breakdown,[14] sparking huge interest in this field. Only a few years previously the first reports of an organic material acting analogously to a field effect transistor were reported for a molecular devices incorporating polypyrrole[15] and polythiophene.[16]

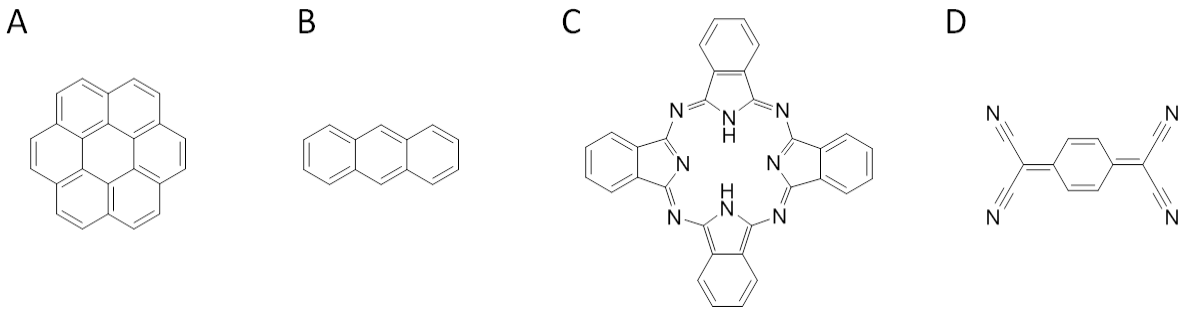


Figure 1.1: Molecular structures of a range of organic electronic materials investigated during the 1950s and 1960s: **A:** coronene, **B:** anthracene, **C:** phthalocyanine and **D:** tetracyanoquinodimethane.

The first organic photovoltaic device (OPV)[17] was reported in 1986 by Tang, this device comprised of an evaporated bilayer of a perylene derivative and copper phthalocyanine. The cell had a power conversion efficiency of around 1%, but most strikingly showed charge extraction that was relatively independent of bias resulting in a fill factor of 0.65. After these seminal reports, the fields of OLED, OFET and OPV continued to grow and diversify, giving rise to a wealth of new research areas and discoveries. From here on in this thesis will focus primarily on OPVs.

The fabrication of OPV devices continued in the bilayer format reported by Tang, however such devices have an inherent limitation in that, unlike a classic inorganic *p-n* junction, the excited states have a short diffusion length, typically reported on the order of 3-10 nm.[18-20] This effectively limits the number of excited states that can diffuse to the interface and dissociate, thereby limiting

the photocurrent achievable in such devices. To circumvent the problem of interface *vs.* volume trade-off, Sariciftci *et al.* investigated a fullerene:MEH-PPV composite in which the two components were blended in a common solvent and then co-deposited into a thin film.[21] Upon photo-excitation of the polymer they observed a reversible electron transfer from the polymer to the fullerene. In 1995, this idea lead to the first report of a bulk heterojunction (BHJ) OPV,[22] comprised of a poly[2-methoxy-5-(2-ethylhexyloxy)-1,4-phenylenevinylene] (MEH-PPV):[6,6]-phenyl-C61-butyric acid methyl ester (PCBM; from here on, "PCBM" refers to the C60 derivative unless otherwise specifically stated) blend between electrodes of indium tin oxide (ITO) and calcium, although the full spectral power conversion efficiency (PCE) was not reported.

After the reports of the first BHJ there were gradual improvements, in some part due to materials —most notably through the poly(3-hexylthiophene-2,5-diyl) (P3HT):PCBM system— first reported in 2002 by Schilinsky *et al*.,[23] with a PCE of around 2 %. This system continued to be one of the most widely investigated blends in the OPV[24] area. In 2003, improved PCE was reported, by thermal annealing whilst applying an external bias to the devices, leading to a PCE of around 3.5%.[25] This highlighted the significant changes that could occur within the microstructure of such blends in the solid state and the effects this could have on the device performance. By 2005 the P3HT:PCBM blend had shown cells approaching 5%.[23] These improvements had been correlated to structural characteristics of the system as deduced from transmission electron microscope (TEM) and X-ray diffraction (XRD). These techniques gave information on the phase contrast and crystallinity[26] in such blends, highlighting the complex phase behaviour of such blends. In 2008, Muller *et al.* explained the binary phase behaviour of a blend of a crystallisable polymer with a crystallisable fullerene as a eutectic system, and were thereby able to correlate changes in the optoelectronic properties to the binary phase diagram.[27] Visualising this system in terms of miscibility of the two components and competing crystallisation behaviour was an important step in better understanding the structure/property/processing relationships that govern the operation of such systems. Further reinforcement of the idea that ordering of materials was important (and controllable) was presented

in the same year by Kim *et al.*, who studied the regioregularity (RR) effect on efficiency of OPVs.[28] In addition Campoy-Quiles *et al*. observed vertical and lateral phase segregation in blends and how this related to thermal treatments, highlighting the processes of polymer crystallisation,[29] fullerene diffusion and aggregation. These works and others,[30, 31] helped to improve the understanding of some of the key attributes of the microstructure (in terms of phases present and ordering), however the microstructure was still typically depicted as a two-phase system of relatively pure domains of each material. However, in the case of P3HT, the relatively wide band-gap material meant that only a certain fraction of the solar spectrum could be harvested, thereby limiting the short-circuit current (and terminally PCE) attainable in such devices.[32] As a route to improving the PCE of OPV devices, the following years lead to the synthesis of a range of novel low-bandgap materials,[32, 33] capable of harvesting a greater portion of the solar spectrum, a selction of these materials are shown in Figure 1.2. The bandgap of typical OPV absorbers is generally larger than that of established PV technologies such as poly-crystalline silicon, which is one factor that can contribute to the generally lower efficiency of this technology to date.

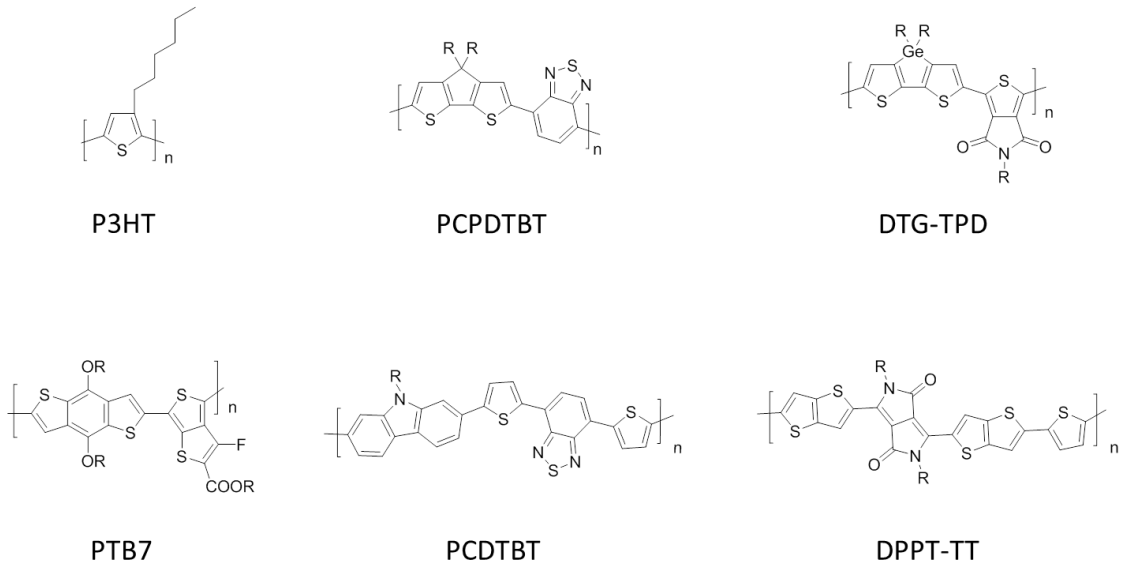


Figure 1.2: : Molecular structures of P3HT and five low bandgap donor polymers reported for OPV applications., poly[2,6-(4,4-bis-(2-ethylhexyl)-4H-cyclopenta[2,1-b;3,4-b']dithiophene)-alt-4,7(2,1,3-benzothiadiazole)] (PCPDTBT), dithienogermole derivative (DTG-TPD), poly({4,8-bis[(2-ethylhexyl)oxy]benzo[1,2-b:4,5-bdithiophene-2,6-diyl]-(3-fluoro-2-[(2-ethylhexyl) carbonyl]thieno[3,4-b]thiophenediyl)) (PTB7), poly[N-9'-heptadecanyl-2,7-carbazole-alt-5,5-(4',7'-di-2-thienyl-2',1',3'-benzothia-diazole)] (PCDTBT) and thieno[3,2-b]thiophene-diketopyrrolopyrrole based polymer (DPPT-TT). All polymers shown comprise different sub-monomer units.

Recently many new techniques have been employed that have given valuable insight into the microstructures of such systems. These have included *in situ* measurements during film formation and thermal annealing processes,[34-37] novel electron microscopy mapping,[38] scanning transmission X-ray microscopy (STXM),[39, 40] resonant soft X-ray scattering (R-SOXS),[41] small angle neutron scattering (SANS)[42] and grazing-angle incidence wide-angle X-ray scattering (GIWAXS).[43-45] Despite this impressive and diverse advancement in microstructural visualisation there is still no consensus on the exact nature and key attributes of the microstructure required for manipulation of key OPV device parameters.

Accompanying the range of analytical techniques employed, there has been a dramatic increase in the numbers of new materials[32, 46-48] reported (the structures of a selection of these are shown in Figure 1.2). These polymers can have a diverse range of attributes, including variable: crystallinity, persistence length, interaction parameters, solubilities, polydispersity *etc*. These chemical modifications can also have significant effect on the photo-physical properties, such as: energy levels, band-gap, absorption coefficient, charge mobilities *etc*. In 2009 Liang et al. reported devices based on a benzodithiophene donor polymer with an a PCE of 6.4%.[32] The following year the same group further refined this class of polymer to yield an efficiency of 7.4%. In 2013 Cabanetos et al. reported a PCE of 8.5%.[48]

Perhaps it is not surprising that such a diverse range of materials require a multitude of different processing protocols in order to access a microstructure that is most efficient in terms of OPV performance. This can include selection of: solvents,[49] additives,[46, 50] composition,[27, 51] annealing procedures[36] *etc*. As a consequence, laborious trial and error procedures are generally required in order to optimise OPV performance.

1.1.3 Current challenges: understanding structure/property/processing inter-relationships

Clearly there are still significant challenges related to the improvement of our fundamental understanding of donor:acceptor blends and their corresponding OPV performance. Many of the current challenges can be addressed by understanding the interplay between three different factors:

- Effects of processing
- Exact microstructure
- Photo-physical properties and OPV performance

Recent reports have indicated the presence and importance of intermixed phases within the active layer of a number of polymer:fullerene systems,[38, 52-55] rendering such an understanding complex. The result of this causes us to firstly re-appraise the view of the microstructure and as a result of this, to consider how this affects our model of the photo-physical processes that are ascribed to this structure.

The following three sections review these points from a *top-down* approach, in terms of current literature and areas of debate within the field. In Section 1.2 the photo-physical processes and various models are reviewed. Section 1.3 deals with the current understanding of the microstructure as probed by different techniques. Section 1.4 compares different techniques used to form thin films and highlights a range of the processes involved in the microstructural formation of these systems.

1.2 OPV operating principle

1.2.1 General processes

Although there is still vivid debate within the field about the exact nature of the processes leading to charge generation and current extraction within BHJ devices, the processes outlined in Figure 1.3 are widely accepted to constitute the general steps. Firstly a photon is absorbed. This usually occurs due to a π-π* electronic transition within the polymeric component of the blend. This excited state is then capable of undergoing one or more steps that result in dissociated charge carriers. For a polymer:fullerene system, it is typically the positive polaron that resides on the polymer and the negative species on the fullerene. Here, it is worthwhile to note another difference between conventional inorganic PV and OPV, which is the difference in dielectric constants of these two classes of materials. Inorganic materials generally have high dielectric constants, which allows for good charge screening upon separation of charges. Whereas organic materials typically have much lower dielectric constants, meaning that a higher binding energy of the two charges is typically experienced.

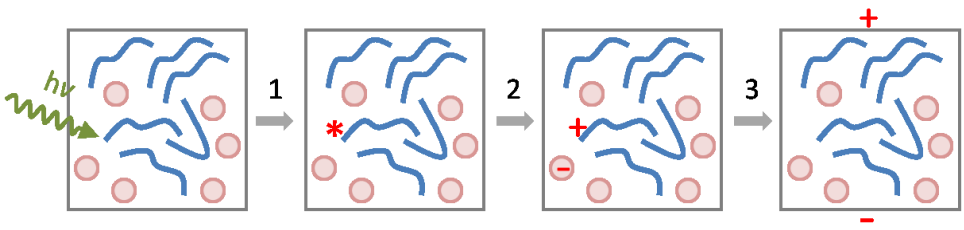


Figure 1.3: Schematic overview of the processes leading to photo-generated charge extraction in a BHJ solar cell. **1:** Photon absorption, typically from the polymer, resulting in an electronically excited state (*). **2:** Excited state (*) dissociates leading to the formation of unbound positive and negative charge carriers. **3:** The charge carriers travel to their respective electrodes, where they are collected.

1.2.2 The conventional model for charge generation

Conventionally OPV blends were thought to consist of two relatively pure phases of donor and acceptor[56] (as depicted in Figure 1.4), and as a result the explanation of the photo-physical processes occurring

within the microstructure were correlated to this picture. The series of processes used to describe charge generation and extraction are shown in Figure 1.4. It is worth highlighting here that each step of these processes is a competition between different pathways; for example, after exciton generation if the exciton does not migrate to an interface, it can decay to its ground-state (via a radiative or non-radiative pathway). Similarly, after a charge transfer state is created at an interface, it can either dissociate into free charges or recombine (via geminate recombination).

The five processes that are thought to occur in this model are outlined below:

1) Photon absorption leading to excitation of the molecule into an excitonic state
2) Exciton migration to the interface between the donor and acceptor materials
3) Electron transfer over the interface forming a charge transfer (CT) state
4) CT dissociation yielding free charges
5) Free charge migration to electrodes

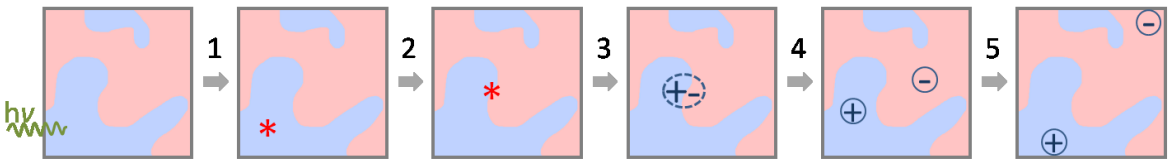


Figure 1.4: Schematics of the conventional two-phase microstructure of a donor (blue)/acceptor (red) blend and the corresponding photo-physical processes leading to charge generation and extraction. **1:** Photon absorption leading to exciton generation (*). **2:** Migration of exciton to a donor-acceptor interface. **3:** Electron transfer across the donor-acceptor interface, resulting in a coulombically bound charge transfer state. **4:** Dissociation of interface state into free charge carriers. **5:** Migration of charge carriers to respective electrodes.

However, such a picture leaves questions regarding the binding of such CT states, which due to the generally low dielectric constants of organic materials (when compared to their inorganic counterparts) should be expected to result in a coulombically bound CT pair that requires would require substantial energy in order to fully dissociate.[57] The exact nature of this CT state, the opto-electronic processes relating to it and it's impacts on charge generation and recombination are

currently areas of vivid debate. Some different refinements of the theory of charge generation considering the CT state are discussed in the following section.

1.2.3 Different refinements of the theory of charge generation

Over the past few years experimental and theoretical results have presented different possible mechanisms for charge generation raising interesting questions relating to the role of hot excitons, long range dissociation and enthalpic and entropic contributions to such processes.

Recently a number of reports of ultra-fast generation of charge carriers in polymer:fullerene systems including P3HT:PCBM and PCBTBT:PCBM have been reported. In these systems it was proposed that the formation of CT states that had an excess of energy (*i.e*. hot CT excitons)[57] could provide an important pathway to charge generation on femtosecond timescales. For example, a report by Piris *et al*.[58] observed charge pair formation on timescales below 200 fs. The report postulated that a more direct route to charge generation was occurring than had previously been accounted for. Furthermore, Grancini *et al*.[59] observed exciton splitting and the generation of CT states and polaron species within 50 fs in PCPDTBT:PCBM blends (depicted in Figure 1.5). One of the main postulations of this work was that the hot CT states had had a higher degree of delocalisation, when compared to (vibrationally) cold ones, which gave them an increased probability of dissociating. It was additionally claimed that hot dissociation causes an increase in charge generation yield.

A conflicting report on the influence of hot excitons in OPVs was forwarded in 2010 by Lee *et al.* where blends of P3HT:PCBM and PPV:PCBM were investigated. Here excitation directly into different states in the CT band (*e.g*. a below gap excitation) were used to probe thermally relaxed CT states. This report concluded that hot dissociation has a negligible effect on *J-V* characteristics[60] of devices fabricated from such systems.

In addition, the Salleo group recently investigated a vast range of systems (encompassing polymer:fullerene, polymer:polymer, polymer:small molecule) and reported[61] that hot excitons did not comprise a significant generation pathway in OPV devices. This was based on evidence that the internal quantum efficiency (IQE) (a measure of the efficiency of converting absorbed photons into extracted charges) was essentially constant over the probed excitation energy range. This was highlighted by the observation that excitation of the vibrationally relaxed charge transfer state (denoted CT_1 in Figure 1.6), had an almost identical internal quantum yield compared to higher energy excitations. . It was proposed that dissociation via the CT_1 state would dominate provided that k_{relax} was significantly faster than k^*_{CS} (both depicted in Figure 1.6). It was therefore suggested that the dominant feature in the competition between k_{CS} and k_f (which would determine charge generation efficiency) would be the energetic landscape connecting the CT_1 and CS states.

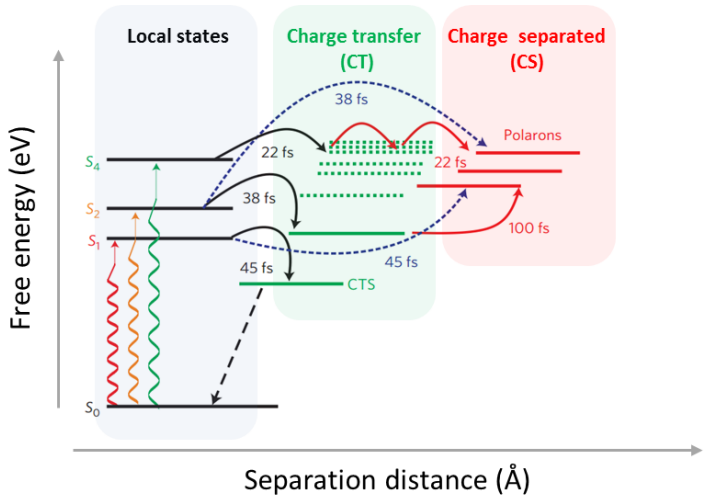


Figure 1.5: A schematic of the mechanism proposed by Grancini *et al*. for hot exciton dissociation. The ground state polymer is excited into different states (black), the higher energy states can more quickly dissociate into polarons. Here the lowest energy charge transfer state (CTS) is depicted as a loss pathway. The CT manifold is depicted green and the polaronic states red (adapted from Grancini *et al*., reference 59).

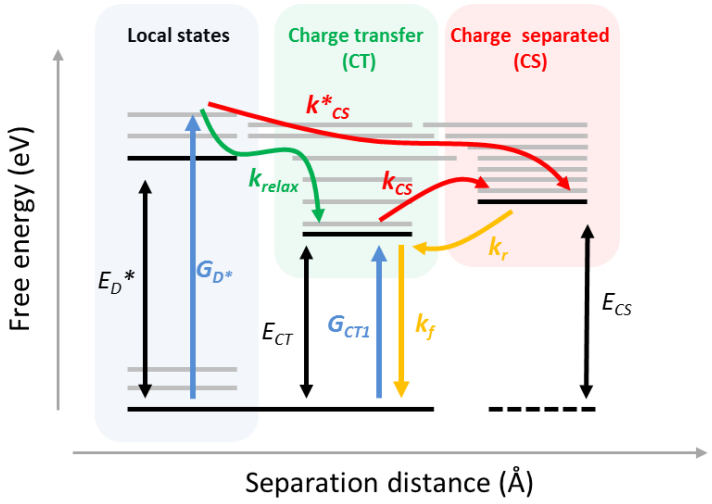


Figure 1.6: Schematic of the energetic states of the donor and acceptor systems. Displaying the ground electronic state (GS), excited donor (D*) levels, charge transfer (CT) manifold and charge separated (CS) states. Adapted from reference 61 (Vandewal *et al*.).

Another idea to address the question of coulombic binding of CT states at an interface has been postulated based on the modelling work of Troisi.[62] This work highlights that long range dissociation may actually be an energetically favourable process, *i.e*. charge transfer between non-adjacent molecules – depicted in Figure 1.7. The underlying argument here was that, in the case of P3HT, the surface of the crystallites (pure domains) have a larger deviation from the perfect crystal lattice (reported as conformational disorder). The result of this conformational disorder was an increase in the band gap via raising of the LUMO and lowering of the HOMO. It was argued that this interfacial disorder could act to effectively repel excitons (and also holes) from the surface of the crystallites. It was further postulated that exciton dissociation between non-adjacent molecules could occur, thereby leading to the formation of charge carriers with a greater separation distance and hence lower initial coulombic binding energy. In addition to the arguments for increasing charge generation, the same theory may be applied to the process of recombination, in that, if the positive polarons residing within the crystallites are repelled from the crystallite surfaces then their proximity to negative polarons (which would reside outside the crystallites) would be reduced, and hence

lower the probability of recombination occurring. Such an idea may also help to understand converse processes such as non-geminate recombination.

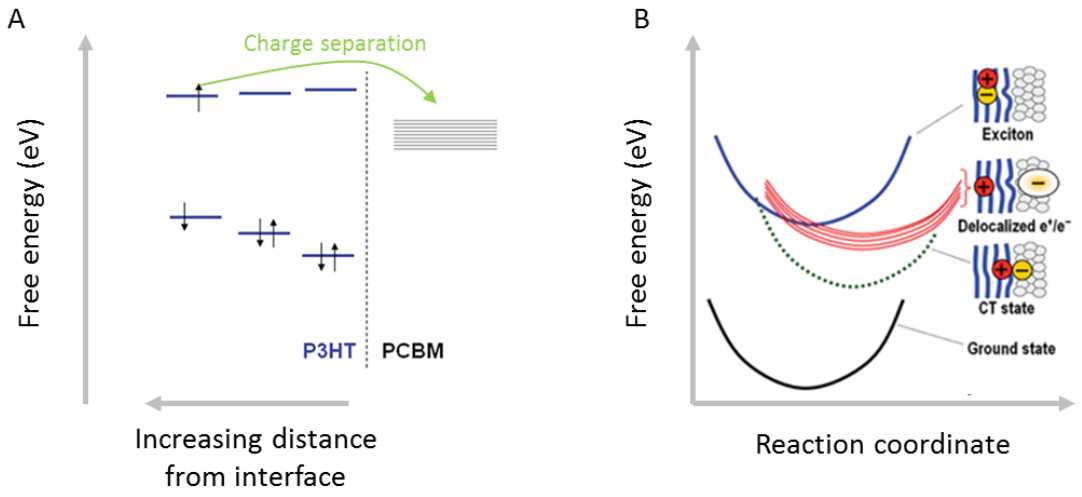


Figure 1.7: Depiction of the energetics of exciton dissociation in the long-range order theory proposed by McMahon *et al*. **A**: Schematic of a simulation of an exciton within P3HT. The exciton is repelled from the interface due to the increasing energy gap caused by structural disorder. **B:** Potential energy surfaces of the different energetic states. One of the key points here is that there is a smaller energetic barrier for an exciton (at or close to its energetic minima) to form a delocalised electron-hole pair rather than a CT state. Figure adapted from McMahon *et al.,* reference 62.

In addition to the theoretical ideas of long range dissociation proposed by the Troisi group, experimental work by Rumbles *et al.*,[63] highlighted that intermediate processes between photon absorption and charge generation can occur over a significantly long range. It was demonstrated that energy transfer in polymer/fullerene systems could occur through appreciably thick (*e.g.* 10 nm) blocking layers (BL). It was proposed that this energy transfer process occurred via Förster resonance energy transfer (FRET).

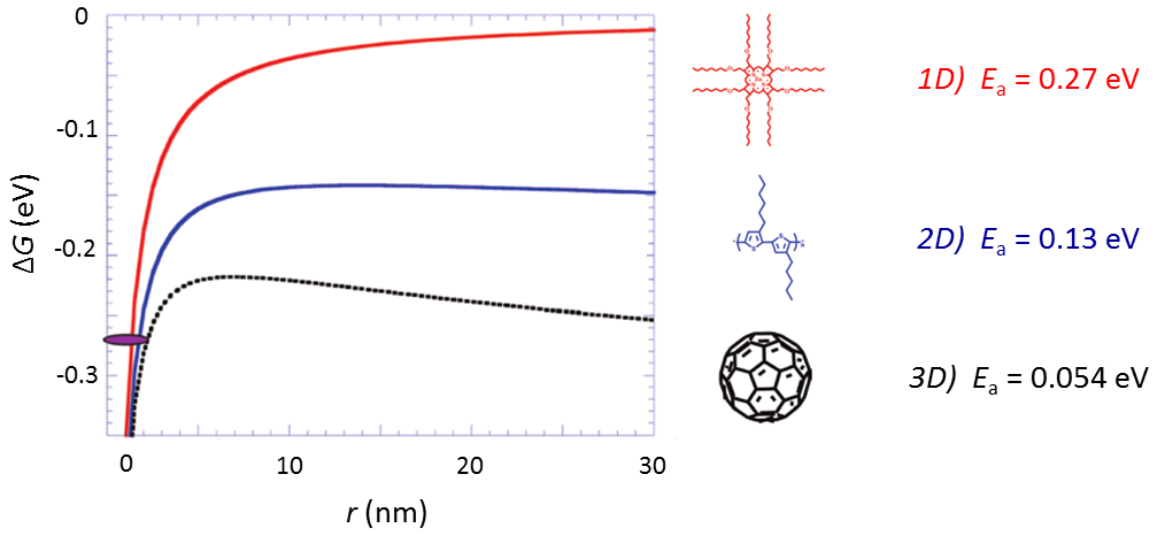


Figure 1.8: Molecular structures and calculated equilibrium free energy plots of electron acceptors of different dimensionality. **Left**: Equilibrium free energy of charge separation, Δ*G,* plotted against distance from interface, *r*. The purple ellipse represents the assumed ground state of -0.27 eV. **Centre**: Molecular structures of the exemplary 1D, 2D and 3D semiconductors. **Right**: The energy of the entropic contribution for the systems of differing dimensionality, where the highest dimension system would be expected to yield the largest entropic change (adapted from Gregg, reference 64), derived from equation 1.1 – 1.3.

Another interesting viewpoint relating to the question of the columbic binding of the CT state was proposed by Gregg,[64] whereby the dimensionality of the donor and acceptor were highlighted. In this context dimensionality refers to the potential for electronic delocalisation (and hence charge transport) within the solid-state structure. For example, a molecule capable of forming molecular wires with one-dimensional electronic delocalisation (in the π-stacking direction) was used as the single dimensionality example. The two dimensional case utilised P3HT, whereby electronic delocalisation was assumed to occur within both the direction of the polymer backbone and the inter-chain π-stacking. Finally the fullerene was employed as the three dimensional example as it was assumed that electronic delocalisation could occur in any direction between adjacent molecules. The main argument of this paper was that, the higher the dimensionality of the acceptor, the greater the entropic driving force for charge separation (as depicted in Figure 1.8). The relationships reported for the entropic energy of charge separation are shown for one, two and three dimensional systems, as Equation 1.1-1.3 respectively:

$$\Delta S = k\ln(1) = 0 \qquad \text{Equation 1.1}$$

$$\Delta S = k\ln(2\pi r/a) \qquad \text{Equation 1.2}$$

$$\Delta S = k\ln(4\pi (r/a)^2) \qquad \text{Equation 1.3}$$

where ΔS is the change in entropy, k is the Boltzmann constant, r is the distance and a is an assumed lattice constant. This concept relating to the importance of dimensionality of the electron acceptor may also provide an argument to help explain why certain planar non-fullerene acceptors do not efficiently generate polarons.

An additional report by Jamieson *et al*. detailed the use of PBTTT:PCBM(C60) (a material pair that forms a co-crystal) as a model system to investigate charge generation in differing microstructures.[51] Here, it was found that charges generated in the co-crystal experienced an energetic benefit by moving into the pure phase of either the donor or acceptor, in this specific system, the electrons into the pure fullerene domains, as depicted in Figure 1.9.[51] This report provides an interesting insight into the nature of finely intermixed phases in OPV blends as well as highlighting the fine interplay between energetic landscape and microstructure.

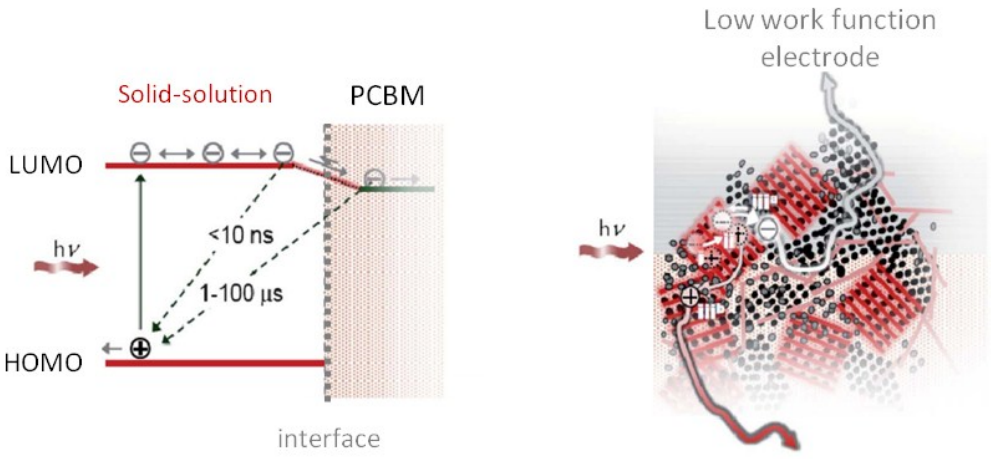


Figure 1.9: Representation of the energetic driving force reported by Jamieson *et al*. in a system of PBTTT:PCBM, whereby charges are generated in the co-crystal. The separation of the excited state is driven by the energetic benefit for charges (in this case electrons) to move into the phase pure/crystalline domains of the fullerene. Adapted from Jamieson *et al*. reference 51.

These differing reports highlight the current uncertainty of the processes of charge generation within the bulk heterojunction, especially when we consider that indeed many of these descriptions relate to an assumption that the relevant processes are occurring at well-defined interfaces between pure phases of materials. In order to address these challenges in the photo-physical processes, it is thus imperative to develop a more comprehensive understanding of the precise microstructure within the BHJ in order to provide a structural understanding into which the interpretation of photo-physical measurements can be interpreted. The following sections describe advances and understanding of the microstructure of polymer:fullerene OPV blends in terms of: phase morphology; composition; purity, perfection, size, shape *etc*.

1.2.4 OPV device operation: an electronic perspective

The previous sections outlined the processes resulting in charge collection on a molecular scale, in the below section the operation OPVs is discussed in the context of behaviour as part of an external circuit (as depicted in Figure 1.10). Considering the device from an electronic perspective can yield valuable information on the structure/property relationships of such a system.

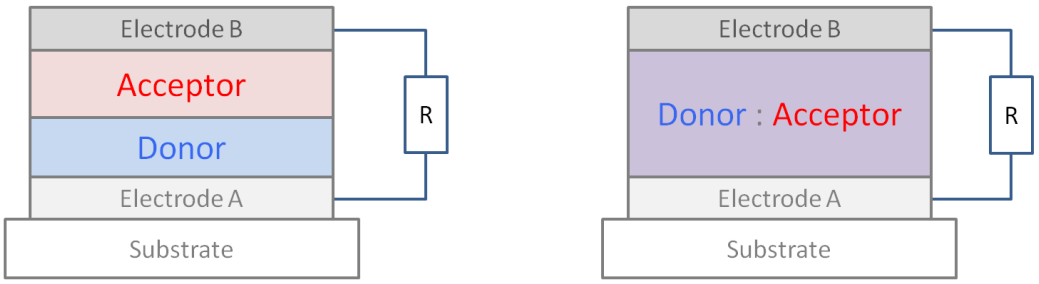


Figure 1.10: Cross-sectional schematic of two widely used device architectures for OPVs: Bilayer (left) and bulk heterojunction (right). The active materials are sandwiched between two electrodes, the bottom of which (*Electrode A*) is typically transparent, *e.g*. indium tin oxide (ITO) coated in PEDOT:PSS, while *Electrode B* would typically be a material with a different work function.

1.2.4.1 *Dark characteristics – $J_{dark}(V)$*

Before discussing the operation of the device under illumination it is valuable to consider the behaviour of a BHJ solar cell when no photo-generated charges are present, this is known as dark operation, $J_{dark}(V)$, and contributes to the observed behaviour under illumination $J_{light}(V)$. Assuming that the device can be modelled as a diode and current generator in parallel, then the device can be explained as in Equation 1.4 (for a given light intensity).[65]

$$\boldsymbol{J_{light}(V) = J_{dark}(V) + J_{photo}(V)} \qquad \textit{Equation 1.4}$$

An example of a P3HT:PCBM blend in dark operation is shown in Figure 1.11 (red) as $J_{dark}(V)$. Under reverse bias no current flows through the device, due to the rectifying behaviour of the diode. However in the forward bias regime, once the energetic barrier for charge injection is overcome, charges are injected into the device and current flows. As the forward bias is increased a greater amount of charge is injected into the device.

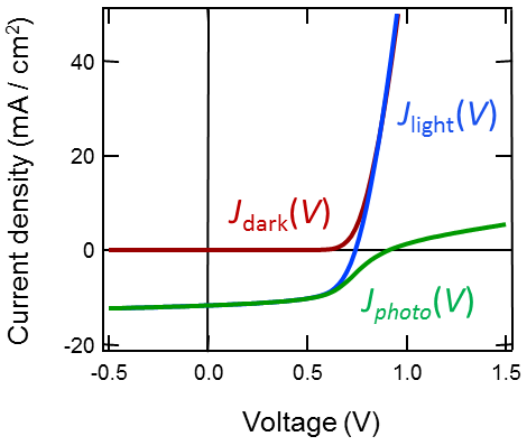


Figure 1.11: Current-voltage characteristics of an organic photovoltaic device (bulk heterojunction). Measurements of the device in the dark (red) and under illumination (blue) were used to calculate the photo-contribution (green).

1.2.4.2 Under illumination – J_{light} (V)

Under illumination (blue in Figure 1.11) the *J(V)* characteristics of the device are noticeably different from in the dark condition. The most striking difference between the dark and light conditions are the negative current that is created across a range of positive and negative bias (shown here as -0.5 to ~0.6 V). This implies that at negative bias $J_{light}(V)$ is dominated by $J_{photo}(V)$ (green in Figure 1.11), where there is a negative current density the photogenerated charge carriers. As increasing positive bias is applied $J_{light}(V)$ shows a reduction in negative current, which at a certain point becomes positive. It is convenient to consider the $J_{light}(V)$ to be comprised of three segments referred to from here as: photodiode; photovoltaic and forward bias regimes.

1.2.4.2.1 Photodiode regime

The photodiode regime is defined as the regime where the applied voltage is negative. In this regime the current flows in the negative direction. At increasing negative bias, the current extracted under illumination increases. This is related to the greater applied electric field being able to more efficiently extract charges from the device. It also means that differences in light intensity will typically result in the largest difference in the photocurrent, and hence improves the sensitivity to brightness.

1.2.4.2.2 Photovoltaic regime

The operation most relevant for this thesis is within the photovoltaic regime. This comprises all activity with the fourth quadrant of the *JV* output (*i.e.* when a positive voltage is applied and the current is negative). The key parameters used to characterise this regime are explained below. Firstly the power conversion efficiency (PCE) of a solar cell can be explained using Equation 1.5, which is

the ratio of denotes incident light power (P_{in}) and output electrical power (P_{out}). The power output of the device for a given spectral profile is determined by the sum of the short circuit current (J_{sc}); open circuit voltage (V_{oc}) and fill factor (FF), as depicted in Equation 1.6.

$$\boldsymbol{PCE = {P_{out}}/{P_{in}}} \qquad \textit{Equation 1.5}$$

$$\boldsymbol{P_{out} = V_{oc} J_{sc} FF} \qquad \textit{Equation 1.6}$$

The **fill factor** is a measure of the ideality of the device and it is a representation of how closely the maximum power point (J_mV_m) relates to the theoretical maximum power ($J_{sc}V_{oc}$), as shown in Equation 1.7. Visually it is observed as the "squareness" of the $J_{light}(V)$. Examples of varying fill factors are shown in Figure 1.12. It can also be useful to consider the FF a measure of the charge extraction efficiency as a function of applied voltage. For example, if the charge extraction is relatively independent of bias, then the curve will be relatively square, meaning a higher FF.

$$\boldsymbol{FF = {J_m V_m}/{J_{sc} V_{oc}}} \qquad \textit{Equation 1.7}$$

The **short circuit current**, is a measure of the extracted photocurrent at zero bias. It is one of the two boundaries of the photovoltaic regime. The J_{sc} can be considered as the summation photo-extracted charges across the wavelength range of interest ($\lambda_{min} \rightarrow \lambda_{max}$). It is derived from integration of the external quantum efficiency (EQE) as in Equation 1.8, where $S(\lambda)$ is a reference for a given power intensity (*e.g*. Air Mass 1.5G), q is the electron charge, c is the speed of light and h is Planck's

constant. The EQE is the summation of the efficiency of absorbing photons (η_A) multiplied by the efficiency of converting absorbed photons into extracted charges (η_{IQE}).

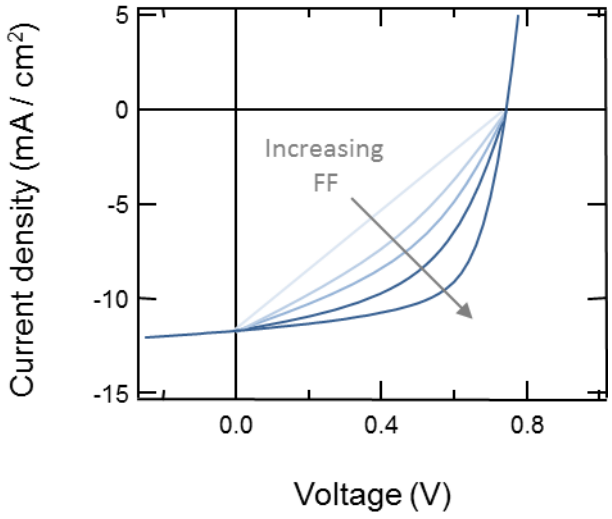


Figure 1.12: *J-V* characteristic of an OPV device exhibiting increasing fill factor from 0.25 to 0.7, shown by progressively darker lines and the output character becoming "squarer".

Open circuit voltage, is the other boundary condition of the photovoltaic regime. This is a representation of the flat band condition (*e.g*. when the applied bias balances the internal field), this can be thought of the maximum possible voltage that can be attained from the cell. Typically the theoretical upper bound for this value is $HOMO_{donor}$ - $LUMO_{acceptor}$.

$$\boldsymbol{J_{sc} = \int_{\lambda min}^{\lambda max} \frac{q\lambda}{hc} EQE(\lambda) S(\lambda) d\lambda} \qquad \textit{Equation 1.8}$$

1.2.4.2.3 Forward bias regime

In this regime the applied voltage is greater than the internal field of the device, causing charge to flow in the "forward" direction. We can see by comparing the magnitude of $J_{photo}(V)$ and $J_{dark}(V)$ in Figure 1.11, that as the applied voltage becomes more positive $J_{light}(V)$ becomes increasingly dominated by the dark contribution. In this regime increasing the applied voltage leads to a dramatic increase in the current passing through the device.

1.3 The influence of microstructure

1.3.1 Number of phases

The exact nature of the microstructure within BHJs has been an area of intrigue since initial reports. In the original paper detailing OPV devices created from blend of polymer and fullerene, the microstructure was described as a "*phase separated, bicontinuous network of donor and acceptor species*",[22] which made up the picture that was generally adopted within the field.[66] The idea of a bicontinuous and (relatively pure) three-dimensional microstructure was commonly accepted throughout the field and comprises the classic two-phase model of a BHJ (as depicted in Figure 1.10 left). As mentioned in the previous section this "picture" is the one onto which much of our understanding of the photo-physical processes has been laid.

More recent work has indicated that many systems may in fact comprise of a more complex microstructure including a finely intermixed phase,[38, 52, 67, 68] as depicted in Figure 1.10 (centre panel). For example Pfanmöller *et al*., used analytical electron microscopy to observe the presence of an intermixed phase in conjunction with two relatively pure phases of P3HT and PCBM. Furthermore, work by Treat *et al*. assessed the temperature dependence of mixing of different fullerenes into the amorphous fraction of different semicrystalline semiconducting polymers, revealing the partial miscibility of these systems. Collins *et al.* and Watts *et al.* convincingly showed that at quasi-

thermodynamic equilibrium, there is still a significant amount of fullerene intermixed within the polymer, implying the persistent presence of this amorphous solid solution, due to a certain degree of miscibility between the two components.[12,13] Other work utilising a broad range of techniques[14-19] further confirms the presence of such an intermixed phase in a range of polymer:fullerene systems.

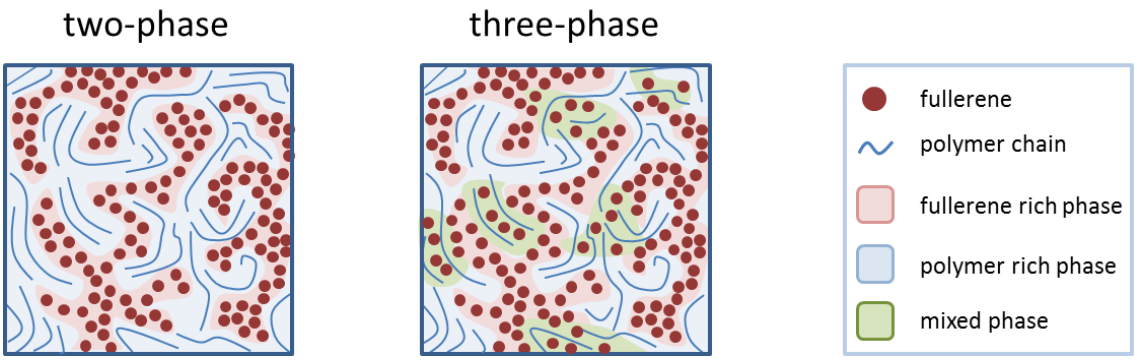


Figure 1.10: Schematics showing representations of the different possible microstructures. **Left**: Two-phase structure comprised of relatively pure phases. **Right**: Three-phase system which also contains an intermixed phase of the two components.

The identification of this intermixed phase raises significant questions as to its role within the BHJ. Current literature indicates that it can be expected in a range of systems, where there is partial miscibility or strong kinetic trapping. However it is also reported that the formation of a microstructure comprised entirely of this intermixed phase would likely be detrimental to device performance.[41, 54, 69] In cases of a single phase system, it has been observed that geminate recombination limits charge generation[70] and possibly the ability to extract carriers from the active layer. These findings highlight the sensitive interplay of different phases within the microstructure of OPV blends.

1.3.2 Nature of phases

1.3.2.1 Pure phases

In addition to the ongoing debate related to the number of phases present, there is still a significant discussion relating to the precise nature of the individual phases which constitute the microstructure. In general, phases comprised of a large majority of a single component are believed to be important for charge transport. Such phases are discussed in the following three subsections relating to varying degrees of ordering, based on: the more typical, classical polymer descriptions of semicrystalline and amorphous as extremes, but also highlighting an intermediate state which is described as locally ordered or aggregated.

1.3.2.1.1 Classic semicrystalline domains

Many classic polymers, such as polyethylene and isotactic polystyrene are capable of crystallising. In general crystallisation is driven by an energetic benefit that can be achieved by the polymer chains packing closely together. While one would expect the most energetically favourable state for a crystallisable polymer below the melting temperature to be a single chain-extended crystal, this rarely occurs, in large part due to chain entanglements.[71] For high molecular-weight polymers, crystallisation typically occurs through a chain folding process. In the simplest instance this requires the polymer backbone to bend through 180^{o} and fold-up next to itself, known as a tight fold (shown in red in Figure 1.11). Once a sufficient number of chains have arranged as to form a crystal nucleus, frontier growth can occur. As more sections of polymer chains align a structure known as a lamellar is formed (Figure 1.11, shown in grey). As the polymer chains have a specific orientation within the lamellar it may result in favoured growth in one or more dimension. The length of the extended backbone within the polymer crystallite is the lamellar thickness, *l*, and is generally much smaller than the other two dimensions of the lamellar, *x* and *y*. The nature and

quality of these crystalline regions can have a drastic impact on the properties of the material. The attributes of the crystallite populations can determine the macroscopic properties of these systems, such as: toughness, thermal stability, opacity, *etc*.

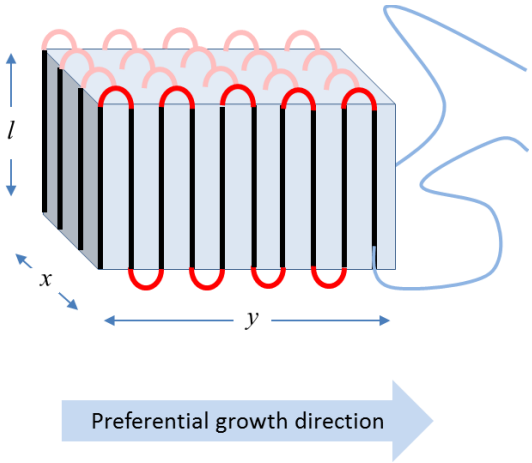


Figure 1.11: Schematic of polymer crystallisation forming a lamellar of thickness, *l*. The extended sections of the polymer chains are shown in black, tight folds in red and un crystallised material in blue.



Figure 1.12: Molecular structures of two semicrystalline organic electronic polymers based around thiophene moieties: **Left**: Poly[2,5-bis(3-tetradecylthiophen-2-yl)thieno[3,2-b]thiophene] (PBTTT). **Right**: Poly[5,5-bis(3-alkyl-2-thienyl-2,2)-bithiophene (PQT).

Similarly, semiconducting polymers can exhibit semicrystalline behaviour such as regio-regular (RR)-P3HT,[72] poly[5,5-bis(3-alkyl-2-thienyl-2,2)-bithiophene PQT[73] and PBTTT[74] (depicted in Figure 1.12). The nature and quality of the crystallites can be affected by: the primary structure of the polymer, processing history and molecular weight, amongst others.[75] Changes to the nature of the crystallite population can have a dramatic effect on the optoelectronic properties of such

systems. For example, the size of crystallites of a semiconducting polymer will be one factor determining how intimately another species (*e.g.* an electron acceptor) can intermix. When considering that the diffusion length of an exciton is estimated to be on the order of 10 nm,[19, 20] if the crystallites are significantly larger than this distance along a minimum of one-dimension, it is likely that a large proportion of excitons formed in these crystals would not be able to diffuse sufficiently close to an interface to enable dissociation. Furthermore, the quality of such crystals, *i.e.* how well the crystallites adhere to the theoretical crystal lattice, can have notable effects on the resultant strength of the π-π interactions within the crystal, and, hence, the molecular coupling between adjacent chains.[76, 77] This disorder can be conceptualised as the paracrystallinity parameter, *g*, where a greater *g* refers to a larger deviation from the perfect lattice (examples depicted in Figure 1.13). Additionally if we consider that charge transport is preferential in one direction (*e.g.* along the polymer backbone) it is likely that the macroscopic orientation (related to crystalline texture) of the overall crystallite population will affect the charge transport properties.[72, 78, 79]

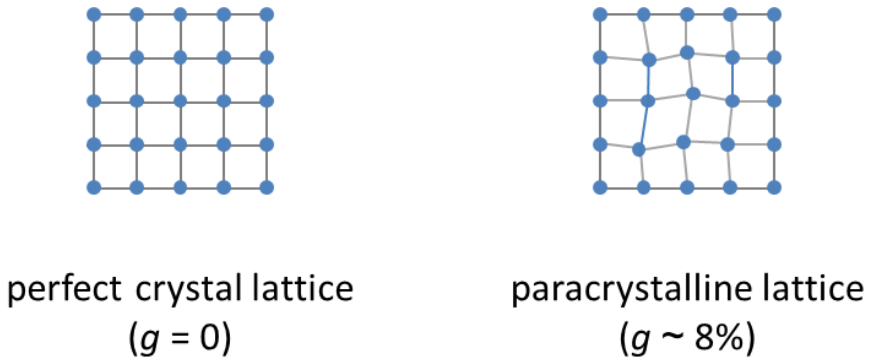


Figure 1.13: Schematic representations of crystal lattices with differing degrees of paracrystallinity. **Left**: Perfect 2D lattice (where *g* = 0). **Right**: Lattice with significant paracrystallinity (*g* ~ 8%).

The long-range coherence observed in some polymers allows them to be probed with techniques such as X-ray diffraction and differential scanning calorimetry (detailed in chapter 2) which can be used to gain important detail about coherence lengths within crystals, crystalline quality, relative degree of crystallinity and textural information *etc*.

1.3.2.1.2 Local ordering /aggregation

In addition to crystalline (long-range order) and amorphous (absence of long-range order), work over the past few years has highlighted the presence and importance of regions of shorter-range order than that of a crystalline material,[80, 81] which and in some cases share attributes more commonly associated with liquid-crystalline polymers.[82, 83] For example, Watts *et al*. studied the polymer poly[(9,9-di-*n*-octylfluorenyl-2,7-diyl)-*alt*-(benzo[2,1,3]thiadiazol-4,8-diyl)] (F8BT), using polarised resonant soft X-ray scattering (P-SoXS) to probe the molecular orientation. This work was able to discern the highly ordered fractions that would conventionally be thought of as crystalline coexisting with more locally ordered regions outside of the "crystalline" domains, revealing a strong retention of (short-range) order within these non-crystalline regions.

Building further on the use of P-SoXS to investigate ordering in non-crystalline systems, Collins *et al*. probed the molecular orientation on length scales of around 10 nm and above in blends of two semiconducting polymers: P3HT and the naphthalene-diimide derivative, N2200.[83] This work highlighted that even in complex multi-component, multi-phase systems it was possible to discern the different materials and, additionally, orientation of regions that were non-crystalline.

Beside the development of soft X-ray methods, recent work has used similar approaches to interpret high resolution transmission electron microscopy (HRTEM)[84]. Thereby N2200 was observed to have a striking degree of ordering.[85] Using the well-defined lattice planes (~2.4 nm) visible in Figure 1.15, it was possible to determine the backbone orientation thus revealing the meandering-type orientation. This structure again highlighted clearly that between long-range and completely disordered domains, short-range ordering could persist.

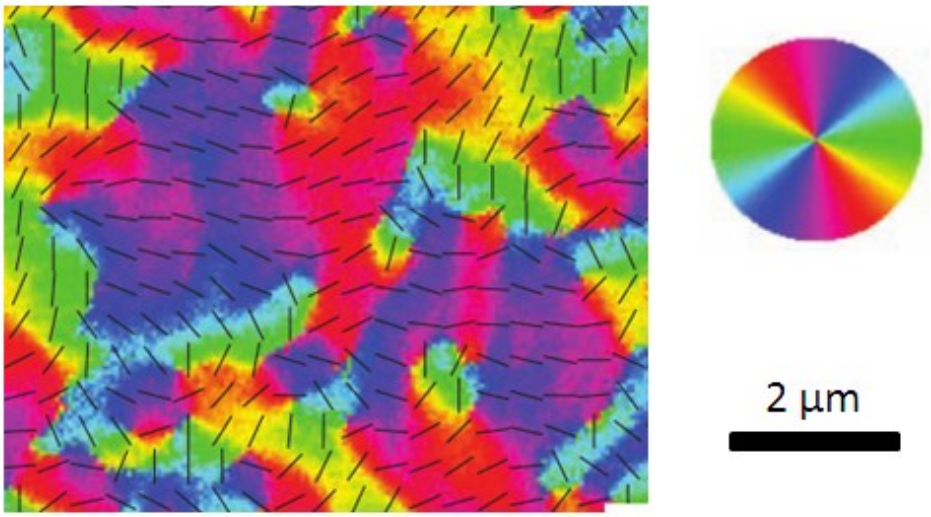


Figure 1.14: Transmission X-ray microscopy images of the preferred orientation of the polymer backbones (deduced from the in-plane resonance). The overlaid black lines indicate the direction of the fully extended polymer backbones**.** Circular colour scale shows the orientation perpendicular to the polymer backbone. Adapted from Watts *et al*., reference 82.

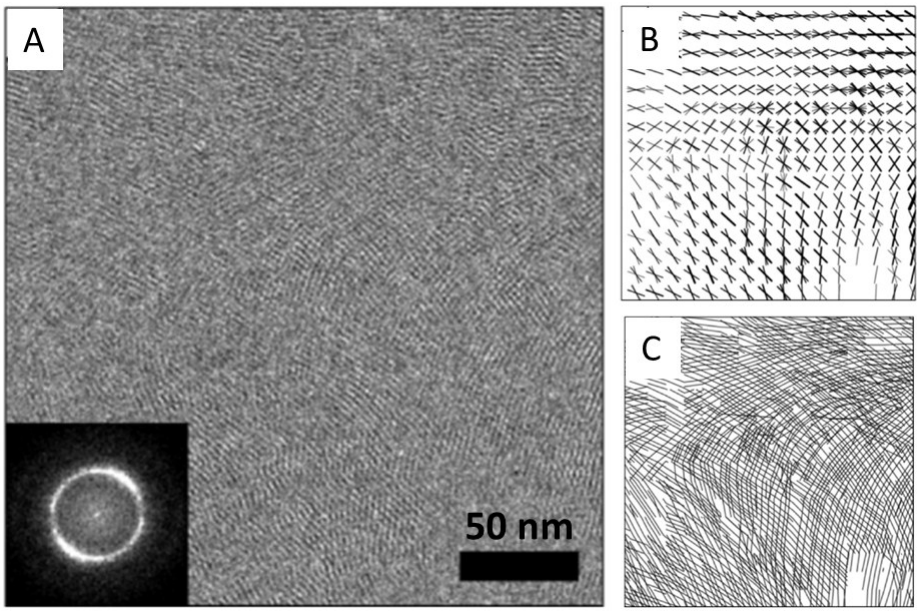


Figure 1.15: HRTEM and corresponding analysis of polymer backbone orientation of a thin film of N2200. **A:** HRTEM showing noticeable texture and a lattice plane of ~2.4 nm which appears to curve through different orientations. **B:** Computed directors drawn parallel to the lattices observed in the HRTEM. **C:** Addition of the local field lines representing the average direction of the polymer chains allow easier visualisation. Scale bar represents 50 nm. Adapted from Takacs *et al.,* reference 85.

While such aggregated domains have been observed via a number of computational imaging techniques, work from Noriego *et al.*[80] investigated the effect of localised aggregates on the charge transport properties of such systems, placing them in the context of a spectrum between classical semicrystalline and amorphous materials. One of the key findings of this work is that the presence of interconnected, localised aggregates is one of the underlying factors capable of giving rise to high charge mobility within materials. These aggregates can act as efficient interchain hopping sites to promote charge transport in the second most preferential direction (after backbone transport).

1.3.2.1.3 Disorder

In addition to the two cases outlined above which focus on long-range and locally ordered phases, it is worthwhile to highlight that certain materials can adopt significantly more disordered conformations. Such materials include: polytriarylamine (PTAA), regiorandom (RRa)-P3HT and various PPV derivatives, such as MEH-PPV and poly[2-methoxy-5-(3',7'-dimethyloctyloxy)-1,4-phenylenevinylene] (MDMO-PVV).

Disorder also seems to be important for optoelectronic processes, including exciton dissociation and charge generation. For instance, when comparing the disordered and ordered regions of organic semiconducting materials, the HOMO and LUMO levels of these dissimilar domains will differ. This can in many cases promote the exciton dissociation and charge carrier generation as well as limiting charge recombination, with the more ordered regions acting as energetic sinks for the charges created.[51, 62, 80, 86, 87]

1.3.2.2 Intermixed phases

1.3.2.2.1 Solid solutions

The presence of intermixed solid solutions have been reported for a number of polymer:fullerene systems.[38, 52, 67] A solid solution can be defined as a two- or multi-component system that forms a one-phase microstructure (*i.e.* a microstructure characterised by the absence of phase separation). This can occur when the components are fully miscible or through kinetic trapping of the microstructure *e.g.* during rapid solvent evaporation or cooling that prevents such phase separation. While the role of such intermixed phases is still under debate, the fact that they can make up significant fractions of the microstructure raise the question whether they significantly influence the photo-physical processes within the active layer. The intimacy of mixing of the two components can be expected to allow for efficient quenching of excitons within such a layer and, hence, may have significant effects on the processes relating to charge generation. However such intimate mixing may also contribute strongly to adverse effects such as geminate recombination.

1.3.2.2.2 Co-crystal formation

Organic co-crystals were first reported over 150 years ago[88] and present an interesting class of architectures. In these systems a crystal comprised of a well-defined stoichiometry of two (or more) molecular species is created.[89] The intimacy of mixing and well defined molecular ordering of these components lead to systems with properties different to either of the individual species. Within the field of plastic electronics, a co-crystalline phase within PBTTT:PCBM(C60) was observed.[90] This phase consists of PCBM(C60) intercalated between the side chains of the polymer. Further work has demonstrated that the most efficient OPVs are created for PBTTT:PCBM(C60) at around a 1:4 ratio, where the co-crystal phase co-exists with a relatively phase pure fullerene domains.[51]

1.3.2.3 Microstructural conclusions

The role and interplay between the different phases that can be present in OPV active layers is believed to be critical for determining device performance. However the complexity of the phase morphology in conjunction with the challenges that are encountered with building up a comprehensive picture of the microstructure (domain size, degree of crystallinity, *etc*.) render linking microstructure to device performance difficult. For this reason there is still an ongoing debate within the field as to what attributes the optimal microstructure/phase morphology would contain. In order to gain a deeper insight of the microstructure/phase morphology and how these can be manipulated, the following section looks at a range of processing techniques and conditions that can contribute to microstructural formation during solution processing in addition to post-deposition treatment.

1.4 Thin film deposition/structure formation

1.4.1 Deposition processes

One of the key attributes of organic electronic materials is, as already alluded to above, the ability to process them from solutions. The next section will briefly discuss a number of processing techniques that can be used to deposit donor:acceptor blends from solution. On a laboratory scale, spin-coating is the most widely used technique for creating thin (~5-500 nm) films of a material. The technique works by covering a substrate in a solution and then rotating the substrate (typically between 800 - 4000 rpm). This causes the solution to be spread over substrate to form a continuous wet layer of generally equal thickness. As this layer has a very large surface-to-volume ratio the evaporation of the solvent is fast, meaning that with a typical donor:acceptor mixture dissolved in a common solvent) in under 10 seconds of spinning the blend will have solidified. The simplicity of equipment and quickness of processing have made this technique hugely popular. However it is not

without major constraints. Firstly, a large amount of the material (typically <90%) is wasted during the spinning process. Secondly, this process is essentially a batch production technique and is therefore not easily converted into a continuous production technique. Also, spin-coating is limited with respect to the areas that can be covered. A schematic of the spin-coating technique is displayed in Figure 1.16.

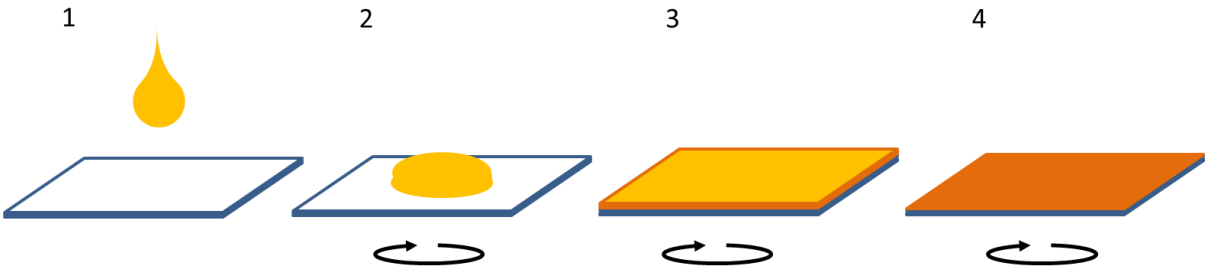


Figure 1.16: Schematic of the spin-coating process showing (from left to right): **1:** The solution is deposited onto the substrate. **2:** The substrate spinning is initiated forcing the solution to spread across the substrate. **3:** The wet film forms over the substrate. **4:** The film dries via solvent evaporation.

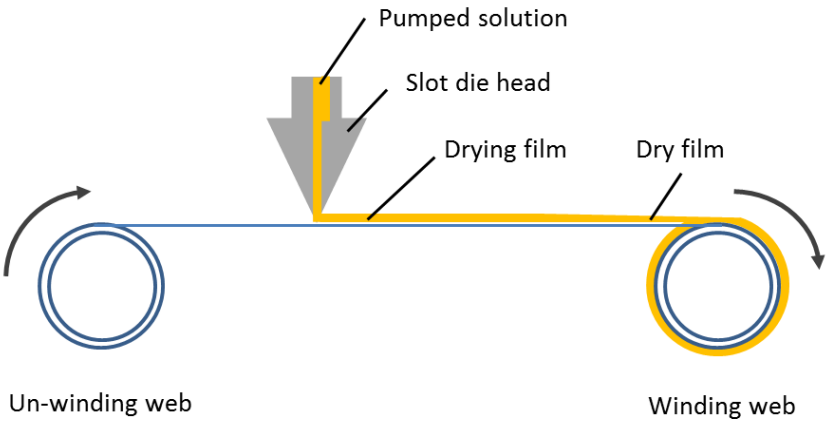


Figure 1.17: Schematic of the slot-die coating process of an active ink (*e.g.* donor:acceptor mixture) onto a roll-to-roll web, where the ink solution is deposited from the slot-die head, solvent evaporation leads to drying and is re-rolled onto the end web.

In order to truly realise the potential of solution processable material systems it will be necessary in many cases to utilise roll-to-roll manufacturing techniques rather than spin-coating. These encompass a range of processes such as gravure printing, offset lithography, doctor blading, slot-die coating and wire-bar coating. Unlike spin-coating they can be adapted to continuous production. The unifying feature of these techniques is that the coating is performed in a single direction, whereby the substrate moves relative to the coating head or vice versa. As an example, the slot-die coating process is schematically depicted in Figure 1.17.

Another technique that is widely used to create thicker films of material is drop casting, whereby the polymer solution is dropped onto a surface and left to dry. Typically this process results in longer drying times so can give the solute more time to move towards a state of thermodynamic equilibrium. An extension of this simple drop-casting technique is that of inkjet printing, whereby small volumes of material are deposited onto a substrate to form a pattern.

1.4.2 Microstructural formation

There are a number of phenomena that influence the microstructure of a system. In this section, these are broken down into two areas of practical interest: *i.e.* those occurring in solution during solvent evaporation and those occurring in the solid state (for example during thermal annealing).

1.4.2.1 Solution processes

1.4.2.1.1 Crystallisation

One of the key phenomena that can affect the microstructure of materials systems is their crystallisation behaviour upon solidification. For example, casting a solution comprised of a solvent

and a crystallisable organic solute, can be depicted in a simplified manner using a binary phase diagram (as shown in Figure 1.18). During casting from a dilute solution the solvent will evaporate. If the temperature is held constant, the drying process can occur as indicated by the red line in Figure 1.18. In this case, one starts with a homogeneous single-phase system and after a critical concentration is surpassed the organic solute may crystallise, resulting in two phases — crystalline organic solute and a mixed, liquid phase of the solvent and organic solute. It is worth noting that this critical concentration will depend on the temperature.

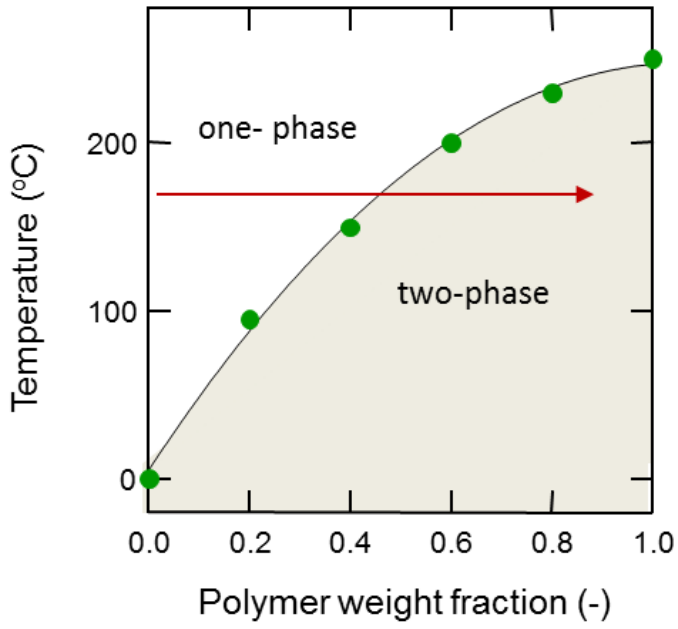


Figure 1.18: A binary phase diagram of a typical solvent:crystallisable solute mixture. Isothermal solidification is indicated with the red line.

1.4.2.1.2 Liquid-liquid phase separation

From a simple perspective if we firstly consider the binary phase diagram of a system of component A and B, which has an upper critical solution temperature (UCST) (as shown in the bottom panel of Figure 1.19), the region excluded by the outer (binodal) curve will form a single phase. However, if

we consider a blend of composition *C,* there will be a significant difference in the phase behaviour as a function of temperature. Essentially, above the UCST the binary will typically exhibit a single energetic minimum as a function of composition and temperature, meaning the formation of a single phase is favoured. However if the temperature is reduced to below the UCST, for example to T_x the free energy landscape may exhibit two local minima (as depicted in the top panel of Figure 1.19). The presence of two energetic minima can result in an energetic benefit for the system to undergo phase separation. The free energy curve plotted in Figure 1.19, has two notable regimes within it. Firstly is the region between S_A and S_B, known as the spinodal (shaded orange in the bottom panel of the figure). Within the spinodal region the curvature of the free energy as a function of composition is negative. As a result spontaneous phase separation into an *A*-rich and a *B*-rich phase will occur if the spinodal region is entered (for example by rapidly cooling a blend of composition *C* to temperature T_x). The points S_A and S_B denote the spinodal limits, as they represent the points of inflection (*i.e.* the curvature is 0) on the free energy curve. The region between the spinodal and the two energetic minima are known as the binodal region (here the curvature of the free energy surface is positive) and compositions within this region are metastable.

The example given above concerns a two component system that is partially miscible and phase separates during cooling. However in many cases we are interested in ternary mixtures, *e.g*. a polymer:fullerene:solvent blend. Figure 1.20 shows a typical isothermal ternary phase diagram of such a blend. Here we can see some similarities with the binary phase diagram, whereby there are spinodal and binodal regions in addition to a composition region where a single phase is favoured. It is clear that in the dilute regime (the top of the diagram) the mixture can exist as a single phase. In the homogenous mixture regime (*i)*, if we now consider the removal of this solvent (as depicted by the grey dashed line), at a certain point the binodal line will be intersected (*ii*). This can result in the decomposition of the homogenous mixture into two phases, which will each contain a certain fraction of each of the three components. The partitioning of the solvent into these phases can be determined through tie-lines and is not necessarily symmetric, meaning that one phase may become

more solvent-rich than the other. This may have important implications on subsequent processes such as molecular ordering because the presence of solvent within a certain domain type will, influence the mobility of the molecules.[91]

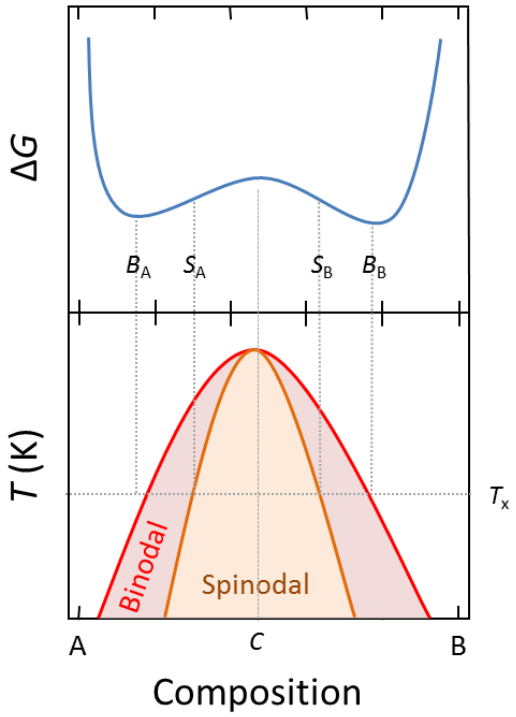


Figure 1.19: Representations of the phase separation behaviour of a partially miscible binary system. **Top**: The Gibbs free energy (ΔG) at a given temperature (T_x) plotted against composition. The binodal points are depicted as B_A and B_B. They depend on the majority component of the phase, as do the spinodal limits S_A and S_B. **Bottom**: Temperature plotted against composition. The phase boundaries are depicted as darker lines, including the binodal (red) and spinodal (orange).

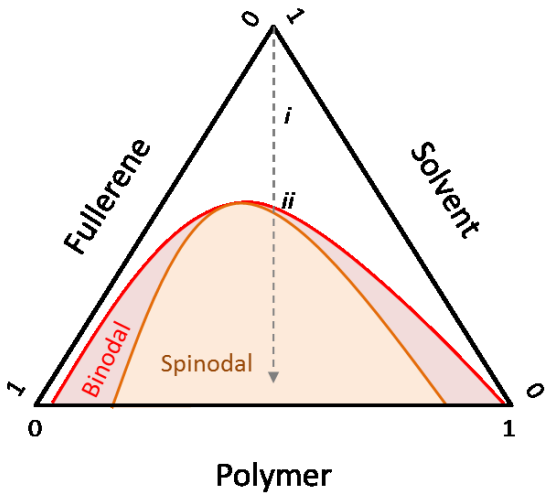


Figure 1.20: An example of an isothermal ternary phase diagram of a polymer:fullerene:solvent blend. Such diagrams can be constructed experimentally or modelled using Flory-Huggins theory. The orange line represents the spinodal and the red line, the binodal.

1.4.2.1.3 Nucleation

Another aspect that is important to consider during solidification of materials is their nucleation process. This applies as much to organic materials as it has been established for metals or ceramics; indeed, control of nucleation has been shown to be highly beneficial in controlling the mechanical[92] and optical properties[93, 94] of a range of organic materials, and, more recently, has been shown to have significant effects on the optoelectronic properties of organic semiconductors.[95] The reason for this is because the nature of the nucleation of an organic material can have significant effects on its final microstructure; for example, for semicrystalline matter, in the case only a few nucleation sites are present during solidification, then typically larger crystallites will be grown than if many nucleation sites are present. Another scenario where nucleation is relevant is where there is no means for a given material, and especially macromolecular systems, to nucleate during the solidification process (neither via heterogeneous nor homogenous nucleation); then a glassy state is induced that often can be rather stable hindering formation of crystalline or molecularly ordered regions even after post deposition treatments such as annealing. Use of additives, such as nucleation

agents, can assist in this scenario to prevent, or at least limit, this vitrification process (see also 1.4.2.1.4). Clearly, careful control of the temperature of deposition[96] as well as the drying rate[97] is, thus, essential during deposition of organic semiconducting system as small variations can have significant effects on their final properties.

1.4.2.1.4 Vitrification

Vitrification, that can occur, *e.g.*, during rapid cooling (alluded to in 1.4.2.1.3), can also have a considerable effect on the final phase morphology. For example, if a partially miscible blend is cooled from a single (liquid) phase (as in Figure 1.19), then based on thermodynamic considerations the components would be expected to phase-separate. However, during rapid solidification the individual components do not have sufficient time to do so, leading to a finely intermixed glassy one-phase system. In addition to the vitrification of systems with a tendency for liquid-liquid phase separation, similar observations can be made for blends that can undergo solid-liquid phase separation, thereby also creating a glassy material. This can occur during solvent evaporation and is rendered more complex by the multitude of components and solvent partitioning.[98]

1.4.2.2 Post-deposition processes

As mentioned in the previous section there can be a number of competing and sometimes complex processes that can affect the microstructure of a multi-component system cast from a solvent. In some cases these processes can directly yield microstructures that perform well for photovoltaic applications,[49] but in other cases the microstructure may be non-optimal. In many instances thermal annealing is utilised to manipulate the microstructure *post* deposition. Increasing the temperature of a blend can have effects on both kinetic processes (such as diffusion and

crystallisation) and thermodynamic attributes (such as the miscibility). Therefore thermal annealing can in many cases lead to a number of competing processes.

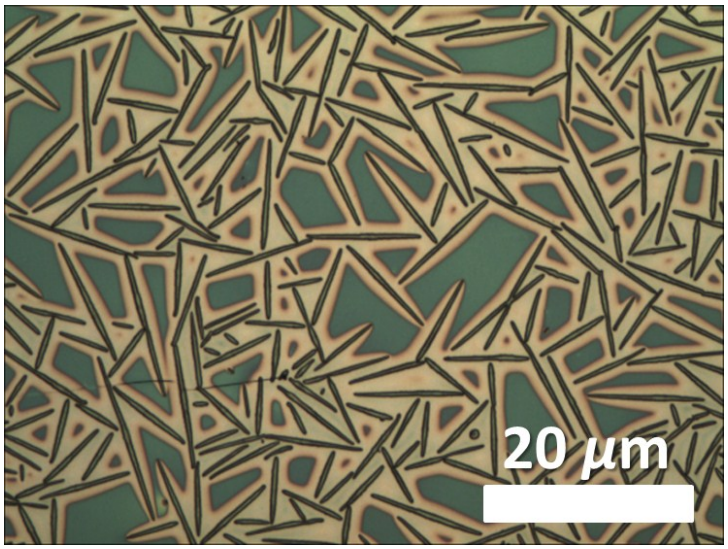


Figure 1.21: Optical transmission micrograph of a P3HT/PCBM bilayer film after annealing at 150 °C, for 20 minutes. Needle-like PCBM crystals can be observed throughout the film. These are surrounded by regions, where the fullerene content has been depleted because of the crystal formation. The darker regions display the areas which still contain a larger amount of fullerene within the polymer matrix.

Post-deposition thermal treatment can in some cases lead to an enhancement of phase separation. For example, in blends comprised of two semicrystalline materials *e.g.* P3HT:PCBM(C60) both components are capable of partly crystallising and aggregating in cast thin films during post-deposition annealing. This can lead to an increase in the fractions of relatively phase-pure regions, hence, depleting intermixed domains from the respective components.

In other cases, thermal annealing has also been shown to promote the diffusion of molecular species, which is a process capable of promoting mixing. For example, among others, Treat *et al*. studied the intermixing of a polymer and fullerene through the use of vertical[52] and lateral[99] bilayer structures. This work highlighted the temperature dependence of intermixing (typically with higher temperatures favouring greater mixing). Additionally the work noted the rapid

diffusion of a fullerene into a neat polymer, quantifying the diffusion coefficient for PCBM(C60) diffusing into P3HT to be 10^{-9} cm^2/s at 110 °C.

To summarise, an example of the competition between different processes (interdiffusion, aggregation/crystallisation) is shown in Figure 1.21. For P3HT/PCBM(C60) bilayers, thermal annealing leads to: firstly, vertical mixing via diffusion of the fullerene. Subsequently, the fullerene crystallises within the polymer matrix forming micron-sized crystals that protrude from the surface of the film. Around each of these crystals there is an observable depletion region of reduced PCBM content. This fullerene depletion phenomena was used by Watts *et al*. to investigate diffusion and also the miscibility limit in polymer:fullerene blends.[100]

1.4.3 Summary

In summary, the active layers in OPV devices present significant challenges from the separate viewpoints of: processing; microstructure and photo-physics. However, in order to develop a holistic understanding of these systems, the interplay between these different aspects must be addressed. This will provide a basis for improvement and feedback of relevant processing protocols, capable of evolving microstructures to provide the desired photo-physical properties within a system.

1.5 Scope and survey of thesis

This thesis addresses the structure/property/processing inter-relationships of different semiconductor binary systems in order to develop a more comprehensive understanding of how processing routes can affect the structural formation processes, what the effect of this is on the phase morphology of such systems and, terminally, how this alters the photo-physical properties such as charge generation.

Chapter 1: placed in context the recent literature and outlines the challenges related to the three areas of processing, structure and photo-physical processes. **Chapter 2**: summarises the materials and experimental methods utilised in the following chapters. **Chapter 3:** investigates in detail the use of depth profile SIMS within the Plastic Electronics area, outlines the experimental methodology and interpretation of measurements to improve understanding of composition-position within organic semiconducting films; and explains the structural formation processes and resulting phase morphology of multi-component systems. **Chapter 4:** explores intermixed phases in organic BHJs in terms of possible microstructural and photo-physical processes in a prototypical binary of P3HT/PCBM. **Chapter 5:** discusses the role of different fullerenes in the formation of vitrified, kinetically trapped phases, and the resultant effect on device performance in OPV blends. **Chapter 6:** builds upon the understanding gained in Chapters 4 and 5 for polymer:fullerene systems and extends this to polymer/polymer systems. The molecular-weight dependence on the structural formation and macroscopic properties are investigated and clear differences reported between systems. **Chapter 7**: further emphasises the influence of processing on the microstructure and photo-physical properties within all polymer semiconducting blends, especially with respect to energy-transfer processes between the two components.

1.6 References

1. K. Braun, *Annual Review of Physical Chemistry*, 1874, 556.
2. E. Braun and S. MacDonald, *Revolution in Miniature: The History and Impact of Semiconductor Electronics*, Cambridge University Press, Cambridge, 1982.
3. Y. Houari, J. Speirs, C. Candelise and R. Gross, *Progress in Photovoltaics: Research and Applications*, 2013.
4. C. Candelise, J. F. Speirs and R. J. K. Gross, *Renewable and Sustainable Energy Reviews*, 2011, **15**, 4972-4981.
5. J. H. Bannock, S. H. Krishnadasan, A. M. Nightingale, C. P. Yau, K. Khaw, D. Burkitt, J. J. M. Halls, M. Heeney and J. C. de Mello, *Advanced Functional Materials*, 2013, **23**, 2123-2129.
6. J. H. Burroughes, *UK Plastic Electronics - Capability Guide*, Electronics, Sensors, Photonics Knowledge Transfer Network, 2013.
7. D. D. Eley, G. D. Partfitt, M. J. Perry and D. H. Taysum, *Transactions of the Faraday Society*, 1952, **2**, 79-86.
8. R. G. Kepler, *Physical Review*, 1960, **119**, 1226-1229.
9. W. J. Siemons, P. E. Bierstedt and R. G. Kepler, *The Journal of Chemical Physics*, 1963, **39**, 3523-3523.
10. A. F. Garito and A. J. Heeger, *Accounts of Chemical Research*, 1974, **7**, 232-240.
11. B. Y. T. J. Kistenmacher, T. E. Phillips and D. O. Cowan, *Acta Crystallographica Section B*, 1974, **B30**, 763-768.
12. C. K. Chiang, C. R. Fincher, Y. W. Park and A. J. Heeger, *Physical Review Letters*, 1977, **39**, 1098-1101.
13. H. Shirakawa, E. J. Louis, A. G. Macdiarmid, C. K. Chiang and A. J. Heeger, *Journal of the Chemical Society, Chemical Communications*, 1977, **16**, 578-580.
14. J. H. Burroughes, D. D. C. Bradley, A. R. Brown, R. N. Marks, K. Mackay, R. H. Friend, P. L. Burn and A. B. Holmes, *Nature*, 1990, **347**, 539-541.
15. H. S. White, G. P. Kittlesen and M. S. Wrighton, *Journal of the American Chemical Society*, 1984, **106**, 5375-5377.
16. A. Tsumura, H. Koezuka and T. Ando, *Applied Physics Letters*, 1986, **49**, 1210-1212.
17. C. W. Tang, *Applied Physics Letters*, 1986, **48**, 183-183.
18. P. Peumans and S. R. Forrest, *Applied Physics Letters*, 2001, **79**, 126-128.
19. P. E. Shaw, A. Ruseckas and I. D. W. Samuel, *Advanced Materials*, 2008, **20**, 3516-3520.

20. O. V. Mikhnenko, H. Azimi, M. Scharber, M. Morana, P. W. M. Blom and M. A. Loi, *Energy & Environmental Science*, 2012, **5**, 6960-6960.
21. N. S. Sariciftci, L. Smilowitz, a. J. Heeger and F. Wudl, *Science*, 1992, **258**, 1474-1476.
22. G. Yu, J. Gao, J. C. Hummelen and A. J. Heeger, *Science*, 1995, **270**, 1789-1789.
23. P. Schilinsky, C. Waldauf and C. J. Brabec, *Applied Physics Letters*, 2002, **81**, 3885-3885.
24. M. T. Dang, L. Hirsch and G. Wantz, *Advanced Materials*, 2011, **23**, 3597-3602.
25. F. Padinger, R. S. Rittberger and N. S. Sariciftci, *Advanced Functional Materials*, 2003, **13**, 85-88.
26. W. Ma, C. Yang, X. Gong, K. Lee and A. J. Heeger, *Advanced Functional Materials*, 2005, **15**, 1617-1622.
27. C. Müller, T. Ferenczi, M. Campoy-Quiles, J. M. Frost, D. D. C. Bradley, P. Smith, N. Stingelin-Stutzmann and J. Nelson, *Advanced Materials*, 2008, **20**, 3510-3515.
28. Y. Kim, S. Cook, S. M. Tuladhar, S. a. Choulis, J. Nelson, J. R. Durrant, D. D. C. Bradley, M. Giles, I. McCulloch, C.-S. Ha and M. Ree, *Nature Materials*, 2006, **5**, 197-203.
29. M. Campoy-Quiles, T. Ferenczi, T. Agostinelli, P. G. Etchegoin, Y. Kim, T. D. Anthopoulos, P. N. Stavrinou, D. D. C. Bradley and J. Nelson, *Nature Materials*, 2008, **7**, 158-158.
30. R. J. Kline, M. D. McGehee, E. N. Kadnikova, J. Liu and J. M. J. Fréchet, *Advanced Materials*, 2003, **15**, 1519-1522.
31. R. J. Kline, M. D. McGehee, E. N. Kadnikova, J. Liu, J. M. J. Frechet and M. F. Toney, *Macromolecules*, 2005, **38**, 3312-3319.
32. a) Y. Liang, Z. Xu, J. Xia, S.-T. Tsai, Y. Wu, G. Li, C. Ray and L. Yu*, J. Am. Chem. Soc*. 2009, **131**, 7792–7799. b) Y. Liang, Z. Xu, J. Xia, S.-T. Tsai, Y. Wu, G. Li, C. Ray and L. Yu, *Advanced Materials*, 2010, **22**, E135-138.
33. M. C. Scharber, M. Koppe, J. Gao, F. Cordella, M. a. Loi, P. Denk, M. Morana, H.-J. Egelhaaf, K. Forberich, G. Dennler, R. Gaudiana, D. Waller, Z. Zhu, X. Shi and C. J. Brabec, *Advanced Materials*, 2010, **22**, 367-370.
34. K. W. Chou, B. Yan, R. Li, E. Q. Li, K. Zhao, D. H. Anjum, S. Alvarez, R. Gassaway, A. Biocca, S. T. Thoroddsen, A. Hexemer and A. Amassian, *Advanced Materials*, 2013, **25**, 1923-1929.
35. H. J. Kim, H. H. Lee and J.-J. Kim, *Macromolecular Rapid Communications*, 2009, **30**, 1269-1273.
36. N. D. Treat, C. G. Shuttle, M. F. Toney, C. J. Hawker and M. L. Chabinyc, *Journal of Materials Chemistry*, 2011, **21**, 15224-15224.
37. N. Shin, L. J. Richter, A. A. Herzing, R. J. Kline and D. M. DeLongchamp, *Advanced Energy Materials*, 2013, **3**, 938-948.

38. M. Pfannmöller, H. Flügge, G. Benner, I. Wacker, C. Sommer, M. Hanselmann, S. Schmale, H. Schmidt, F. A. Hamprecht, T. Rabe, W. Kowalsky and R. R. Schröder, *Nano Letters*, 2011, **11**, 3099-3107.

39. B. A. Collins, Z. Li, J. R. Tumbleston, E. Gann, C. R. McNeill and H. Ade, *Advanced Energy Materials*, 2013, **3**, 65-74.

40. C. R. McNeill, B. Watts, S. Swaraj, H. Ade, L. Thomsen, W. Belcher and P. C. Dastoor, *Nanotechnology*, 2008, **19**, 424015-424015.

41. H. Yan, B. A. Collins, E. Gann, C. Wang, H. Ade and C. R. McNeill, *ACS Nano*, 2012, **6**, 677-688.

42. D. Chen, A. Nakahara, D. Wei, D. Nordlund and T. P. Russell, *Nano Letters*, 2011, **11**, 561-567.

43. N. C. Cates, R. Gysel, Z. Beiley, C. E. Miller, M. F. Toney, M. Heeney, I. McCulloch and M. D. McGehee, *Nano Letters*, 2009, **9**, 4153-4157.

44. D. S. Germack, C. K. Chan, R. J. Kline, D. a. Fischer, D. J. Gundlach, M. F. Toney, L. J. Richter and D. M. DeLongchamp, *Macromolecules*, 2010, **43**, 3828-3836.

45. C. Piliego, T. W. Holcombe, J. D. Douglas, C. H. Woo, P. M. Beaujuge and J. M. J. Fréchet, *Journal of the American Chemical Society*, 2010, **132**, 7595-7597.

46. C. M. Amb, S. Chen, K. R. Graham, J. Subbiah, C. E. Small, F. So and J. R. Reynolds, *Journal of the American Chemical Society*, 2011, **133**, 10062-10065.

47. a) H. Bronstein, Z. Chen, R. S. Ashraf, W. Zhang, J. Du, J. R. Durrant, P. S. Tuladhar, K. Song, S. E. Watkins, Y. Geerts, M. M. Wienk, R. A. J. Janssen, T. Anthopoulos, H. Sirringhaus, M. Heeney and I. McCulloch, *Journal of the American Chemical Society*, 2011, **133**, 3272-3275. b) S. Cho, N. Coates, J. S. Moon, S. H. Park, A. Roy, S. Beaupre, D. Moses, M. Leclerc, K. Lee and A. J. Heeger, *Nature Photonics*, 2009, **3**, 297-303.

48. C. Cabanetos, A. El Labban, J. A. Bartelt, J. D. Douglas, W. R. Mateker, J. M. J. Fréchet, Michael D. McGehee and P. M. Beaujuge*, Journal of the American Chemical Society*, 2013, **135**, pp 4656–4659.

49. H. Zhong, Z. Li, F. Deledalle, E. C. Fregoso, M. Shahid, Z. Fei, C. B. Nielsen, N. Yaacobi-Gross, S. Rossbauer, T. D. Anthopoulos, J. R. Durrant and M. Heeney, *Journal of the American Chemical Society*, 2013, **135**, 2040-2043.

50. J. Peet, J. Y. Kim, N. E. Coates, W. L. Ma, D. Moses, A. J. Heeger and G. C. Bazan, *Nature Materials*, 2007, **6**, 497-500.

51. F. C. Jamieson, E. B. Domingo, T. McCarthy-Ward, M. Heeney, N. Stingelin and J. R. Durrant, *Chemical Science*, 2012, 485-492.

52. N. D. Treat, M. A. Brady, G. Smith, M. F. Toney, E. J. Kramer, C. J. Hawker and M. L. Chabinyc, *Advanced Energy Materials*, 2011, **1**, 82-89.

53. B. A. Collins, Z. Li, C. R. McNeill and H. Ade, *Macromolecules*, 2011, **44**, 9747-9751.
54. P. Westacott, J. R. Tumbleston, S. Shoaee, S. Fearn, J. H. Bannock, J. B. Gilchrist, S. Heutz, J. DeMello, M. Heeney, H. Ade, J. Durrant, D. S. McPhail and N. Stingelin, *Energy & Environmental Science*, 2013, **6**, 2756-2764.
55. W. Yin and M. Dadmun, *ACS Nano*, 2011, 4756-4768.
56. A. C. Mayer, S. R. Scully, B. E. Hardin, M. W. Rowell and M. D. McGehee, *Materials Today*, 2007, **10**, 28-28.
57. C. Silva, *Nature Materials*, 2013, **12**, 5-6.
58. J. Piris, T. E. Dykstra, A. A. Bakulin, P. H. M. V. Loosdrecht, W. Knulst, M. T. Trinh, J. M. Schins and L. D. A. Siebbeles, *The Journal of Physical Chemistry C*, 2009, **113**, 14500-14506.
59. G. Grancini, M. Maiuri, D. Fazzi, A. Petrozza, H. J. Egelhaaf, D. Brida, G. Cerullo and G. Lanzani, *Nature Materials*, 2012, **11**, 1-5.
60. J. Lee, K. Vandewal, S. R. Yost, M. E. Bahlke, L. Goris, M. a. Baldo, J. V. Manca and T. Van Voorhis, *Journal of the American Chemical Society*, 2010, **132**, 11878-11880.
61. K. Vandewal, S. Albrecht, E. T. Hoke, K. R. Graham, J. Widmer, J. D. Douglas, M. Schubert, W. R. Mateker, J. T. Bloking, G. F. Burkhard, A. Sellinger, J. M. J. Frechet, A. Amassian, M. K. Riede, M. D. McGehee, D. Neher and A. Salleo, *Nature Materials*, 2014, **13**, 63-68.
62. D. P. McMahon, D. L. Cheung and A. Troisi, *The Journal of Physical Chemistry Letters*, 2011, **2**, 2737-2741.
63. D. C. Coffey, A. J. Ferguson, N. Kopidakis and G. Rumbles, *ACS Nano*, 2010, **4**, 5437-5445.
64. B. A. Gregg, *The Journal of Physical Chemistry Letters*, 2011, **2**, 3013-3015.
65. R. A. Street, M. Schoendorf, A. Roy and J. H. Lee, *Physical Review B*, 2010, **81**, 205307.
66. a) B. C. Thompson and J. M. J. Fréchet, *Angewandte Chemie*, 2008, **47**, 58-77. b) H. Kim, J. Young Kim, K. Lee, Y. Park, Y. Jin and H. Suh, *Current Applied Physics*, 2001, **1**, 139-143.
67. B. A. Collins, E. Gann, L. Guignard, X. He, C. R. McNeill and H. Ade, *The Journal of Physical Chemistry Letters*, 2010, **1**, 3160-3166.
68. J. A. Bartelt, Z. M. Beiley, E. T. Hoke, W. R. Mateker, J. D. Douglas, B. A. Collins, J. R. Tumbleston, K. R. Graham, A. Amassian, H. Ade, J. M. J. Fréchet, M. F. Toney and M. D. McGehee, *Advanced Energy Materials*, 2013, **3**, 364-374.
69. S. Shoaee, M. P. Eng, E. Espíldora, J. L. Delgado, B. Campo, N. Martín, D. Vanderzande and J. R. Durrant, *Energy & Environmental Science*, 2010, **3**, 971-971.
70. T. M. Clarke, A. Ballantyne, S. Shoaee, Y. W. Soon, W. Duffy, M. Heeney, I. McCulloch, J. Nelson and J. R. Durrant, *Advanced Materials*, 2010, **22**, 5287-5291.

71. P. J. Flory, *The Principles of Polymer Chemistry*, Cornell University Press, New York, 1953, ch. 2, pp. 48-50.

72. H. Sirringhaus, P. J. Brown, R. H. Friend, M. M. Nielsen, K. Bechgaard, A. J. H. Spiering, R. A. J. Janssen, E. W. Meijer, P. Herwig and D. M. de Leeuw, *Nature*, 1999, **401**, 685-688.

73. B. S. Ong, Y. Wu, P. Liu and S. Gardner, *Journal of the American Chemical Society*, 2004, **126**, 3378-3379.

74. I. McCulloch, M. Heeney, C. Bailey, K. Genevicius, I. Macdonald, M. Shkunov, D. Sparrowe, S. Tierney, R. Wagner, W. Zhang, M. L. Chabinyc, R. J. Kline, M. D. McGehee and M. F. Toney, *Nature Materials*, 2006, **5**, 328-333.

75. P. J. Flory, *The Principles of Polymer Chemistry*, Cornell University Press, New York, 1953, ch. 13, pp. 564-565.

76. J. Rivnay, R. Noriega, J. E. Northrup, R. J. Kline, M. F. Toney and A. Salleo, *Physical Review B*, 2011, **83**, 121306-121306.

77. F. P. V. Koch, J. Rivnay, S. Foster, C. Müller, J. M. Downing, E. Buchaca-Domingo, P. Westacott, L. Yu, M. Yuan, M. Baklar, Z. Fei, C. Luscombe, M. A. McLachlan, M. Heeney, G. Rumbles, C. Silva, A. Salleo, J. Nelson, P. Smith and N. Stingelin, *Progress in Polymer Science*, 2013, **38**, 1978-1989.

78. A. Salleo, *Materials Today*, 2007, **10**, 38-45.

79. M. A. Baklar, F. Koch, A. Kumar, E. B. Domingo, M. Campoy-Quiles, K. Feldman, L. Yu, P. Wobkenberg, J. Ball, R. M. Wilson, I. McCulloch, T. Kreouzis, M. Heeney, T. Anthopoulos, P. Smith and N. Stingelin, *Advanced Materials*, 2010, **22**, 3942-3947.

80. R. Noriega, J. Rivnay, K. Vandewal, F. P. V. Koch, N. Stingelin, P. Smith, M. F. Toney and A. Salleo, *Nature Materials*, 2013, **12**, 1038-1044.

81. D. R. Blasini, J. Rivnay, D.-M. Smilgies, J. D. Slinker, S. Flores-Torres, H. C. D. Abruna and G. G. Malliaras, *Journal of Materials Chemistry*, 2007, **17**, 1458-1458.

82. B. Watts, T. Schuettfort and C. R. McNeill, *Advanced Functional Materials*, 2011, **21**, 1122-1131.

83. B. A. Collins, J. E. Cochran, H. Yan, E. Gann, C. Hub, R. Fink, C. Wang, T. Schuettfort, C. R. McNeill, M. L. Chabinyc and H. Ade, *Nature Materials*, 2012, **11**, 536-543.

84. C. J. Takacs, N. D. Treat, S. Krämer, Z. Chen, A. Facchetti, M. L. Chabinyc and A. J. Heeger, *Nano Letters*, 2013, **13**, 2522-2527.

85. J. Rivnay, M. F. Toney, Y. Zheng, I. V. Kauvar, Z. Chen, V. Wagner, A. Facchetti and A. Salleo, *Advanced Materials*, 2010, **22**, 4359-4363.

86. T. M. Clarke, A. M. Ballantyne, J. Nelson, D. D. C. Bradley and J. R. Durrant, *Advanced Functional Materials*, 2008, **18**, 4029-4035.
87. C. Groves, *Energy & Environmental Science*, 2013, **6**, 1546-1546.
88. F. Wöhler, *Annalen Chemie Pharmacie*, 1844, **51**, 143-163.
89. C. R. Patrick and G. S. Prosser, *Nature*, 1960, **187**, 1021-1021.
90. A. C. Mayer, M. F. Toney, S. R. Scully, J. Rivnay, C. J. Brabec, M. Scharber, M. Koppe, M. Heeney, I. McCulloch and M. D. McGehee, *Advanced Functional Materials*, 2009, **19**, 1173-1179.
91. S. Kouijzer, J. J. Michels, M. van den Berg, V. S. Gevaerts, M. Turbiez, M. M. Wienk and R. A. J. Janssen, *Journal of the American Chemical Society*, 2013, **135**, 12057-12067.
92. A. Galeski, *Progress in Polymer Science*, 2003, **28**, 1643-1699.
93. M. Blomenhofer, S. Ganzleben, D. Hanft, H.-w. Schmidt, M. Kristiansen, P. Smith, K. Stoll, D. Ma and K. Hoffmann, 2005, 3688-3695.
94. J. Varga, I. Mudra and G. W. Ehrenstein, *Journal of Applied Polymer Science*, 1999, **74**, 2357-2368.
95. N. D. Treat, J. A. N. Malik, O. Reid, L. Yu, C. G. Shuttle, G. Rumbles, C. J. Hawker, M. L. Chabinyc, P. Smith and N. Stingelin, *Nature Materials*, 2013, **12**, 628-633.
96. S. Goffri, C. Muller, N. Stingelin-Stutzmann, D. W. Breiby, C. P. Radano, J. W. Andreasen, R. Thompson, R. A. J. Janssen, M. M. Nielsen, P. Smith and H. Sirringhaus, *Nature Materials*, 2006, **5**, 950-950.
97. D. M. Delongchamp, B. M. Vogel, Y. Jung, M. C. Gurau, C. A. Richter, O. A. Kirillov, J. Obrzut, D. A. Fischer, S. Sambasivan, L. J. Richter and E. K. Lin, *Chemistry of Materials*, 2005, **17**, 5610-5612.
98. Y. Funaki, K. Kumano, T. Nakao, H. Jinnai, H. Yoshida, K. Kimishima and K. Tsutsumi, *Polymer*, 1999, **40**, 7147-7156.
99. N. D. Treat, T. E. Mates, C. J. Hawker, E. J. Kramer and M. L. Chabinyc, *Macromolecules*, 2013, **46**, 1002-1007.
100. B. Watts, W. J. Belcher, L. Thomsen, H. Ade and P. C. Dastoor, *Macromolecules*, 2009, **42**, 8392-8397.

Chapter 2

Experimental methods

2.1 Materials

Within this study three molecular weights of regio-regular poly(3-hexylthiophene-2,5-diyl) (P3HT) have been used, L-P3HT, M-P3HT and H-P3HT, the details are of these are displayed in Table 2.1. These were kindly supplied by James Bannock and Martin Heeney of Imperial College London, in addition a regio-random P3HT (RRa-P3HT) was purchased from Sigma-Aldrich and used as received. Poly(3-hexylselenophene-2,5-diyl) (P3HS) was synthesised by Mohammed Al-Hashimi (Imperial College London) and provided in two molecular weights (properties displayed in Table 2.1). In addition a diketopyrrolopyrrole (DPP) derivative (DPP-TT-T) was kindly supplied by Weimin Zhang (Imperial College London). Molar mass distribution was determined via gel permeation chromatography (GPC) in chlorobenzene and calibrated against polystyrene standards.

Table 2.1: Summary of the properties of the polymers used in this thesis. The number-average molecular weight (M_n), weight-average molecular weight (M_w) and regioregularity (RR) are displayed. RR was determined via integration of the methylene region in ^{1}H-NMR, not accounting for end-group effects.

Material	M_n (kg/mol)	M_w (kg/mol)	RR (%)
L-P3HT	5.1	7.2	>95
M-P3HT	26	48	>98
H-P3HT	70	135	99
RRa-P3HT	27	46	-
L-P3HS	8.3	16	95
H-P3HS	52	100	97
DPP-TT-T	24	89	-

The different fullerene derivatives used within this thesis: [6,6]-phenyl-C61-butyric acid methyl ester (PCBM), bis(1-[3-(methoxycarbonyl)propyl]-1-phenyl)-[6.6]C62 (bis-PCBM), 1',1'',4',4''-tetrahydro-di[1,4]methanonaphthaleno[5,6]fullerene-C60 (ICBA) and their deuterated analogs (>

99.5% purity) were kindly supplied by Solenne, BV, the Netherlands and used as received (structures shown in Figure 5.1).

2.2 Methods

2.2.1 Steady-state UV-vis absorption spectroscopy (UV-vis)

UV-vis absorption is a commonly used optical technique capable of determining photon absorption of materials over a range of wavelengths (typically 200-1400 nm). The technique can be applied to samples of thin solid films or dilute solutions of a material. The method utilises the difference in incident and transmitted light within a sample to derive the absorption based on the Beer-Lambert Law (Equation 2.1) with the additional assumption that absorption is linear with concentration (Equation 2.2), where *A* is the absorbance, *I* is the transmitted intensity, I_0 is the incident intensity, *L* is the path length (or thickness of sample) and α is the absorption coefficient.

$$\boldsymbol{A = -log(I/I_0)} \qquad \textit{Equation 2.1}$$

$$\boldsymbol{A = \alpha L} \qquad \textit{Equation 2.2}$$

Typically photon absorption in this energy range is related to electronic transitions within the material (for example exciting an electron from the highest molecular orbital (HOMO) to the lowest unoccupied molecular orbital (LUMO) - shown as *A* in Figure 2.1. While the energetics of these transitions are heavily influenced by the intrinsic material properties there can also be significant contribution from the molecular surroundings, whether this is polarity of solvent or solid-

state microstructure. Due to the sensitivity to local environment, the technique can provide a range of information related to molecular interactions within the sample.

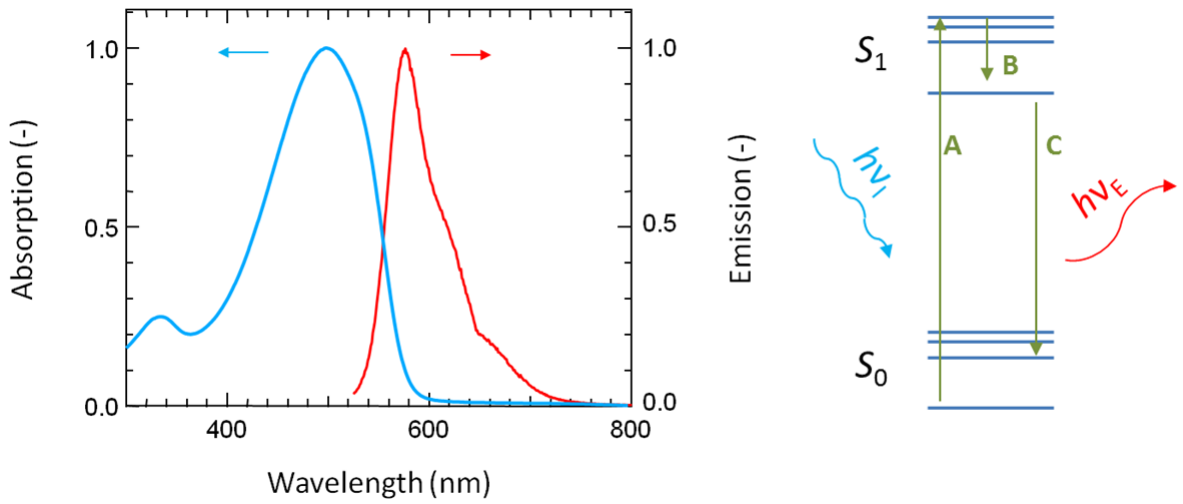


Figure 2.1: Optoelectronic properties of a prototypical organic semiconductor. **Left**: Typical absorption (blue) and emission (red) spectra of a semiconducting polymer. **Right**: Simplified Jablonski diagram depicting the ground and first electronically excited singlet states of a system, S_0 and S_1 respectively. This diagram shows three different types of energetic transition (A-C) occurring. **A**: Photon absorption leading to promotion of an electron from $S_0 \rightarrow S_1$. **B**: Vibrational relaxation to the lowest vibrational state of S_1. **C**: Electronic relaxation accompanied by photon emission ($S_1 \rightarrow S_0$).

2.2.2 Steady-state photoluminescence spectroscopy (PL)

Following an electronic excitation (typically by absorption of a photon, A in Figure 2.1), after vibronic relaxation to the lowest vibrational mode within the electronically excited state (B in Figure 2.1), it is possible for electronic relaxation to occur. One of the pathways for this is via a radiative decay process (*e.g.* photoluminescence), which leads to emission of a photon (C in Figure 2.1). The spectral shape and intensity can be greatly influenced by the local environment of the material (*e.g.* aggregation, locality to quenching sites, energetic distribution of emission sites) and hence can yield valuable and sensitive information related to the local environment. In order to make quantitative comparisons between samples the intensity of emission can be corrected for the density of absorbed photons using Equation 2.3, where *A* is the absorption at the excitation wavelength.

$$PL_{corr} = PL_{raw}/(1 - 10^{-A}) \qquad \textit{Equation 2.3}$$

2.2.3 Transient absorption spectroscopy (TAS)

TAS is a spectroscopic pump-probe technique used to study transient species generated after photo-excitation. The technique works by firstly optically exciting a material using a short laser pulse (pump). After this pump, a probe beam of different (typically longer) wavelength is used to measure the change in transmission ($\Delta T/T$), from which the change in absorption at that given wavelength is deduced. A simplified representation of the experimental setup is shown in Figure 2.2. By mapping a range of wavelengths as a function of time it can be possible to assign the features within the absorption spectra to different species such as: polarons; bipolarons and charge transfer states. Once a feature such as a polaron has been identified, it is possible to study the relative quantity and decay dynamics of such excited states by observing the change in absorption intensity as a function of time.

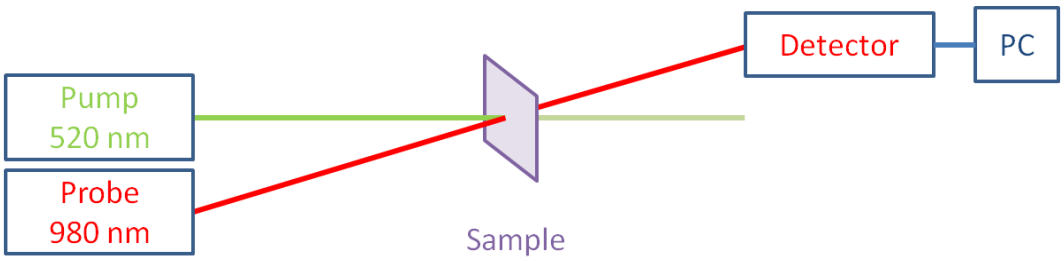


Figure 2.2: Schematic representation of the experimental setup used for transient absorption spectroscopy. The pump beam is focused onto the sample, the resulting perturbation of the electronic states is observed optically using the probe.

2.2.4 Differential scanning calorimetry (DSC)

DSC is a thermal-analytical technique capable of providing quantitative information of different thermal transitions undergone by a material upon heating or cooling. The technique works by monitoring the heat required to change the temperature of a sample in a given time. Expressions for the rate of temperature change and the rate of supply of energy are displayed in Equation 2.4 and Equation 2.5 respectively, where k_T is the rate of temperature change, T is temperature, k_Q is the rate of heat flow change and Q is heat flow.

DSC works by recording the difference in supply of energy (between as sample and a reference) required to change their temperature at a constant rate. If the temperature changes at a constant rate then *(i.e.* if no first order transitions are encountered) the heat flow to the sample will depend only upon the heating rate and the specific heat capacity of the material (C_p), and follow a linear relationship as described by Equation 2.6.

$$\boldsymbol{k_T = dT/dt} \qquad \textit{Equation 2.4}$$

$$\boldsymbol{k_Q = dQ/dt} \qquad \textit{Equation 2.5}$$

$$\boldsymbol{C_P = dQ/dT} \qquad \textit{Equation 2.6}$$

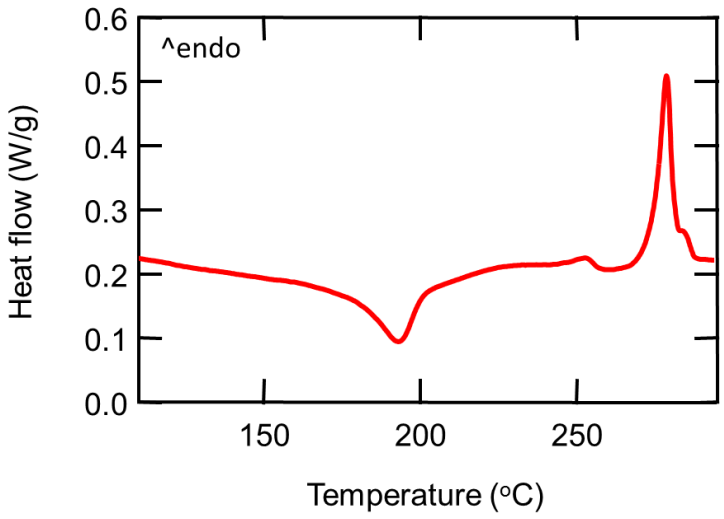


Figure 2.3: A differential scanning calorimetry trace of the first heating of a solution cast fullerene derivative, showing an exothermic transition ~180 °C (cold crystallisation), and two endothermic transitions (~250 and 280 °C).

When heating a material in this manner it is possible to extract the *Cp* from the gradient of the heat flow against temperature plot for a sample. In addition to this, a wealth of other information can be obtained by the technique, including detailed information related to phase transitions (such as melting, crystallisation *etc.*). When a first order endothermic transition is encountered, energy must be supplied in order to drive the phase change, as would be the case for a melting transition. Meaning the heat-flow to the sample will be greater during an endothermic transition than when no phase change occurs (as seen on Figure 2.3). The converse is true for exothermic transitions, where thermal energy is liberated from the sample, resulting in less energy being required to change the temperature. The integral of this transition, in conjunction with the heating rate can be used to derive the amount of energy required or liberated during the phase change. This energy value can then be normalised to the mass of the component of interest to yield the enthalpy per gram. Further to melting transitions, glass transitions in certain materials can be observed. Around the glass transition of a material, the heat capacity typically exhibits a rapid change, as discussed previously a change in heat capacity will result in a change in the gradient of

heat flow as a function of temperature. This change in gradient is often observed as a “kink” in the thermogram.

2.2.5 Wide-angle X-ray scattering (WAXS)

WAXS is a technique capable of probing structural order within solid samples. The typical periodic distance probed with WAXS is approximately 10^{-10} – 10^{-8} m. The technique works by shining a collimated monochromatic X-ray source onto a sample. If crystallographic planes within the sample satisfy Braggs law (Equation 2.7) then diffraction will occur:

$$n\lambda = 2d\,sin\theta \qquad \textit{Equation 2.7}$$

where n is an integer, λ being the X-ray wavelength and d the periodic distance between crystal planes. A conventional way to probe this is to vary the angle of a point detector and observe the change in diffraction intensity (*e.g*. Bragg-Bretano configuration), an example of such a diffractogram is shown in Figure 2.4.

Other than giving information on the unit cell, WAXS is capable of probing other characteristics including: degree of crystallinity, crystalline texture, crystallite size and paracrystallinity of materials. WAXS measurements within this thesis were performed on one of the following two setups. Imperial College London using a Philips X’Pert Pro MRD with a Cu-K_α (λ = 0.15418 nm) source. Operation was carried in a Bragg-Bretano theta-2theta configuration.

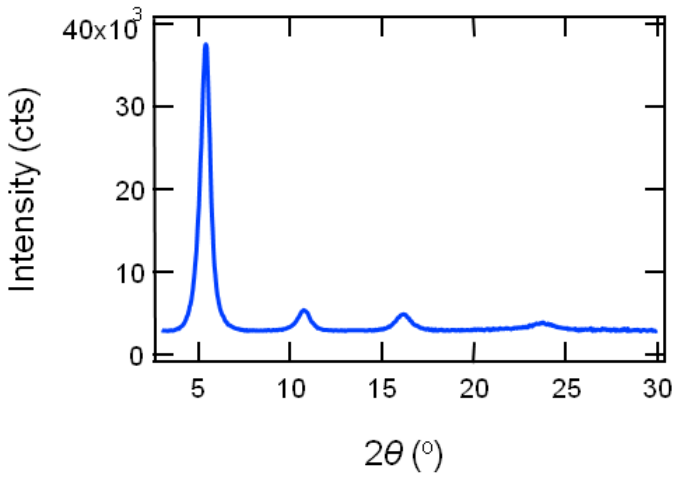


Figure 2.4: X-ray diffractogram of a polythiophene derivative recorded under Bragg-Bretano, θ — 2θ, configuration. The diffractogram shows a first order diffraction at ~5 °, corresponding to the lamellar stack. Higher order reflections of this are observed at ~11 ° and ~17 ° and another feature, corresponding to the π-stack is observed at ~23 °.

2.2.5.1 Grazing-angle incidence wide-angle X-ray scattering (GIWAXS)

In the field of plastic electronics the thinness of films (*e.g.* 10-100s nm) and importance of molecular/segmental orientation relative to a substrate mean that a conventional Bragg-Bretano configuration may not always be the most appropriate choice. One technique capable of probing orientation in thin-film geometries, whilst probing a sufficiently large volume of the sample is GIWAXS. This technique utilises an incident X-ray beam almost parallel to the substrate (as shown in Figure 2.5). If the sample has preferential orientation of any periodicity, here exemplified as an edge-on structure (*i.e.* the edge of the lamellar is perpendicular to the substrate), then the resultant coherent scatter from the two periodicities (d_z and d_{xy}) will typically differ, resulting in scatter in different planes. This difference in scatter can be observed at the detector plate in the Q_{xy} and Qz directions.

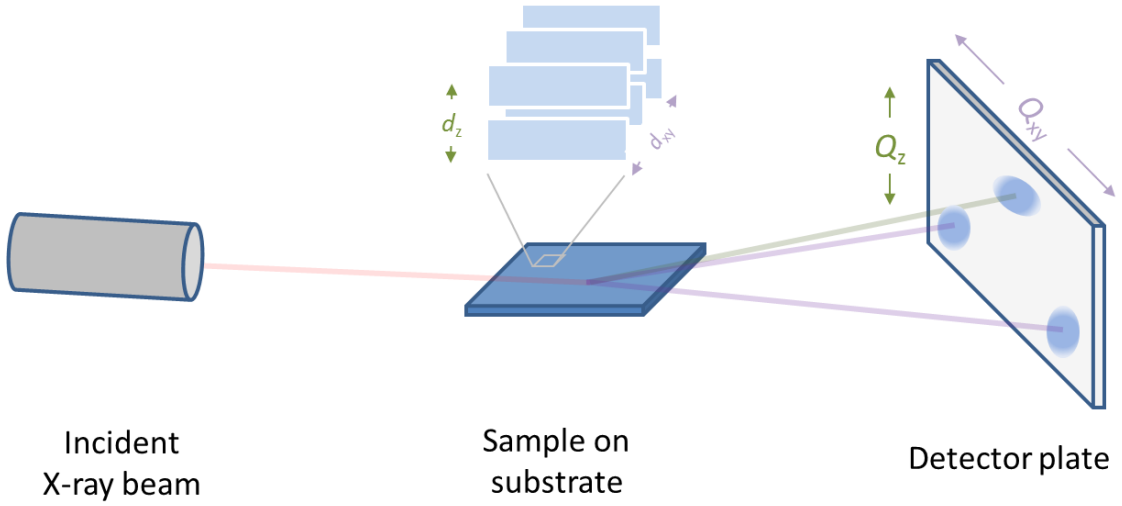


Figure 2.5: Schematic representation of grazing-angle incidence wide-angle X-ray scattering (GIWAXS) configuration for a thin-film sample showing edge-on orientation. The incident X-ray beam approaches the sample from a very shallow angle (typically in the region of 0.1 ^{o}). The incident beam may then interact with periodic features within the sample and result in scatter within both the Q_{xy} and *Qz* planes, which can be observed on the detector plate.

2.2.6 Near-edge X-ray absorption fine structure (NEXAFS)

NEXAFS is an electromagnetic absorption technique whereby X-rays, typically within the range of 200-400 eV, are shone onto a sample and the spectral transmission is measured. The majority of organic materials have core to anti-bonding electronic transitions within this regime (*e.g.* relating *s* → π* and *s* → σ*). Due the high sensitivity of the anti-bonding orbitals energy to the atoms present and bonding within the molecule NEXAFS is able to discern the characteristic "finger-print" of different organic materials. With the production of appropriate reference samples (*i.e.* neat materials with known optical density and thickness) it is possible to quantitatively discern the composition of a blend of two known materials.

2.2.7 Secondary ion mass spectrometry (SIMS)

SIMS is a branch of chemical analysis capable of distinguishing elemental, isotopic and molecular composition at, or close to, a surface. The technique utilises a primary (typically an ionic)

source, such as a liquid metal ion gun (LMIG) which is focused onto a sample. The bombardment of primary ions upon the surface can lead to the formation of liberated secondary ions (SIs) that may then be collected and analysed in a mass spectrometer. Although the observation of secondary ions generated via primary ion sources was observed over a century ago,[2] it was not until the 1960-70s when the technique became more widespread as an analytical tool, due to improvements in manufacturing techniques and vacuum technology.

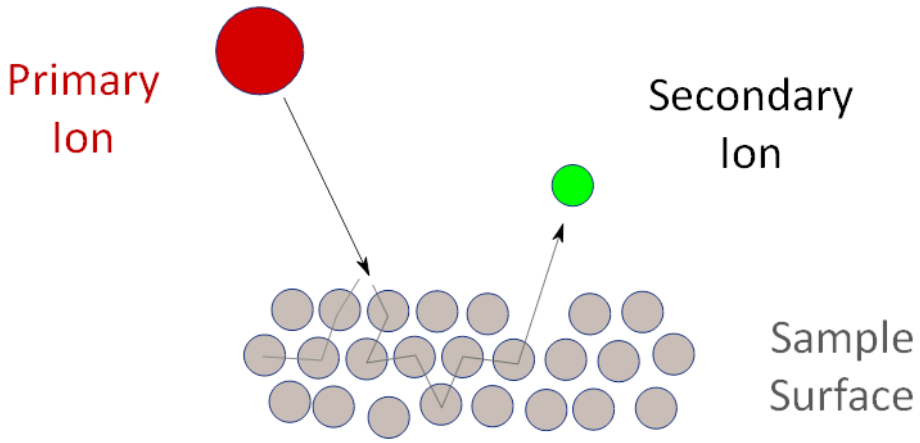


Figure 2.6: Schematic representation of a collision event that can lead to the formation of a liberated secondary ion capable of being captured in a detector within the SIMS process. The primary ion (red) impacts upon the sample surface (grey) thereby transferring energy to the sample, which is then distributed through different atoms (grey lines). This process can lead to the ejection of a secondary ion from close to the surface (green), which it is then possible to observe with an analyser.

In order to carry out a measurement with SIMS a number of processes need to occur. The key points relating to generation of secondary ions are shown schematically in Figure 2.6. Firstly, the primary ions need to be collimated and accelerated to an appropriately high energy, typically on the order of keV. This beam (represented as the red sphere in Figure 2.6) is focused onto a surface of the solid sample. The high energy of the impacting ions can cause elastic and inelastic collisions transferring some of the primary ions' energy to the particles in and around the surface (depicted by the grey lines shown within the sample in Figure 2.6). This energy transfer can result in a number of processes, including breaking of chemical bonds, thermalisation of the sample, ionisation and removal

of species from around the surface (depicted as the green particle in Figure 2.6). Due to these multiple collision processes the location of the emitted particles can be up to 10 nm away from the initial impact of the primary ion.[3]

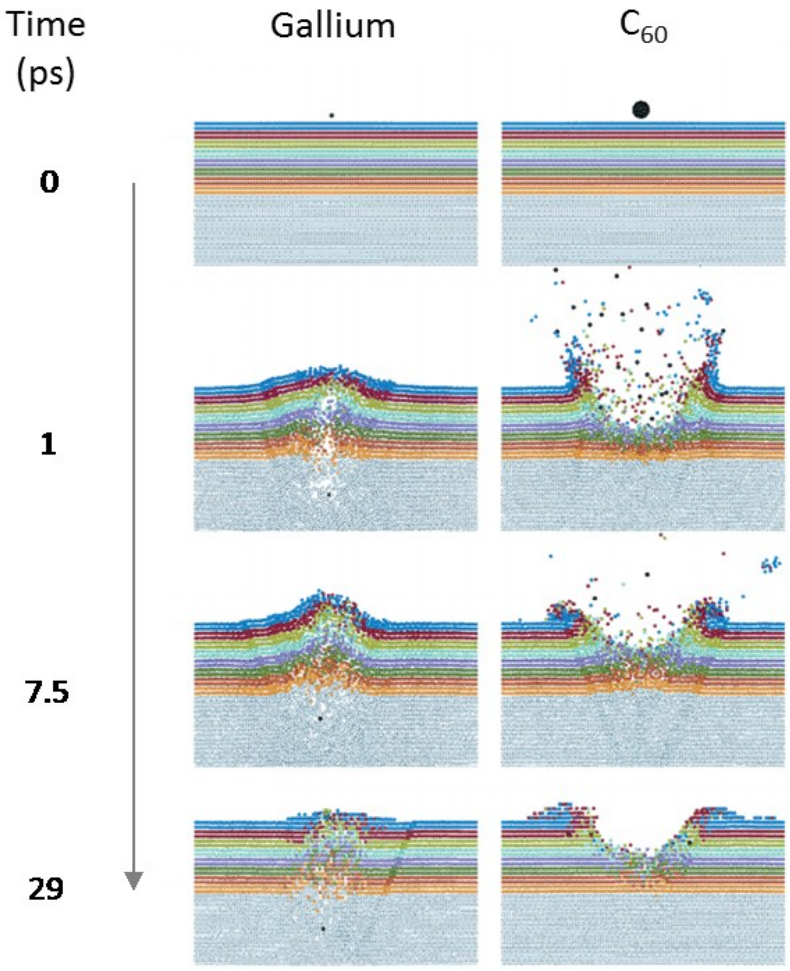


Figure 2.7: Cross-sectional view of the structural effect of surface bombardment with 15 keV primary ions of Ga (left) and C_{60} (right), showing the greater depth of penetration and damage caused by the Ga ion. Colouring represents original atomic layering (adapted from Potswa *et al*., reference 4).

Over the last decade there has been significant development of cluster ion sources, which enable much less destructive analysis of softer/molecular materials, such as organic, polymeric and biological samples.[4] These sources work by using charged particles comprised of multiple atoms clustered together with a typically low integer positive charge. The main advantage of this type of

source is that the kinetic energy of the particle is distributed over a number of atoms resulting in multiple localised lower energy impacts as opposed to one higher energy impact from a single charged atom, an example of which is shown in Figure 2.7. The result of such multiple impacts is reduced damage to the molecular structure meaning much larger fragments can be "lifted" from the surface intact, thereby increasing the ion yields of these larger fragments. This is very useful for the differentiation of materials where the chemical bonding *(e.g*. polymer blends) rather than elemental composition is different. Examples of cluster sources include: sulphur hexafluoride (SF_6^-),[5] bismuth-3 (Bi_3^+),[6] fullerene (C_{60}^+),[7] gold (Au_n^+) [8]and argon (Ar_{500}^+).[9, 10]

2.2.1 Depth profile – SIMS (D-SIMS)

The application of SIMS to surfaces allows sensitive compositional information to be gained, but it is limited to the composition local to the exposed face (static SIMS). For many systems, including a multitude of thin-film samples, it is desirable to gain an understanding of how composition varies through the depth of the film; for example, in the Plastic Electronics area, where the thin-film microstructure plays a critical role in performance of many devices.[11]

Through the use of an additional ion source known as a sputter beam it is possible to depth profile through the sample and thereby measure mass spectra as a function of depth. The three key steps of this process are outlined in Figure 2.8. The first step in depth profiling is to raster the sputter beam over the sputter area (typically a square with side length 250-500 µm). The sputter beam is generally of much higher energy than the analytical beam and results in the removal of a far greater quantity of material. It is also worthwhile to highlight that in addition to removing a large amount of material, the sputter beam may cause surface chemistry of the sample affecting the ion yields, hence careful selection of such a beam is essential to optimise the accuracy of measurement. Secondly, after the sputtered material has cleared from the analysis line, the analytical beam is

applied to a smaller area, or sub-crater within the sputter crater. This causes the emission of secondary ions as described in the previous section. A sub-crater is utilised to minimise any interference from material at the crater edge ensuring that a sharper interface and compositional information are obtained. After the SIs have been collected in the analyser Figure 2.8 C), the sputtering and analytical steps repeat sequentially until the desired sample depth has been measured.

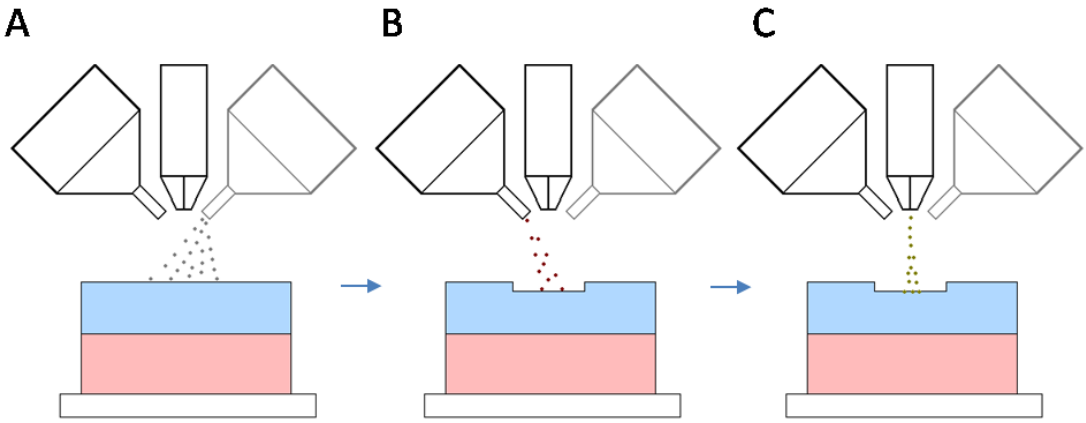


Figure 2.8: Schematic representation of the three main steps used in depth profile-SIMS. **A:** A high energy sputter beam is focused over the sputter area (*e.g.* 250 x 250 µm). **B:** The analytical beam is applied to the analysis area (*e.g.* 50 x 50 µm) which is centred within the sputter area. **C:** The secondary ions generated by the analysis beam are collected and accelerated into the analyser.

Specific peaks are selected from the mass spectra obtained by the scanning analytical beam and the final output is a depth profile as a function of sputter time, as shown in Figure 2.9. The example shown here depicts a trilayer structure comprised of polystyrene/P3HT/PCBM. Three mass fragment anions are plotted, CH, ^{34}S and D. The CH signal is most intense within the polystyrene layer, whereas the ^{34}S is most pronounced within the central P3HT layer and the deuterium signal is most abundant within the D5-PCBM layer. The depth profile can be used to qualitatively determine trends in composition as a function of depth. If appropriate calibration is carried out, in many cases it is possible to use the depth profile to reconstruct a composition-depth plot. For this accurate knowledge of the sputter rates and ion yields are required.

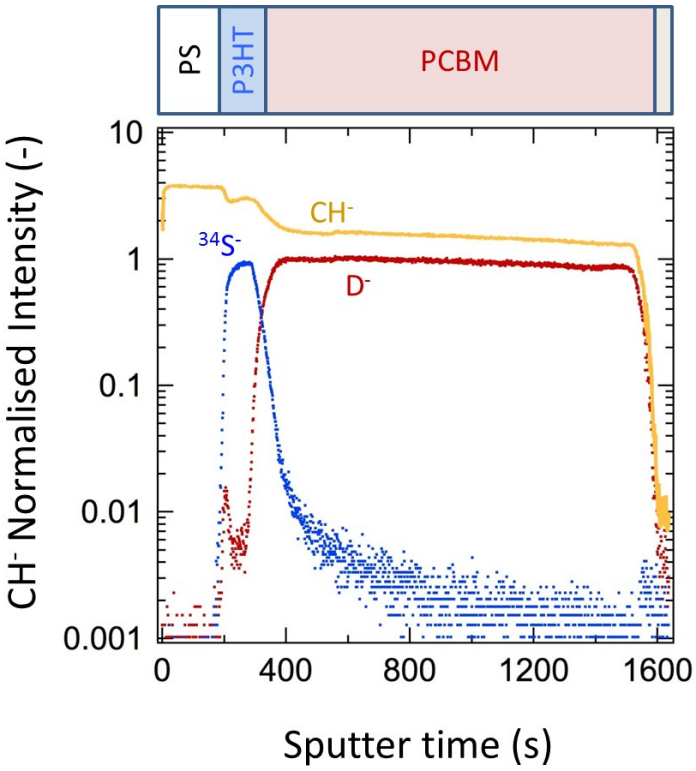


Figure 2.9: Example of a depth profile SIMS measurement of a trilayer structure of polystyrene (PS)/P3HT/PCBM. The depth profile exhibits high CH^- signal in the PS layer but no discernable $^{34}S^-$ or D^- signals. Once the interface with the P3HT layer is uncovered (~200 s) there is a sharp onset in the $^{34}S^-$ signal. At longer sputter times the D5-PCBM layer is uncovered and a strong increase in the signal D^- signal is observed in conjunction with a reduction in CH^- and S^- signals. When the substrate is reached (1600 s) all signals of interest reduce in intensity. It is worthwhile to note that the P3HT/D5-PCBM interface is less sharp than the PS/P3HT, possibly due to beam-induced mixing or a roughening of the sample throughout the measurement.

2.3 References

1. S. Shoaee, M. P. Eng, E. Espildora, J. L. Delgado, B. Campo, N. Martin, D. Vanderzande and J. R. Durrant, *Energy & Environmental Science*, 2010, **3**, 971-976.
2. J. J. Thomson, *Philosophical Magazine*, 1910, **20**, 752-767.
3. J. C. Vickerman and I. S. Gilmore, *Surface Analysis: The Princpal Techniques*, John Wiley & Sons Inc, 2009, ch. 4, pp. 114-115.
4. Z. Postawa, B. Czerwinski, M. Szewczyk, E. J. Smiley, N. Winograd and B. J. Garrison, *The Journal of Physical Chemistry B*, 2004, **108**, 7831-7838.
5. A. D. Appelhans and J. E. Delmore, *Analytical Chemistry*, 1989, **61**, 1087-1093.

6. D. Touboul, F. Kollmer, E. Niehuis, A. Brunelle and O. Laprévote, *Journal of the American Society for Mass Spectrometry*, 2005, **16**, 1608-1618.
7. C. Szakal, S. Sun, a. Wucher and N. Winograd, *Applied Surface Science*, 2004, **231-232**, 183-185.
8. N. Davies, D. E. Weibel, P. Blenkinsopp, N. Lockyer, R. Hill and J. C. Vickerman, *Applied Surface Science*, 2003, **203-204**, 223-227.
9. S. Ninomiya, K. Ichiki, H. Yamada, Y. Nakata, T. Seki, T. Aoki and J. Matsuo, *Rapid Communications in Mass Spectrometry*, 2009, **23**, 3264-3268.
10. J. L. S. Lee, S. Ninomiya, J. Matsuo, I. S. Gilmore, M. P. Seah and a. G. Shard, *Analytical Chemistry*, 2010, **82**, 98-105.
11. T. Ohe, M. Kuribayashi, R. Yasuda, A. Tsuboi, K. Nomoto, K. Satori, M. Itabashi and J. Kasahara, *Applied Physics Letters*, 2008, **93**, 053303-053303.

Chapter 3

The application of SIMS to the Plastic Electronics area

3.1 Introduction

Plastic electronics is a vibrant field of research comprising many different thin-film technologies for applications including: printable circuitry; flexible solar cells; LEDs and sensors. One unifying factor of all such systems is the importance of the microstructure and device architecture on the performance. There is still much to be learned about; especially, about the driving forces leading to the formation of certain microstructures and relevant structure/property/processing inter-relationships. One technique that holds significant promise, but has so far not been fully exploited in the Plastic Electronics area is secondary ion mass spectrometry (SIMS) depth profiling, whereby 3-dimensional mapping of secondary ions can be created, yielding valuable structural-composition information. This technique is capable of mapping laterally over areas of 10-100 µm and vertically through 10-1000 nm, making it ideally suited for probing thin-film samples, as exemplified by the poly(3-hexylthiophene-2,5-diyl) (P3HT)/ poly(3-hexylselenophene-2,5-diyl) (P3HS) bilayer reconstruction shown in Figure 3.1.

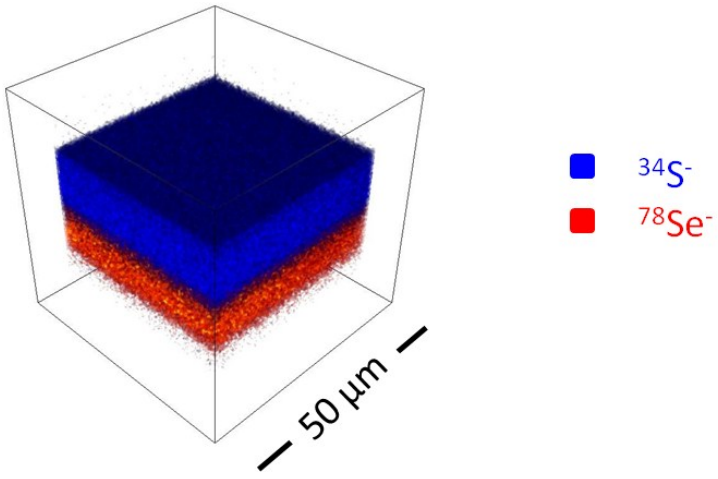


Figure 3.1: Three dimensional reconstruction of a pristine P3HT/P3HS bilayer, clearly showing distinct layers of the two materials. *x* and *y* sides of the cube each represent 50 µm. The *z* side has been expanded and represents 400 nm to highlight the depth sensitivity of the measurement.

SIMS has been used to address different aspects in the Plastic Electronics area. For example, the Krebs group have used time of flight (ToF)-SIMS to investigate chemical degradation mechanisms in organic photovoltaic (OPV) blends utilising isotopically labelled oxygen.[1] In addition to this, Treat *et al.* used dynamic SIMS to investigate the temperature-dependent diffusion of fullerenes into different semiconducting polymers.[2-3] A number of studies carried out by Moons *et al.*[4] investigated the vertical phase separation in different semiconducting polymer:fullerene blends that are used in for OPV applications. Work by Ohe *et al.* probed the vertical phase separation in polymer: small molecule blends used for organic field effect transistors with SIMS depth profiling and were able to correlate the structural attributes to the electronic properties.[5] In addition Yamamoto *et al.* employed a gradient shaving technique to image a bevelled cross-section type structure of a blend.[6] More recent work from Smentkowski *et al.* utilised an Ar cluster ion source which was capable of resolving significantly larger ionic fragments of P3HT and [6,6]-phenyl-C61-butyric acid methyl ester (PCBM) than had previously been recorded,[7] thereby reducing the requirements for elementally discrete materials.

In addition to these interesting reports of SIMS utilisation within the Plastic Electronics area, there are currently a number of research questions where the capabilities of SIMS may have important input. For example, recently the group of Steiner,[8] reported an apparent surface directed spinodal decomposition (SDSD) of blends of P3HT:PCBM cast from chlorobenzene, which was investigated using X-ray photoelectron spectroscopy (XPS). In addition, the report by *Xu et al.*[9] highlighted the role of vertical phase separation in inverted OPV devices as a key factor in determining device performance. Further reports[10, 11] highlight the need to improve the understanding of the processes leading to vertical and lateral phase separation within OPV blends.

Clearly, these open research questions highlight the active interest in many areas that would benefit from investigations with a variety of SIMS techniques. There still remains significant scope to improve our understanding of the SIMS process and the quality of information available from the measurement. Some of the main routes to improve the quality of information are: increasing spatial

resolution; improving larger molecular signals; understanding composition-intensity relationships and understanding vertical profiling — each of which and are briefly discussed below.

- **Increasing spatial resolution**: currently SIMS resolution is typically limited to a lateral resolution of ~50 nm,[12] however practical operation generally deems this limit closer to 200 nm and is ion beam dependent. Depth resolution however is usually significantly better, around 10 nm.[13] While this point is highly important for the development of SIMS the majority of this progression will come from new ion source design, and is therefore outside the scope of this thesis.
- **Improving larger molecular signals**: this is a key to enhancing the measured contrast especially within organic and biological systems, where the majority of contrast is dependent upon covalent bonding as opposed to the elements present. In recent years, significant advances have been made, predominantly through the development of cluster ion sources.[14] This point is therefore again largely dependent upon novel instrumentation.
- **Understanding composition-intensity relationships**: this relates to the complex and highly debated process of secondary ion formation within organic films.[15-17] If it is possible to better understand and empirically model the composition intensity dependence of given systems then it will be possible to relate composition to the observed ion yields.
- **Understanding vertical profiling**: by developing relationships between the composition of thin-films and the sputter rates it should be possible to more reliably interpret the sputter time as a depth.

The final two points outlined above are of significant importance for the Plastic Electronics area, whereby building up a comprehensive picture of composition as a function of depth is of significant interest for a number of reasons, including visualising phase separation during solvent casting and understanding processes of intermixing from bilayer structures, *e.g.*, during a post-

deposition treatment. For these reasons one of the main focuses of this chapter (Section 3.3) is to evolve such understanding for systems directly relevant to organic semiconductors. In order to place the following investigation in context, the next section gives a background and overview of SIMS.

3.2 Understanding binary systems of functional organic materials

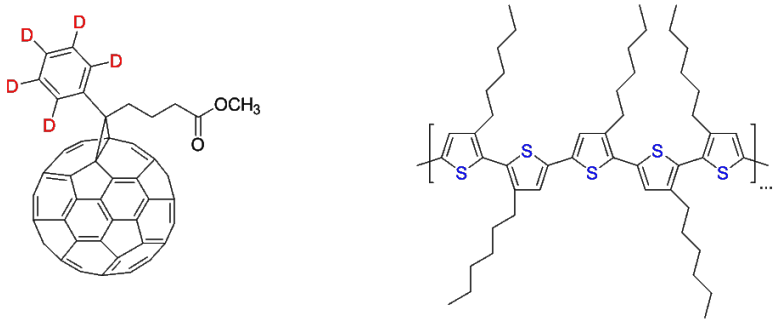
3.2.1 Blends – RRa-P3HT:D5-PCBM

As mentioned in the previous section there are a number of experimental conditions that need to be understood and optimised in order to maximise the information gained from SIMS. Here a model system is utilised to help understanding the differences in vertical phase separation and to gain a better insight of the feasibility of reconstructing the depth profiles into quantitative depth and composition information. We investigate the full composition range of regiorandom-P3HT (RRa-P3HT): [6,6]-pentadeuterophenyl-C61-butyric acid methyl ester (D5-PCBM) blends. The reason for selecting the regio-random analogue of P3HT was to reduce the polymers intrinsic ability to crystallise, as this was anticipated to reduce the number of phases that could be present and hence allow a more straightforward investigation. It is worthwhile to note that P3HT is different from the majority of semiconducting polymers as it has a regioregular and regiorandom form. The molecular structures of the materials used in this section are depicted in Figure 3.2 highlighting the atoms allowing differentiation between the two materials *i.e.* D and S for D5-PCBM and P3HT, respectively, coloured in red and light blue.

3.2.1.1 Vertical separation

To explore the vertical distrbution of materials over the full composition range of the RRa-P3HT:D5-PCBM binaries, thin-film were prepared as explained in Materials and methods. The depth

profiles of these samples are displayed in Figure 3.3, with the weight fraction of P3HT shown as insets. All depth profiles measured here clearly display the expected two layer structure of the PS/P3HT:D5-PCBM, as deduced from the fact that at early measurement times (*i.e*. between 0-100 s, lefthand side of each depth profile) we observe a layer devoid of sulphur (P3HT) and deuterium (D5-PCBM), but rich in CH^- anions.



D5-PCBM RRa-P3HT

Figure 3.2: Molecular structures of the deuterated fullerene, D5-PCBM (left) and regiorandom P3HT (right). These were used for the binary blend depth profile study. The coloured atoms indicate the atoms probed in D-SIMS; deuterium (red) and sulphur (blue) for D5-PCBM and RRa-P3HT, respectively.

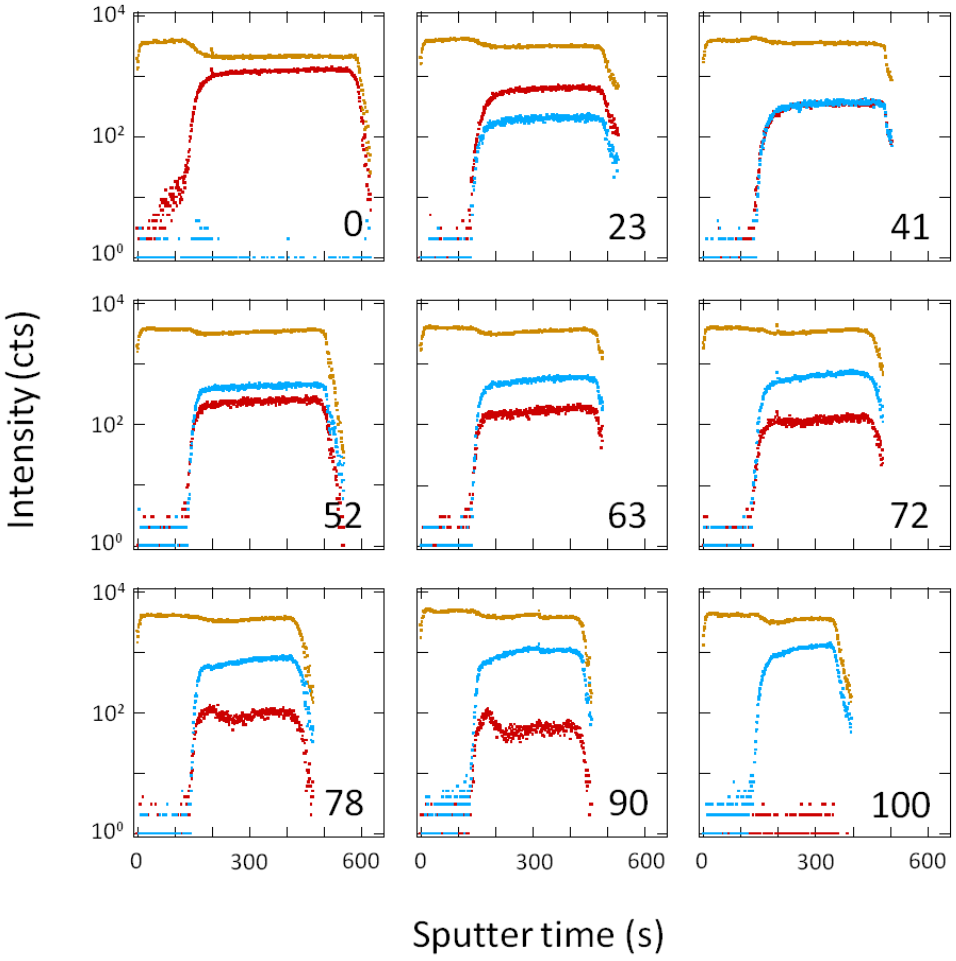


Figure 3.3: SIMS depth profiles of various RRa-P3HT:D5-PCBM blends. Shown are the $^{34}S^-$ (blue), D^- (red) and CH^- (yellow) traces. The insets indicate the P3HT weight content (%) in the respective blend.

Referring to Figure 3.3, after sputtering through the polystyrene (PS) layer (explained in the materials and methods section), all samples exhibit clear onsets for both the sulphur and deuterium signals. The layer comprised of P3HT:D5-PCBM takes between 200 - 450 seconds to sputter through. This difference in sputter time is related to the layer thickness and also sputter rate of the blend, and is discussed in more detail below. For samples comprising between 0 - 63 wt% P3HT, the blend layer generally appears to have flat signals of S^- and D^-, implying no significant vertical phase separation is present. Interestingly, at higher polymer content, slight differences occur in the shape of the ion yields. This is observed as an increase in the gradient of the profile tops, which is attributed to charging at the sample surface leading to enhanced ionisation.[18] However as there is an anti-

correlation between the S^- and D^- signals, which may relate to small differences in the vertical composition close to the top interface of the blend film, due to an accumulation of D5-PCBM at the surface of the film. Such an accumulation may be due to: beam induced thermalisation of the blend during the measurement or aggregation and/or conformational relaxation of the polymer expelling the fullerene to the free surface. It is worth highlighting that while there may be a slight amount of vertical demixing in the RRa-P3HT:D5-PCBM blends occuring, the difference in vertical distribution of the D5-PCBM signal is relatively small.

Importantly, it is evident from the depth profiles that the neat samples (*i.e.* D5-PCBM: 0 wt%; RRa-P3HT 100 wt%) show essentially no signal interference from the other traces; *e.g*. the deuterium ion signal in the neat P3HT samples is $<10^3$ smaller than that in the neat D5-PCBM sample and *vice versa*. This implies that the traces followed here will provide excellent references for understanding the composition of such binary systems.

To summarise this part: it is clear that stable signals from the different ions corresponding to D5-PCBM and RRa-P3HT can be obtained with very little interference. This allows us to analyse, for instance, the vertical composition across thin-films of an entire polymer:fullerene composition range. It is found that for the majority of the blend ratios there is no vertical phase separation. Vertical phase separation seems to occur at low fullerene content, as evident from the small enhancement of the D^- signal found at the top interface of the blend film. This could be a result of processing or measurement induced. Furthermore, the generally flat nature of the ion signals from D^- and S^- in the blend layer profiles and the sharp onset and offset of these layers allows for more comprehensive analysis of the blends to be carried out. This is detailed in the following sections.

3.2.1.2 Ion yield

In order to build up a more comprehensive understanding of how the measured intensity relates to the precise composition of the investigated blends, it is necessary to investigate the composition-intensity relationship. The depth profiles discussed in the previous section provide intensity information of the full composition range of the RRa-P3HT:D5-PCBM binary for both components, which are plotted for the anionic (D^-, $^{34}S^-$ and C_4S^-) species against composition in Figure 3.4.

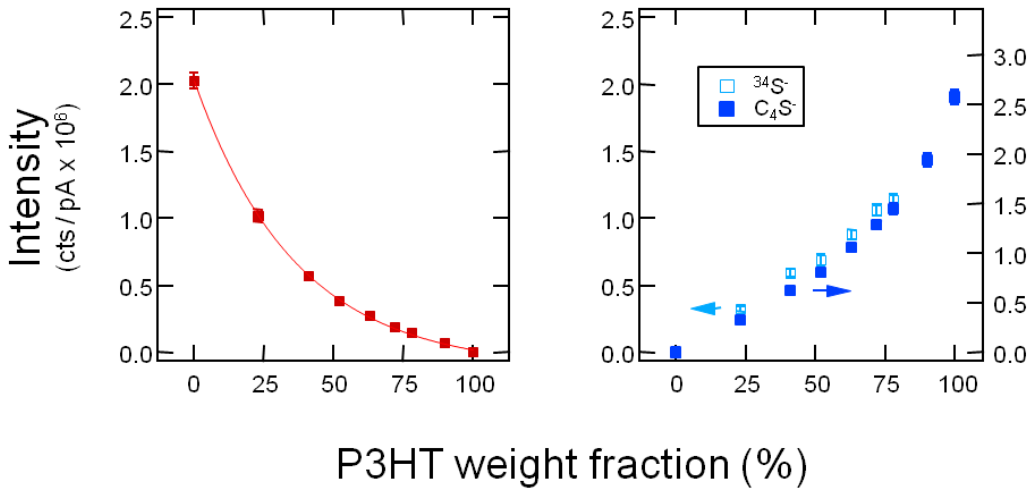


Figure 3.4: Secondary ion yield plotted against composition of RRa-P3HT:D5-PCBM blends. **Left**: D^- negative ions. **Right**: $^{34}S^-$ (open) and C_4S^- (solid) negative ions. The SIMS intensity shows a non-linear behaviour with composition. It is possible to accurately fit the D^- intensity-composition relationship using a single exponential function (red line). Displayed error bars are based on a standard deviation of the intensity variation in the plateau region.

The composition-intensity dependence for the measured ions all display monotonic behaviour, its super-linear evolution with composition being likely due to differences in the materials ionisation behaviour when the surrounding environment (matrix) is altered. Beneficially the D^- relationship with composition can be fitted using the exponential function displayed in Equation 3.1:

$$I(w) = I_0 + Ae^{-kw} \qquad \text{Equation 3.1}$$

where I_0, A and k are empirically determined parameters. The fit of this equation is shown as the red line in Figure 3.4 (left) and can be used for the conversion of the intensity (*y*-axis) of a depth profile into weight composition and, hence, can be employed for determining the composition in regions of interest for polymer:fullerene systems. It also provides understanding how the ion beams interact with the sample and establishes a platform for experimentally relevant investigations such as: studying vertical profiles; bilayer interdiffusion and the microstructural development, *e.g.* during interdiffusion.

3.2.1.3 Sputter rate

Having addressed the composition-intensity relationship (which essentially reflects the *y*-axis of a depth profile) we now turn our attention to understanding the sputter rate, which relates the sputter time to the actual depth measured through the sample. Careful analysis of how this varies with composition will allow reconstruction of the sputter time into an accurate depth measurement. The depth profile calibration will enable greater insight into: the position and sharpness of interfaces; material distributions within vertically blended structures and a clearer understanding of the effects related to intermixing and layer expansion of films (*e.g*. polymer swelling). The RRa-P3HT:D5-PCBM system provides an excellent model system to study this as there is little vertical composition difference in the prepared samples, meaning the sputter rate throughout the layer should remain constant assuming the sputter energy and sample roughness do not fluctuate significantly. Sputter rates are calculated from the film thickness measured via profilometry (see materials and methods) and the time taken to sputter through the layer. The measured data and calculated rates are displayed in Table 3.1 and Figure 3.5.

Table 3.1: A table of values obtained for films thickness and sputter time used to calculate the sputter rates of the different blend compositions of RRa-P3HT:D5-PCBM

P3HT weight percent	0	23	41	52	63	72	78	90	100
Thickness (nm)	43	50	52	84	71	85	83	98	101
Time (s)	446	355	341	370	333	321	301	298	219
Sputter rate (nm/s)	0.10	0.14	0.15	0.23	0.21	0.26	0.28	0.33	0.46

From the sputter rates plotted in Figure 3.5, it is clear that there is a large variation across the composition range, resulting in a non-linear, but monotonic increase with polymer loading. One reason for this is the significant variation in sputter rate of the two neat materials, whereby RRa-P3HT sputters at over four times the D5-PCBM. The origin of the difference in sputter rates of the neat materials may be affected by: the chemical structure of the components,[19] different beam induced effects[20] or variation in density of the materials. The densities of the RRa-P3HT and PCBM have been reported to be 1.10 and 1.61 g/mol,[2] respectively, and this difference will certainly be a contributing factor to the slower sputtering of D5-PCBM. However, the density of PCBM is only ~45% higher than that of RRa-P3HT, hence, would not explain in full the observed discrepancy in sputter rate.

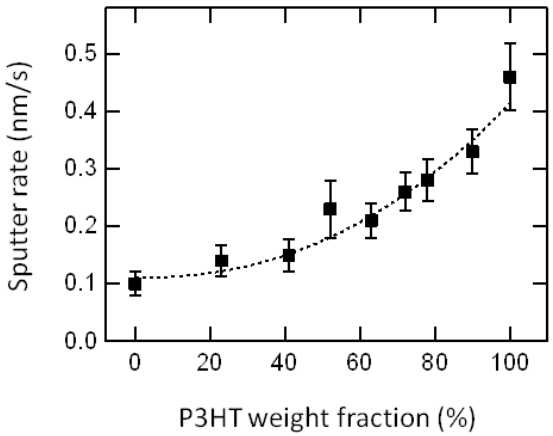


Figure 3.5: Sputter rate plotted against composition of RRa-P3HT:D5-PCBM blends. The graph shows a clear super-linear rate dependence on composition. The error bars are plotted from cumulative uncertainty in thickness and sputter time. The dashed line is an exponential fit as a guide for the eye.

In summary, the previous two sections have derived relationships for intensity/composition and sputter-rate/composition, having found both to be monotonic and non-linear. The intensity plot can be used to determine the composition of a given layer comprised of the materials investigated. In conjunction with this, once the composition is known, the sputter rate can be determined, allowing for the sputter time to be converted into depth. This provides a tool for further interpretation of other structures of interest (see Section 3.3.3) and lays the platform towards developing a model capable of converting a depth profile into a realistic reconstruction of the active layer of multi-component semiconducting thin-films.

3.2.2 Influence of material selection

To understand whether the trends observed in the RRa-P3HT:D5-PCBM blends (both with respect to their vertical distribution and composition dependencies) are general for all polymer:fullerene systems, binaries comprised of different polymers and fullerenes were investigated. The following two sections provide examples of systematic variation of the fullerene and polymer, with a focus on novel materials that have been shown to have more promising OPV device performance than RRa-P3HT:D5-PCBM.[21-23]

3.2.2.1 Fullerene derivatives and multi-adducts

The chemical structure of fullerenes can have a significant effect on the structural and optoelectronic properties of polymer:fullerene blends (see Chapter 5). Variation of the fullerene can lead to an enhanced device performance through a number of routes including an increase in V_{oc}, or the improvement of the extraction of photo-generated charges. Here we selected commercially

viable fullerenes, *i.e*. D5-bis-PCBM and D-ICBA (structures shown in Figure 3.6) in addition to the previously discussed D5-PCBM.

The depth profiles of RRa-P3HT:D5-bis-PCBM and RRa-P3HT:D-ICBA blends appeared similarly flat to those of RRa-P3HT:D5-PCBM (data not shown), indicating that also for these blends no discernable vertical phase separation occurs. The intensity/composition dependence from the plateau regions of the depth profiles was extracted as outlined above for the RRa-P3HT:D5-PCBM binaries and the ionisation behaviour of the different fullerenes is compared with the former system, shown in Figure 3.6.

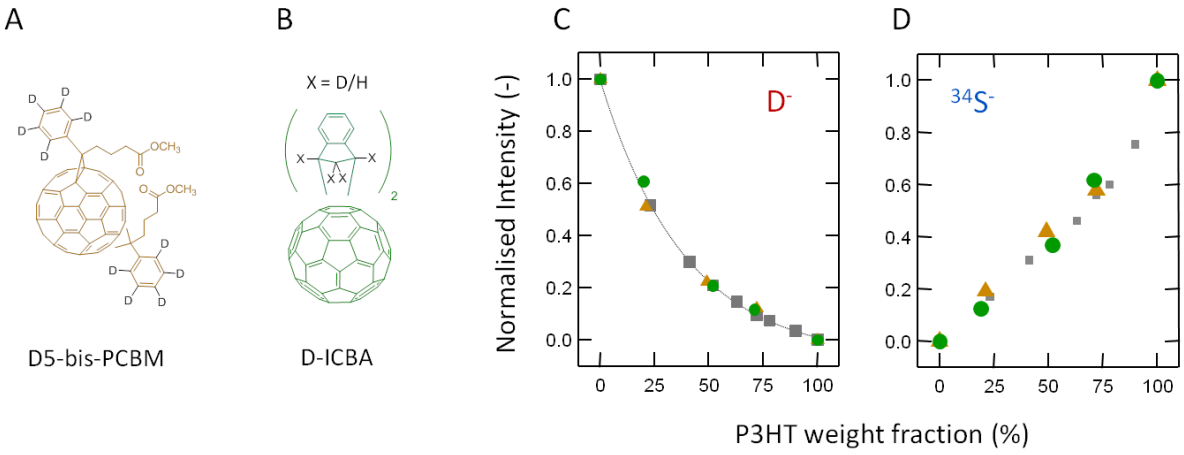


Figure 3.6: Molecular structures of the selected deuterated fullerenes (*i.e.* D5-bis-PCBM and D-ICBA) and composition-intensity plots of RRa-P3HT blend systems comprising these fullerenes: D5-PCBM (grey squares), D5-bis-PCBM (orange triangle) and D-ICBA (green circles). **A-B:** Molecular structures of D5-bis-PCBM and D-ICBA, respectively. **C:** Normalised composition-intensity plot for deuterium (D^-). The grey line represents the fit derived for D5-PCBM, which appears in good agreement with measurements from the other fullerenes. **D:** Normalised composition-intensity plot for sulphur ($^{34}S^-$).

The intensity/composition relationships of the blends comprising different fullerene systems (Figure 3.6 C-D) exhibit generally similar monotonic behaviour with the normalised deuterium ion (D^-) signal being essentially identical for all three fullerenes investigated. This is significant as it means that the exponential fit derived in the previous section to model RRa-P3HT:D5-PCBM can also be applied to all of the fullerenes investigated here. Interestingly the signal derived from the polymer

($^{34}S^-$) shows a larger deviation from the reference RRa-P3HT:D5-PCBM system (shown in grey), but overall the sulphur data suggests ion yields that are more linear with composition than observed in the D^- case. This may be due to the fact that the chemistry leading to liberation of sulphur ions can depend upon the chemical nature of the surrounding molecules (matrix), which will change if a different fullerene is present.

In summary, varying the chemical structure of the fullerene blended with RRa-P3HT showed essentially no changes in the vertical phase separation behaviour, in all cases yielding a homogenous vertical distribution of the two components. This vertical homogeneity allowed for intensity/composition relationships to be derived for the different systems and showed similar behaviour for all three systems. In the case of the D^- signal, all systems could be fit using the same equation derived for RRa-P3HT:D5-PCBM. Furthermore this relationship can now be used to determine composition in systems, such as interdiffused bilayers, and is utilised extensively in Chapter 5.

3.2.2.2 High performance OPV blends — DPP-TT-T:D5-PCBM

Having observed no significant differences in the vertical composition of the prototypical polymer (RRa-P3HT) blended with different fullerenes, focus is now turned to varying the polymer. Here a diketopyrrolopyrrole (DPP) derivative (DPP-TT-T, structure shown in Figure 3.7 A) was selected, as it is part of the novel class of “push-pull” polymers, which have shown much promise in terms of OPV device performance when blended with PCBM.[23]

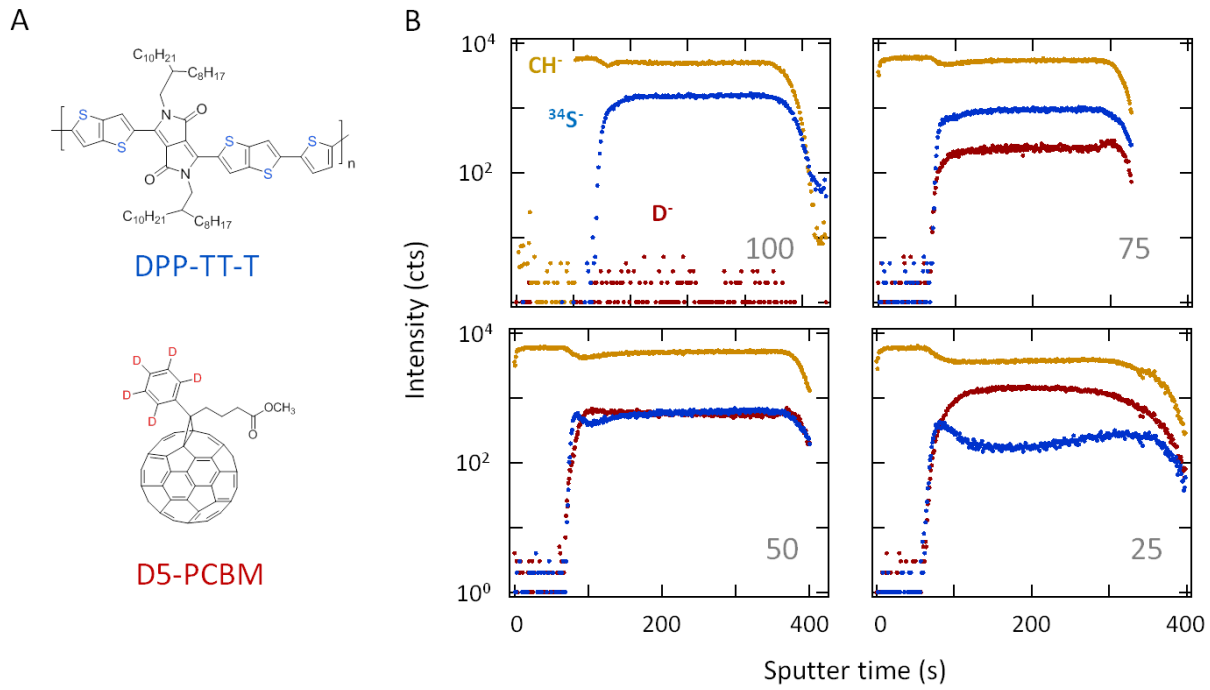


Figure 3.7: Molecular structures and vertical distributions of solution-cast, pristine DPP-TT-T:D5-PCBM blends**. A:** Molecular structures of DPP-TT-T (sulphur containing- blue) and D5-PCBM (deuterium containing – red). **B:** Depth profiles for pristine blends of DPP-TT-T:D5-PCBM of different composition (DPP-TT-T weight fractions is shown in inset).

Solution processed DPP-TT-T:D5-PCBM blends spanning the entire composition range were investigated. Their depth profiles are displayed in Figure 3.7 B on a logarithmic scale to aid visualisation of the background and maximise signals. Various observations can immediately be made. Firstly it is important to note that there is essentially no contribution from the DPP-TT-T to the D^- signal (as deduced from the neat DPP-TT-T profile), confirming that this signal can be used to attain information on D5-PCBM. Secondly, the depth profiles show striking differences when compared to the RRa-P3HT:D5-PCBM system, with a significant vertical phase separation occurring in the DPP-TT-T:D5-PCBM. This is enhanced when the fullerene content is increased; although even for weight ratios of 75:25 DPP-TT-T:D5-PCBM, there appears to be some segregation of the fullerene to the bottom interface occurring, as deduced from the enhancement in the D^- signal and a reduction in the intensity of $^{34}S^-$. To better aid visualisation of the phase separation, normalised, linear plots and an estimation of the vertical weight composition are displayed in

Figure 3.8 (A and B, respectively). The vertical phase diagram was thereby constructed from the above SIMS data as detailed in materials and methods.

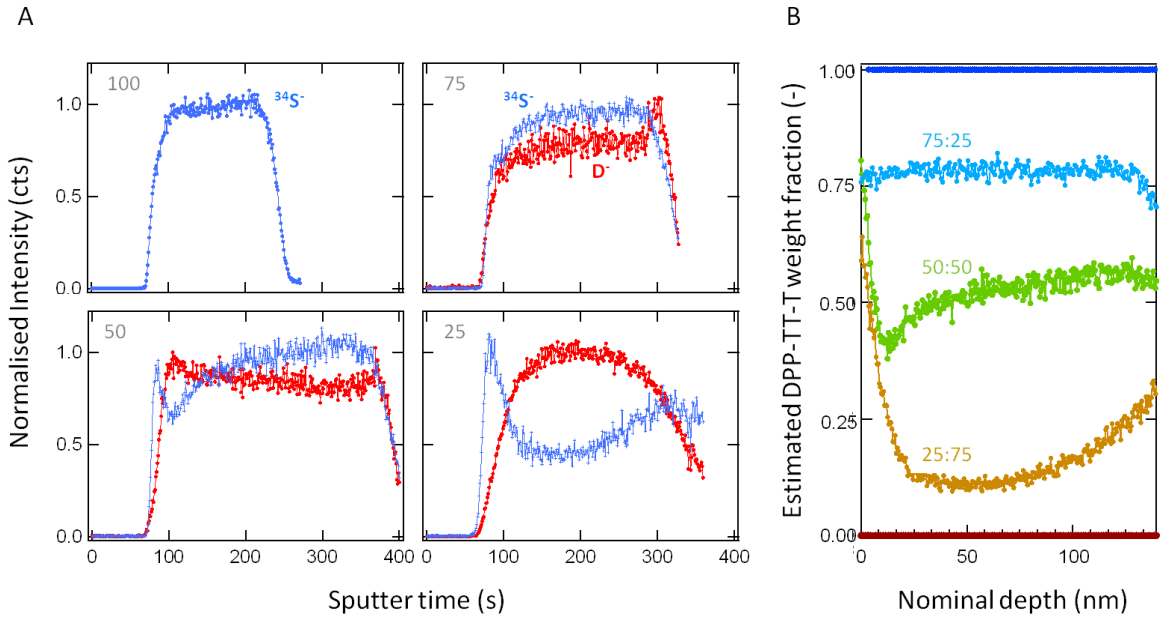


Figure 3.8: Normalised vertical distribution of solution-cast DPP-TT-T:D5-PCBM blends and estimated binary composition-depth diagram. **A:** Depth profiles of blends showing DPP-TT-T ($^{34}S^-$, blue traces) and D5-PCBM (D^-, red traces), normalised and plotted on a linear scale to aid clarity. **B:** Estimated depth-composition diagram for of different DPP-TT-T weight fractions, showing the different vertical distribution of materials, with the most pronounced changes at the top interface. Insets indicate the DPP-TT-T content by weight. Diagram constructed as described in Section 3.5.

When the fullerene content is increased to 50 wt%, the system starts to exhibit more significant vertical phase separation. In this case, there is an apparent enhancement of the polymer signal observed at the top interface, followed by a more fullerene-rich layer, another polymer-rich layer and, finally, an accumulation of fullerene at the bottom interface. When the fullerene content is increased, larger amplitude oscillations (based on $[(I_{peak}-I_{trough})/I_{peak}]$) between the signals are observed. Interestingly in the case of the 25:75 (by weight) polymer:fullerene sample, the relative period of oscillation appears larger, suggesting larger-scale phase separation within this system. The origin of this demixing behaviour may be due to an interface effect, such as surface directed spinodal decomposition (SDSD)[24] or a lateral demixing resulting in droplets capped with a “skin” of lower

surface energy fraction, *e.g*. the polymer-rich phase.[25] It is likely that such demixing phenomena behaviour may be expected for less miscible blends, and may result from the more rigid nature of the DPP-TT-T backbone when compared to RRa-P3HT.

To conclude this part of this chapter, through investigation of systems comprised of different polymers and fullerenes it has been shown that it is possible to observe a range of differing behaviour for these materials systems. In terms of the microstructure and processes governing its formation, it is apparent that under typical solution processing the amorphous polymer RRa-P3HT exhibits virtually no discernable vertical phase separation when blended with any of the three fullerenes investigated. However when a more rigid semicrystalline polymer DPP-TT-T is blended with D5-PCBM, a clearly observable vertical phase separation is found. The magnitude of this phase separation increases with fullerene content. Contributing factors to this development include the interaction parameters of the polymer with both the fullerene and the solvent, which will influence the driving forces for phase separation, both of which would likely show lower miscibility than RRa-P3HT due to the more rigid nature of the DPP-TT-T. Moreover kinetic processes such as material diffusion may play an important role in determining how far towards an equilibrium state a system can progress during the solution casting process. In addition kinetically quenched solid solutions may form, as will be discussed in Chapter 5.

From the perspective of using SIMS to probe plastic electronic materials, it is evident from the above that a clear basis can be established from which relationships between measured intensity and sputter time can be related to absolute composition and depth through a thin-film. For the systems investigated, both relationships are non-linear, but in the case of RRa-P3HT blended with fullerenes, a single empirical exponential model can be used to accurately convert measured intensity into weight composition. These findings can be used in further experiments, including interdiffusion from bilayers, to extract accurate temperature-composition information for material pairs. Our study, hence, can be expected to have impact in the areas of microstructural visualisation

and will further assist in improving our understanding of how SIMS can be successfully used as a tool to probe organic semiconductors.

3.2.3 Bilayers

Within the field of Plastic Electronics, bilayers structures (comprised of discrete layers of two materials sequentially layered onto a substrate) provide useful model systems to investigate a range of structural and electronic properties.[4, 26-28] Pristine bilayers and their thermally annealed counterparts can thereby provide valuable comparison capable of yielding complementary information to solution-cast blends, in some cases due to their significant differences in microstructure. These systems are discussed in detail in Chapters 4-7, and used to investigate the photo-physical properties including: energy transfer, exciton quenching and charge generation. The experimental method utilised to fabricate bilayers is detailed in Section 2.2.7.

3.2.3.1 Influence of donor polymer regioregularity on the intermixing with D5-PCBM

In order to assess the applicability of the bilayer fabrication process and study a prototypical OPV system, the intermixing of fullerenes with RRa-P3HT was investigated. The depth profiles of bilayers of RRa-P3HT/D5-PCBM are shown in Figure 3.9 A. The bilayer kept at room temperature (Figure 3.9, left panel) clearly shows a two layer structure, which interestingly exhibits a significant fullerene signal within the polymer layer, corresponding to ~16 wt%. This observed intermixing of the fullerene is an indicator of the mobility and miscibility of the D5-PCBM in RRa-P3HT, even at room temperature. It is also interesting to note that we observe a small signal enhancement of the

fullerene at the air interface, similar to our previous observation of an enhanced D^- signal at the air interface of solution-cast blends (Figure 3.3).

After annealing (30 s and 100 °C) the bilayer shows complete vertical intermixing across the sample, yielding a layer of a composition of ~65 wt% D5-PCBM. The fact that complete intermixing occurs suggests that the actual miscibility at the annealing temperature is higher than the measured content, and as a consequence, the reservoir of neat fullerene has been emptied.

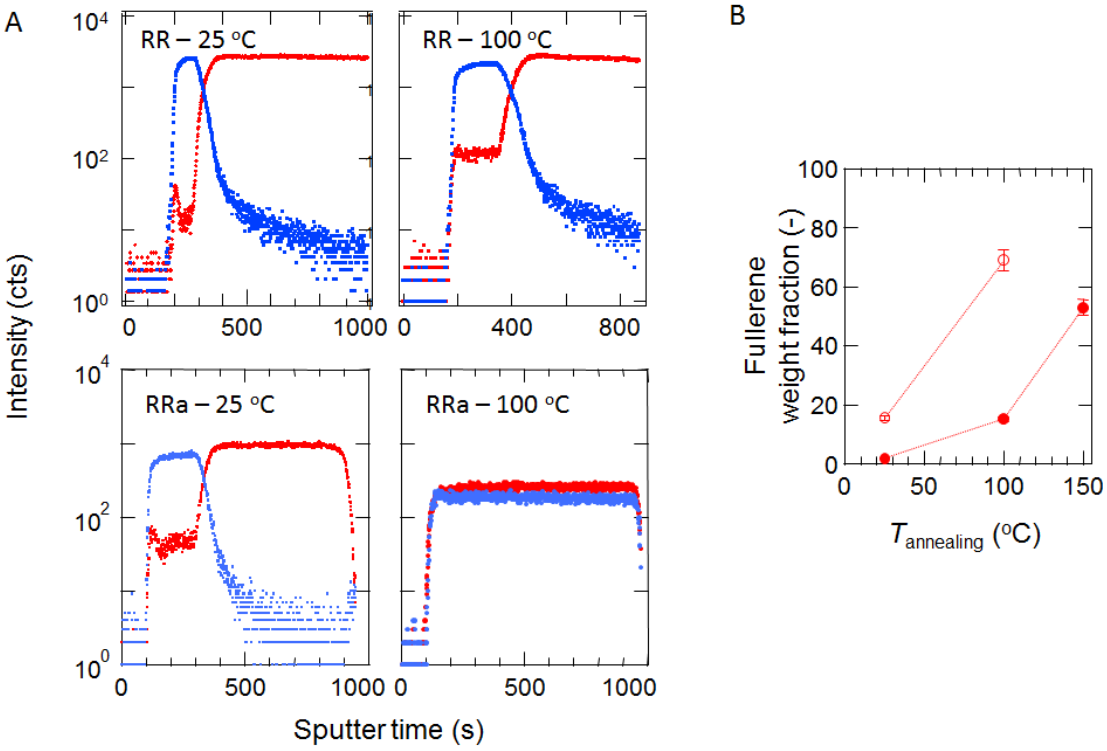


Figure 3.9: Temperature-dependent intermixing of RR-P3HT/D5-PCBM and RRa-P3HT/D5-PCBM bilayers. **A:** Depth profiles of RR-P3HT/D5-PCBM (top) and bilayers RRa-P3HT/D5-PCBM (bottom) pristine (left) and annealed at 100 °C, 30 s (right), displaying complete intermixing after the heat treatment. **B:** Quantity of D5-PCBM intermixed into RRa-P3HT (open circles) and RR-P3HT (filled circles) as a function of bilayer annealing temperature (lines are as a guide for the eye).

To compare the effect of crystallinity of the polymer on the fraction of intermixed fullerene, similar experiments were carried out using regioregular (RR)-P3HT. In contrast to the RRa-P3HT containing sample, a distinct bilayer structure with polymer-rich and fullerene-rich layer is retained for

all RR-P3HT/D5-PCBM samples independent of annealing temperature. The fullerene content in the P3HT layer varies (see Figure 3.9 B), with more D5-PCBM interdiffusing at higher temperatures. Clearly, the more crystalline RR-P3HT exhibits lower intermixing with the fullerene, when compared to RRa-P3HT, which is molecularly less ordered. This lower tendency for intermixing has been previously reported based on work applying different techniques,[29] with the specific origin believed to relate to the volume fraction of non-aggregated polymer capable of incorporating fullerene.[2, 30] Thereby, the effect of inter-crystalline tie-chains limiting the expansion of the polymer matrix will play a large role.

3.2.3.2 Fullerene intermixing with different semicrystalline polymer semiconductors

Having observed stark differences in the effect of crystallinity on the intermixing of D5-PCBM with RRa-P3HT and RR-P3HT, we present below a comparison with another polymeric semiconductor that shows a tendency to molecularly order: DPP-TT-T. This polymer leads to high efficiency OPVs and has a relatively stiff backbone due to it multiple fused rings.[31]

The intermixing behaviour of DPP-TT-T/D5-PCBM bilayers after thermal treatment at different temperatures is displayed in Figure 3.10. We find a clear enhancement in the deuterium ion signal originating from the PCBM in the polymer layer as the temperature is increased. Nonetheless, the interface between the two layers appears to remain of approximately constant width in all cases, suggesting a well-defined bilayer is maintained with annealing leading to a polymer-rich and a fullerene-rich layer. Moreover, independent of the thermal treatment selected, we find a flat profile of the D^- signal within the polymer layer, suggesting diffusion equilibrium was attained.

The relative D^- signal is plotted against temperature for the DPP-TT-T/D5-PCBM (Figure 3.10 left – blue diamonds) and shows very low fullerene intermixing using temperatures of 100 ^oC and

below. Upon increasing the annealing temperature to 125 °C, there is a noticeable increase in the uptake, possibly due to a glass transition of the system facilitating conformational reorganisation and molecular motion. However, even at annealing temperatures of 250 °C, the intermixed signal of fullerene remains low for the DPP-TT-T:D-5PCBM blends (*e.g.* less than 10 %), when compared to RR-P3HT comprising systems (red circles), which display a much greater signal from intermixed fullerene across all temperature ranges investigated with a large rapid increase in intermixing at around 150 °C. From this it is clear that the DPP-TT-T:D5-PCBM exhibits remarkably different behaviour.

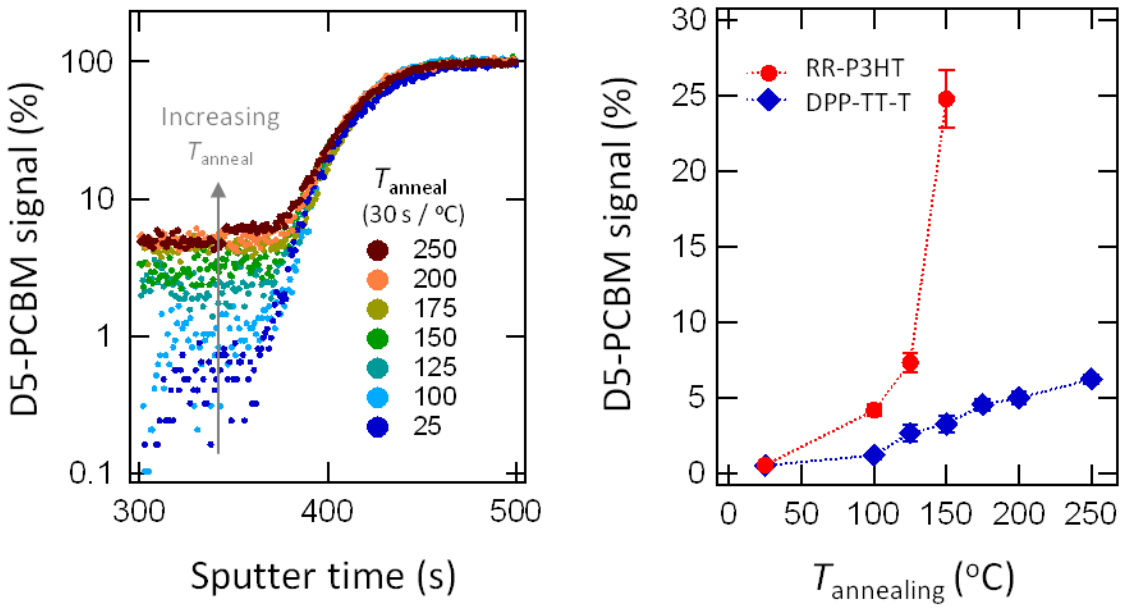


Figure 3.10: Temperature-dependent intermixing of D5-PCBM into DPP-TT-T. **Left:** D^- signal of normalised depth profiles of DPP-TT-T/D5-PCBM annealed at different temperatures for 30 s**. Right:** Mixing behaviour of DPP-TT-T/D5-PCBM (blue) and RR-P3HT/D5-PCBM as a function of annealing temperature.

The relatively low intermixing observed for D5-PCBM with DPP-TT-T may be related to a number of factors, including: a more positive chemical interaction potential between the polymer-fullerene ($\chi_{P\text{-}F}$); a reduced non-crystalline fraction of the polymer; a higher polymer glass transition; a larger energetic barrier to conformational reorganisation, *etc.* While these factors will contribute to different extent, one underlying attribute of the polymer that — without doubt — will affect a

significant number of the above points is the rigidity of the polymer backbone, a common feature of many of the more-recent high performance polymers.[23, 32, 33]

These findings clearly highlight the stark contrast in behaviour between RRa-P3HT, RR-P3HT and DPP-TT-T, in terms of their tendency to mix with PCBM. Furthermore, the data presented above suggest that in DPP-TT-T, there are relatively constrained pathways through which the fullerene can diffuse. These results, combined with the vertical demixing observed in blends of DPP-TT-T:D5-PCBM blends, give thus more insights into the processes affecting microstructural formation and point towards a lower thermodynamic tendency for DPP-TT-T:D5-PCBM to mix when compared to RR-P3HT:PCBM. Kinetic trapping of the structure during solution casting may, however, also play a critical role in the microstructure development from solution. A more detailed investigation of such phenomena is discussed in Chapter 5.

3.3 Conclusions

The results discussed within this chapter have allowed a number of conclusions to be drawn falling broadly into two categories: (i) those related to the structural formation processes and interactions affecting the microstructure in systems, encompassing a variety of polymers and fullerenes, and (ii) the optimisation and understanding of the application of SIMS to systems relevant in the Plastic Electronics area.

Firstly, a number of findings related to the microstructural formation processes within different polymer-fullerenes systems have been discussed. The vertical phase separation of solution cast blends was investigated; systems of RRa-P3HT blended with D5-PCBM, D5-bis-PCBM or D-ICBA exhibited essentially no vertical phase separation, whereas blends of the more rigid polymer DPP-TT-T:D5-PCBM strongly phase-separated vertically, especially at higher fullerene content, likely due to lateral demixing or surface directed spinodal decomposition (SDSD). It seems therefore obvious that

in polymer:fullerene blends replacement of the polymer has a larger influence on vertical phase separation than when changing the fullerene. Intermixing from bilayer structures furthermore highlights this difference between the behaviour of blends comprising different polymers, and shows that their behaviour is affected by both the degree of crystallinity and the molecular structure of the polymer. Thereby we find that DPP-TT-T incorporates the lowest amount of fullerene, which we attribute to the more rigid nature of its backbone.

Secondly, In terms of SIMS, both composition-intensity and composition-depth relationships have been empirically derived. These relationships allowed for the quantification of further systems of interest, including intermixed bilayers, which are important for understanding the temperature-dependent phase behaviour. Furthermore the present chapter provides a quantified basis from which models can be derived to automatically compute the composition as a function of depth directly from the depth profiles obtained from SIMS.

3.4 Materials and methods

Preparation of blends for SIMS measurements: accurate stoichiometries of the respective semiconductor were measured by mass, dissolved in chlorobenzene at 20 mg/ml and cast via spin-coating at 1200 rpm for 45 s. The resultant films were dried under vacuum for 48 hours and then capped with a thin (45 nm) layer of polystyrene (PS). The PS layer was spin-coated onto a silicon substrate at 8 mg/ml from a toluene solution at 2000 rpm for 45 s. The polystyrene layer was then floated and laminated in a similar fashion to the bilayer production (described below). The polystyrene layer within these samples serves two purposes, firstly it enables the analytical and sputter beams to stablise prior to probing the actual sample. Secondly the intensity of the molecular fragment signals (*e.g.* CH^-) observed in the capping layer can be used to calibrate between different measurements.

*Preparation of bilayers for SIMS measurements: b*ilayers were fabricated by spin-coating the deuterated fullerene from a 30 mg/ml solution in chlorobenzene at 800 rpm for 60 s onto an SiO_2 substrate. The polymer was then spin-coated from a 20 mg/ml solution in chlorobenzene at 1200 rpm for 60 s onto a polystyrene sulphonate (PSS) coated glass substrate. The two bilayer component layers were left under vacuum for 48 hours to aid removal of residual solvent. The P3HT layer was then floated onto a bath of deionised water and "scooped up" with the fullerene coated substrate.

Film thickness measurements: A Dektak III profilometer with a needle radius of 250 µm and stylus force of 0.1 mN was used. A standard thickness error of 8 nm was assumed.

Construction of vertical phase diagram from SIMS data: in order to estimate the composition of the DPP-TT-T:D5-PCBM blend layer of as a function of depth equation 3.2 was utilised to derive the estimated DPP-TT-T weight fraction ($W_{DPP\text{-}T\text{-}T}$) as a function of depth, where I_{34S} and I_D are the measured intensities at a given depth for of the $^{34}S^-$ and D^-, respectively.

$$\boldsymbol{Estimated\ DPP\text{-}TT\text{-}T\ weight\ fraction} = \frac{I_{34S}}{I_{34S} + I_D} \qquad \textit{Equation 3.2}$$

3.5 References

1. K. Norrman and F. C. Krebs, *Solar Energy Materials and Solar Cells*, 2006, **90**, 213-227.
2. N. D. Treat, M. A. Brady, G. Smith, M. F. Toney, E. J. Kramer, C. J. Hawker and M. L. Chabinyc, *Advanced Energy Materials*, 2011, **1**, 82-89.
3. a) N. D. Treat, T. E. Mates, C. J. Hawker, E. J. Kramer and M. L. Chabinyc, *Macromolecules*, 2013, **46**, 1002-1007. b) N. D. Treat, A. Varotto, C. J. Takacs, N. Batara, M. Al-Hashimi, M. J. Heeney, A. J. Heeger, F. Wudl, C. J. Hawker and M. L. Chabinyc, *Journal of the American Chemical Society*, 2012, **134**, 15869-15879.
4. a) C. M. Björström, A. Bernasik, J. Rysz, A. Budkowski, S. Nilsson, M. Svensson, M. R. Andersson, K. O. Magnusson and E. Moons, *Journal of Physics of Condensed Matter*, 2005,

17, L529–L534. b) C. M. Björström, S. Nilsson, A. Bernasik, A. Budkowski, M. R. Andersson, K. O. Magnusson and E. Moons, *Applied Surface Science*, 2007, **253,** 3906–3912. c) C. M. Björström, J. Rysz, A. Bernasik, A. Budkowski, F. Zhang, O. Inganäs, M. R. Andersson, K. O. Magnusson J. J. Benson-Smith, J. Nelson and E. Moons, 2009, *Advanced Materials*. **21**, 4398–4403. d) J. J. Michels and Ellen Moons, *Macromolecules*, **2013**, *46* 8693–8701.

5. L. Yu, X. Li, J. Smith, S. Tierney, R. Sweeney, B. K. C. Kjellander, G. H. Gelinck, T. D. Anthopoulos and N. Stingelin, *Journal of Materials Chemistry*, 2012, **22**, 9458-9461.
6. S. Yamamoto, D. Kitazawa, J. Tsukamoto, T. Shibamori, H. Seki and Y. Nakagawa, *Thin Solid Films*, 2010, **518**, 2115-2118.
7. V. S. Smentkowski, G. Zorn, A. Misner, G. Parthasarathy, A. Couture, E. Tallarek and B. Hagenhoff, *Journal of Vacuum Science & Technology A: Vacuum, Surfaces, and Films*, 2013, **31**, 030601-030601.
8. Y. Vaynzof, D. Kabra, L. Zhao, L. L. Chua, U. Steiner and R. H. Friend, *ACS Nano*, 2011, **5**, 329-336.
9. Z. Xu, L.-M. Chen, G. Yang, C.-H. Huang, J. Hou, Y. Wu, G. Li, C.-S. Hsu and Y. Yang, *Advanced Functional Materials*, 2009, **19**, 1227-1234.
10. M. Campoy-Quiles, T. Ferenczi, T. Agostinelli, P. G. Etchegoin, Y. Kim, T. D. Anthopoulos, P. N. Stavrinou, D. D. C. Bradley and J. Nelson, *Nature Materials*, 2008, **7**, 158-158.
11. J. S. Kim, P. K. H. Ho, C. E. Murphy, R. H. Friend, *Macromolecules*, 2004, **37**, 2861-2861.
12. J. C. Vickerman and I. S. Gilmore, *Surface Analysis: The Principal Techniques*, John Wiley & Sons Inc, 2009, ch. 4, pp. 166-166.
13. D. S. McPhail and M. Dowsett, *Surface Analysis: The Principal Techniques*, John Wiley & Sons Inc, 2009, ch. 5, pp. 213-215.
14. N. Winograd, *Analytical Chemistry*, 2005, **77**, 143-149.
15. A. G. Shard, F. M. Green, P. J. Brewer, M. P. Seah and I. S. Gilmore, *The Journal of Physical Chemistry B*, 2008, **112**, 2596-2605.
16. J. A. Townes, A. K. White, E. N. Wiggins, K. D. Krantzman, B. J. Garrison and N. Winograd, *The Journal of Physical Chemistry A*, 1999, **103**, 10-12.
17. S. J. Pachuta and R. G. Cooks, *Chemical Reviews*, 1987, **87**, 647-669.
18. H. W. Werner, *Journal of Applied Physics*, 1976, **47**, 1232-1232.
19. G. Gillen, L. King, B. Freibaum, R. Lareau, J. Bennett and F. Chmara, *Journal of Vacuum Science & Technology A: Vacuum, Surfaces, and Films*, 2001, **19**, 568-575.
20. T. Mouhib, C. Poleunis, R. Möllers, E. Niehuis, P. Defrance, P. Bertrand and a. Delcorte, *Surface and Interface Analysis*, 2013, **45**, 163-166.

21. Y. He, H.-Y. Chen, J. Hou and Y. Li, *Journal of the American Chemical Society*, 2010, **132**, 1377-1382.
22. M. Lenes, G.-J. a. H. Wetzelaer, F. B. Kooistra, S. C. Veenstra, J. C. Hummelen and P. W. M. Blom, *Advanced Materials*, 2008, **20**, 2116-2119.
23. H. Bronstein, Z. Chen, R. S. Ashraf, W. Zhang, J. Du, J. R. Durrant, P. S. Tuladhar, K. Song, S. E. Watkins, Y. Geerts, M. M. Wienk, R. a. J. Janssen, T. Anthopoulos, H. Sirringhaus, M. Heeney and I. McCulloch, *Journal of the American Chemical Society*, 2011, **133**, 3272-3275.
24. R. A. L. Jones, L. J. Norton, E. J. Kramer, F. S. Bates and P. Wiltzius, *Physical Review Letters*, 1991, **66**, 1326-1329.
25. S. Kouijzer, J. J. Michels, M. van den Berg, V. S. Gevaerts, M. Turbiez, M. M. Wienk and R. A. J. Janssen, *Journal of the American Chemical Society*, 2013, **135**, 12057-12067.
26. S. Shoaee, M. P. Eng, E. Espíldora, J. L. Delgado, B. Campo, N. Martín, D. Vanderzande and J. R. Durrant, *Energy and Environmental Science*, 2010, **3**, 971-971.
27. A. Rao, M. W. B. Wilson, H. J. M, S. Albert-Seifried, H. Bassler and R. H. Friend, *Journal of the American Chemical Society*, 2010, **132**, 12698-12703.
28. P. Westacott, J. R. Tumbleston, S. Shoaee, S. Fearn, J. H. Bannock, J. B. Gilchrist, S. Heutz, J. de Mello, M. Heeney, H. Ade, J. Durrant, D. S. McPhail and N. Stingelin, *Energy and Environmental Science*, 2013, **6**, 2756-2764.
29. D. Chen, F. Liu, C. Wang, A. Nakahara and T. P. Russell, *Nano Letters*, 2011, **11**, 2071-2078.
30. H. W. Ro, B. Akgun, B. T. O. Connor, M. Hammond, R. J. Kline, C. R. Snyder, S. K. Satija, A. L. Ayzner, M. F. Toney, C. L. Soles and D. M. Delongchamp, *Macromolecules*, 2012, **45**, 6587-6599.
31. T-H. Lee, K-Y. Wu, T-Y. Lin, J-S. Wu, C-L Wang, and C-S. Hsu, *Macromolecules* 2013**, *46***, 7687-7695
32. D. Gendron and M. Leclerc, *Energy and Environmental Science*, 2011, **4**, 1225-1237.
33. C. Piliego, T. W. Holcombe, J. D. Douglas, C. H. Woo, P. M. Beaujuge and J. M. J. Fréchet, *Journal of the American Chemical Society*, 2010, **132**, 7595-7597.

Chapter 4

The role of intermixed phases in organic photovoltaic blends

4.1 Introduction

Organic photovoltaics (OPVs) consisting of a semiconducting polymer and a fullerene, blended into a bulk heterojunction (BHJ), offer great potential for high-throughput processing and promise to drastically lower material costs when compared to many of their inorganic counterparts. Over the last few years, there has been phenomenal improvement in the power conversion efficiency (PCE) within the OPV field due to increased commercial and academic interest, resulting in devices with certified efficiencies of 10%.[1] Nonetheless, there still remains a significant challenge in understanding the complex microstructure that is formed upon deposition of the donor:acceptor blend and how this is related to the series of processes that lead to maximum photocurrent.

The rapid enhancement of PCE of OPVs in recent years has been in large part due to the wide range of novel polymers that have been developed, many of which consist of "push-pull" alternating monomer units.[2-6] These new materials have, however, been reported to form a variety of microstructures and can require widely different processing protocols with respect to selection of solvents and blend composition, use of additives, specific thermal treatments,[7-8] *etc.*, in order to produce efficient devices. For every newly developed material system, intricate trial-and-error procedures are required to optimise OPV performance. For this reason enhancing the understanding of the interplay between desirable microstructural characteristics and the optoelectronic processes is vital for creating a platform that allows designing from the outset strategies of how to process such a diverse range of materials into efficient cells.

Establishment of relevant structure/property/processing inter-relationships is rendered complex by the fact that recent work indicates that not only the crystalline fractions in organic donor: acceptor blends may play an important role with respect to their OPV performance, but also their less ordered phases where a more pronounced intermixing of the components can be expected[9-23] (leading in most cases to amorphous solid solutions of the two components). For example Pfannmöller *et al.*, observed within the BHJ of poly(3-hexylthiophene-2,5-diyl) (P3HT): [6,6]-

phenyl-C61-butyric acid methyl ester (PCBM) system,[9] using analytical electron microscopy, the presence of an intermixed phase in addition to the relatively pure phases formed by the two components (*i.e.* P3HT and PCBM). Furthermore work by Treat *et al*., assessed the temperature dependence of mixing of different fullerenes into the amorphous phase of different semicrystalline semiconducting polymers;[10,11] while Collins *et al.* and Watts *et al.* convincingly showed that at quasi-thermodynamic equilibrium, there is still a significant amount of fullerene intermixed within the polymer, implying the persistent presence of this amorphous solid solution.[12,13] Other work[14-23] further confirms the presence of such an additional phase in a range of polymer:fullerene systems with possible implications on how the photo-physical processes in such systems are described

Conventionally, charge generation in OPVs has been considered to occur via photon absorption in a neat phase of one of the two active components, leading to the generation of an exciton which migrates to an interface between relatively phase-pure donor and acceptor domains within the BHJ structure before undergoing exciton dissociation over one or more steps that can lead to the generation of free charges.[24] However, in light of the recent reports of the presence of a finely intermixed phase which can comprise a significant fraction of the BHJ structures and other reports of ultrafast charge generation (<200 fs) in different polymer:fullerene systems,[25-29] the question might be raised whether the intermixed phase also contributes to charge generation. For instance, Troshin *et al.* found a strong correlation between the relative solubilities of the two components and the OPV performance of the corresponding BHJ film.[30] This is in agreement with more recent work by Treat *et al*., who studied the miscibility of different fullerene derivatives in a semicrystalline donor polymer and the effects on phase separation and device performance.[11] Moreover, the Siebbles research group observed that the charge generation in P3HT:PCBM could occur on ultrafast timescales and hence postulated that such processes may take place via a more direct route than described by the conventional model.[25] Clearly, subtly differing or competing processes will play a role in photogeneration depending on the phase morphology of the active layer, but there remains significant uncertainty about which features of the active layers'

microstructure and phase morphology govern charge generation within BHJ systems and this raises interesting questions regarding our current conception of an "ideal" microstructure for OPV devices.

The phase morphology (*e.g*. two-phase structure comprised of relatively pure phases *vs.* three phase morphology that comprises also an intermixed phase) that is formed by the active layer of a BHJ will depend on various parameters, including the miscibility of the two components and the processing routes selected to deposit the BHJ. These effects can be expected to be particularly relevant for some of the more recent, non-crystalline donor materials where the phase purity of this component can no longer be governed by crystallisation. Nonetheless, the relatively crystalline P3HT:PCBM blend as a model system is discussed here. This prototypical OPV binary has been shown to often exhibit a three-phase microstructure.[9,10,12] P3HT of two different weight-average molecular weights (M_w)[31] was selected to provide an additional tool to manipulate the phases that may be present in such blends via the length of the donor polymer chains, in analogy to cross-linked polymer:diluent systems where the molecular weight of the polymer has been observed to play a large role in the mixing behaviour.[32] The semicrystalline nature of both components should offer further freedom in varying the relative fraction of phases present. An additional benefit of using P3HT as a donor polymer is that its steady-state UV-vis absorption is much more sensitive to the local environment (e.g. backbone planarity, polymer aggregation) than many other materials, which can allow more localised insight into the molecular surroundings of this polymer. It is noted here that aggregation can occur in both crystalline and non-crystalline fractions of the material, as the ordering required to observe spectroscopic changes can be much more localised than the long-range order expected from a crystal lattice.

4.2 Results and discussion

The P3HTs of choice were a material of low M_w (denoted in the following: "L-P3HT", M_w = 7.2 kg/mol) which forms a chain-extended microstructure,[33-35] and a high molecular weight P3HT ("H-P3HT", M_w = 135 kg/mol) which will solidify in a semicrystalline, two-phase (amorphous/crystalline) microstructure[33-35] upon typical solution processing. Indeed, the H-P3HT will be comprised of a significant portion of amorphous material with tie molecules, entanglements and loops (see schematic inset Figure 4.1-B) capable of readily incorporating fullerene molecules to form an intermixed phase. The fullerene content was also varied, and blends were produced of two compositions (*i.e.* 5 and 50 wt%) for both the L-P3HT and H-P3HT by spin-coating as described in the Materials and methods section and utilising the as-cast samples. It may be expected that the blends of a lower PCBM fraction will be in a regime, where a considerable fraction of the fullerene is fully miscible with the P3HT without significantly altering the polymer microstructure.[36] In contrast, at higher PCBM loading, the fullerene is likely to affect the ordering/aggregation of the polymer.[36.37] Note also that the most efficient devices have been reported for blends comprising around 50 wt% PCBM.[36,37]

The charge generation yield of the various P3HT:PCBM systems was probed by transient absorption spectroscopy (TAS). TAS measures the yield and decay dynamics of the dissociated polarons in these blend systems. The decay dynamics are indicative of the rate of non-geminate recombination, whilst the initial amplitude Δ*OD* is indicative of the initial yield of dissociated charges, attributed to dissociated polarons. The yield of dissociated polarons is proportional to the observed Δ*OD*, given that for the same material system, the extinction coefficient of the probed species remains constant.[38] Furthermore, it has been shown previously that, for systems comprising P3HT:PCBM, the Δ*OD* correlates strongly with the short circuit current (J_{sc}) of devices and hence the Δ*OD* can be used as a convenient tool to investigate photo-physical processes that are relevant to devices.[39]

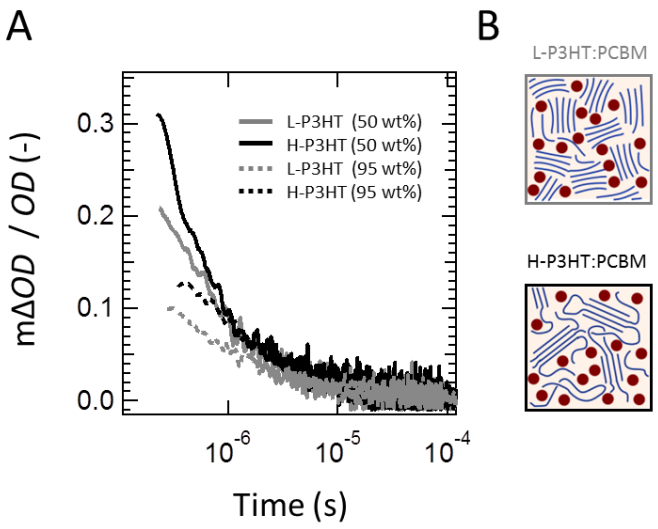


Figure 4.1: Molecular-weight dependence of dissociated polaron yield (Δ*OD*) of P3HT:PCBM binary blend films. **A**: Transient absorption yield and decay dynamics displaying the photo-induced absorption of $P3HT^+$ polarons (980 nm), following pulsed laser excitation (520 nm). A comparison is shown between P3HT:PCBM blends comprising P3HT of different molecular weight: M_w = 7 kg/mol (red) and M_w = 135 kg/mol (blue). The P3HT fraction (wt %) is also given. The blends were co-deposited from chlorobenzene (20 mg/ml). **B**: Schematics depicting the proposed microstructure of L-P3HT:PCBM (top) and H-P3HT:PCBM (bottom) blends.

Micro-second-transient absorption studies of films were carried out at low-intensity (< 4 μJ/cm^2) excitation conditions and data was generated at a probe wavelength of 980 nm corresponding to polymer positive polarons ($P3HT^+$).[40] All transients exhibited power law ($\Delta OD \propto t^{-a}$) and oxygen-independent decay dynamics, consistent with their assignment to polaron rather than triplet absorption. Whilst similar decay dynamics were observed for all films noticeable differences in dissociated polaron yield (Δ*OD*) were found between blends comprising H-P3HT and L-P3HT, respectively (Figure 4.1 A). The H-P3HT:PCBM systems consistently exhibited a considerably larger Δ*OD* – around 30 % (at 400 ns) higher for the binaries comprising 50 wt% P3HT. Similarly, at a P3HT content of 95 wt%, the Δ*OD* (at 400 ns) is approximately 40 % higher for the H-P3HT:PCBM blend when compared to L-P3HT:PCBM. This corresponds to a 30-40% higher yield of dissociated polarons. At higher PCBM content, larger Δ*OD* are measured compared to the binaries comprising 95 wt% P3HT, consistent with a recent hypothesis that the PCBM aggregation, which generally occurs at this

composition, is a key driver of charge separation in such systems.[41] Moreover, the amplitudes of observed decay transients varied approximately linearly with excitation density, and the decay dynamics of the dissociated polaron absorption for all the blend films were very similar, indicating that neither saturation effects nor non-geminate losses prior 200 ns significantly distorted this comparison.

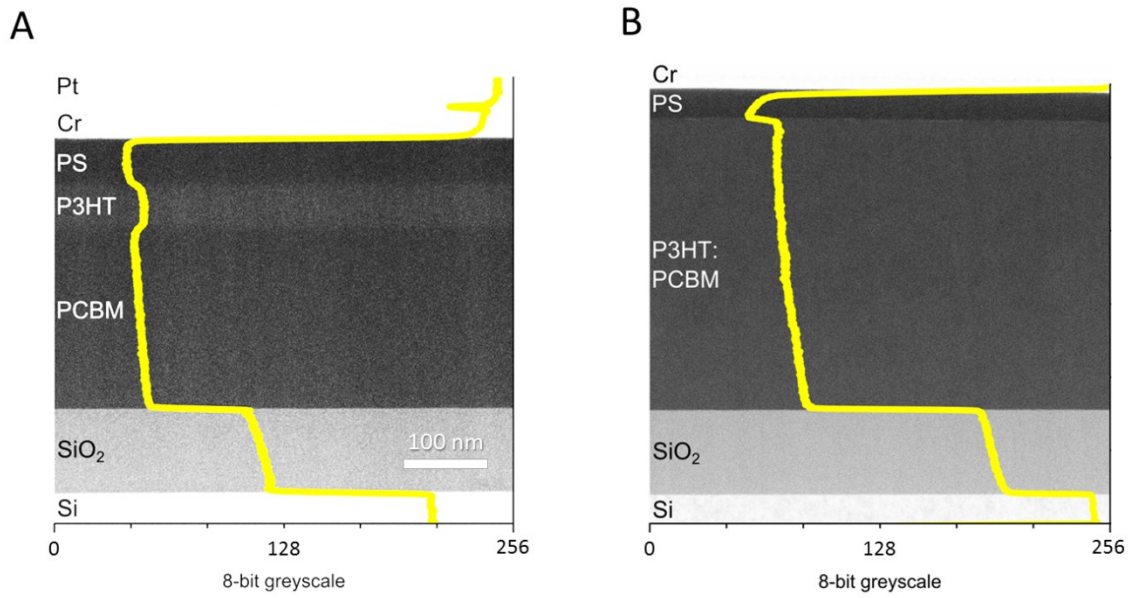


Figure 4.2: High resolution HAADF STEM images and overlaid integrated intensity profiles (yellow) through the vertical composition of the as-cast (A) and annealed (30s, 150 °C) (B) H-P3HT/PCBM bilayers. The x-axis corresponds to 8-bit greyscale, where 0 = black and 255 = white. Intermediate values are the remaining 254 shades of grey. The thicknesses observed here are in the range expected for such processing conditions. The scale bar inset in A also applies to B.

The question arises why such differences are observed in the Δ*OD* of the various P3HT:PCBM blends and how these relate to the different phase morphologies expected to form in the four binaries. Therefore, temperature-dependent miscibility of the fullerene in the two P3HTs[10] was investigated as a tool to try to understand and quantify the composition of the intermixed phase. For this purpose depth profile secondary ion mass spectrometry (D-SIMS) was conducted and followed procedures established by Treat *et al.*[10] This required fabrication of bilayers of the polymer/fullerene systems through lamination, followed by an annealing procedure to drive the interdiffusion of the

deuterated PCBM into the P3HT layer, rather than deposition of the two components from a common solvent as used for the sample preparation for TAS.[10]

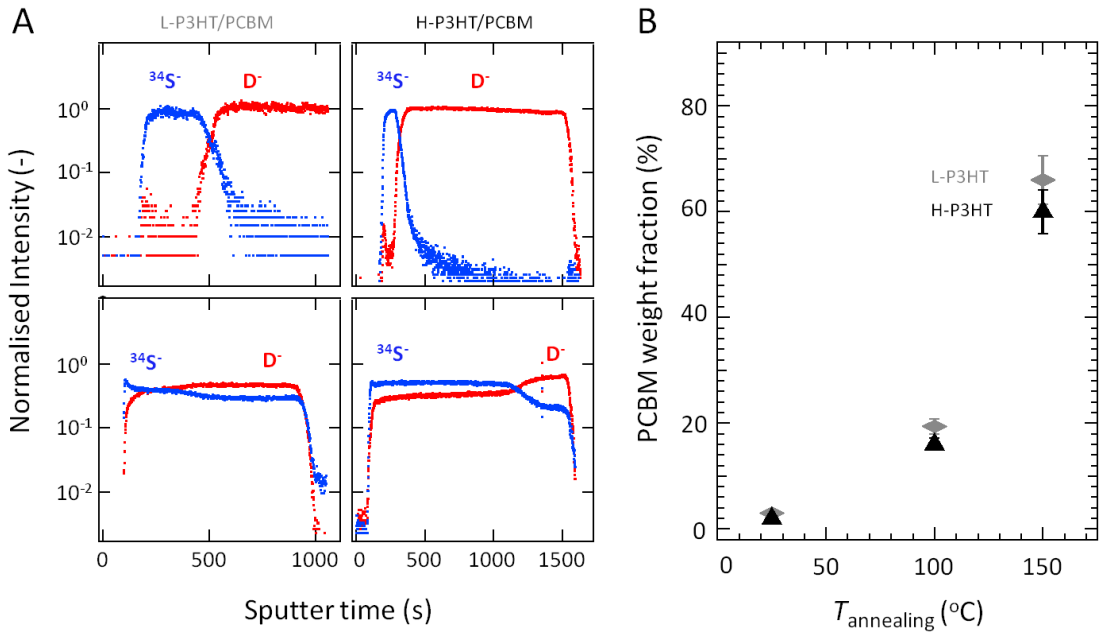


Figure 4.3: Depth profile of P3HT/PCBM bilayers, as-prepared and thermally annealed, performed by depth profile SIMS. **A:** Depth profiles of as-cast bilayers L-P3HT/PCBM (top left), H-P3HT/P3HT (top right) and annealed (150 °C, 30 s) bilayers L-P3HT/PCBM (bottom left) and H-P3HT/PCBM (bottom right). Sulphur trace (corresponding to P3HT) and deuterium trace (corresponding to D5-PCBM) are shown in blue and red, respectively. **B:** Quantity of measured PCBM into L-P3HT (grey diamonds) and H-P3HT (black triangles) deduced from the D-SIMS data presented in (A) as a function of temperature after annealing for 30 s. The quantity of intermixed PCBM is deduced from the empirical model derived in Chapter 3.

First the bilayers were scrutinised to check whether clean bilayers (non-intermixed) structures had been obtained by the lamination process. Sharp interfaces and distinct layers were indeed observed in high angle annular dark field scanning transmission electron microscopy (HAADF STEM) (Figure 4.2 A), implying that no significant intermixing had occurred during the fabrication of the bilayer. The multilayer structure is further discernable via the integrated grey-scale intensity line plot (overlaid in yellow), whereby the P3HT layer has a sufficiently higher intensity. These findings imply that at room temperature a bilayer with a sharp interface is maintained between the P3HT and PCBM. This was confirmed by the depth profiles of the as-prepared bilayers obtained from D-SIMS, which displayed subsequent layers that were sulphur rich (P3HT) and deuterium rich (D5-PCBM)

(Figure 4.3 A top panel), agreeing with the observed contrast in TEM. It is interesting to note that the offset (the trailing edge) of the ($^{34}S^-$) P3HT layer is more gradual than the onset (the leading edge). The shape of both the leading and trailing edges at the interfaces suggests a small degree of ion beam induced mixing. However, the more extended trailing edge also indicates some intermixing of the two layers at this interface. For this reason, analysis of layer composition was performed in the central region, away from both interfaces.

After only a short annealing step (30 s) at 150 °C, there is no longer an interface between the P3HT and D5-PCBM discernable from HAADF STEM (Figure 4.2 B), implying that intermixing of the two components has occurred. This intermixing is further confirmed by D-SIMS (Figure 4.3 A, bottom panels) where the vertical composition appears to have moved towards a more evenly distributed state. We note that after annealing the depth profiles do not exhibit a diffusion profile, indicating that a diffusion equilibrium has been reached. Additionally, the H-P3HT/PCBM annealed bilayer appears to have a greater vertical compositional contrast when compared to the L-P3HT analogue. A possible explanation for this are the differences in microstructure of the neat polymers. The L-P3HT is likely to adopt an extended chain microstructure, with little interconnectivity between crystallites. This may facilitate either uptake of PCBM into the matrix or allow diffusion of these short chains into the fullerene, thereby promoting complete vertical mixing. Conversely the entangled nature of H-P3HT would act to oppose both of these processes. These observations are a clear indication of a certain degree of miscibility between the donor and acceptor material. In order to provide a comparison between the intermixing between the L-P3HT/PCBM and H-P3HT/PCBM bilayers we studied the signal observed for the fullerene that had diffused into the polymer layer at a given temperature. The intensity of this signal in relation to a reference sample of neat D5-PCBM was used to determine the relative intensity of D5-PCBM signal, which was then converted into a weight fraction using the exponential fit derived in Chapter 3. Surprisingly, especially when considering the large differences observed in TAS for H-P3HT:PCBM and L-P3HT:PCBM blends, no significant

variation was found in the temperature-dependent intermixing between P3HT/PCBM bilayers comprising P3HT of different M_w (Figure 4.3 B) after annealing.

Does the D-SIMS data imply that there is no correlation between miscibility and charge generation? It may, but a number of other possibilities could also explain the fact that different Δ*OD* values are measured in TAS while similar PCBM:P3HT miscibility are found in D-SIMS, including: differences in the distribution of the PCBM or P3HT fraction within the various blend structures (*e.g.*, domain size or shape); kinetic effects of crystallisation related to the M_w of the polymer; or differences in the vitrification effect of the PCBM, to name a few. A further possibility is that the different processing routes, *i.e.* deposition from a common solvent for the fabrication of thin blend films (as used for TAS measurements) *vs*. preparation of neat layers that are laminated into bilayers followed by solid-sate mixing through interdiffusion of the fullerene (as used for the D-SIMS analysis), could lead to different thin-film microstructures in such binaries, not allowing a straight-forward comparison. In fact, PCBM is known to act as vitrifier for P3HT when they are deposited from a common solvent,[37] while the polymer very likely can more readily crystallise in the absence of the fullerene, as is the case for the neat P3HT films during the bilayer fabrication.

A better understanding of the microstructures of H-P3HT:PCBM and L-P3HT:PCBM blends and their corresponding H-P3HT/PCBM, L-P3HT/PCBM bilayers is hence required. As a simple probe of the microstructure of these systems (as prepared and annealed) UV-vis spectroscopy was utilised in this chapter because the optical absorption of P3HT is very sensitive to changes in the local environment and molecular arrangement of the P3HT macromolecules, and can be interpreted using the Spano model of weakly interacting *H*-aggregates.[42] According to this model, the ratio of the 0-0/0-1 vibronic transitions (at ~595 and ~550 nm, respectively, see Figure 4.4) can be related to the magnitude of aggregation and, therefore, intermolecular coupling within the system. In addition, the disordered polymer chains give rise to a higher energy, lower wavelength, λ, absorption (at λ < 540 nm).

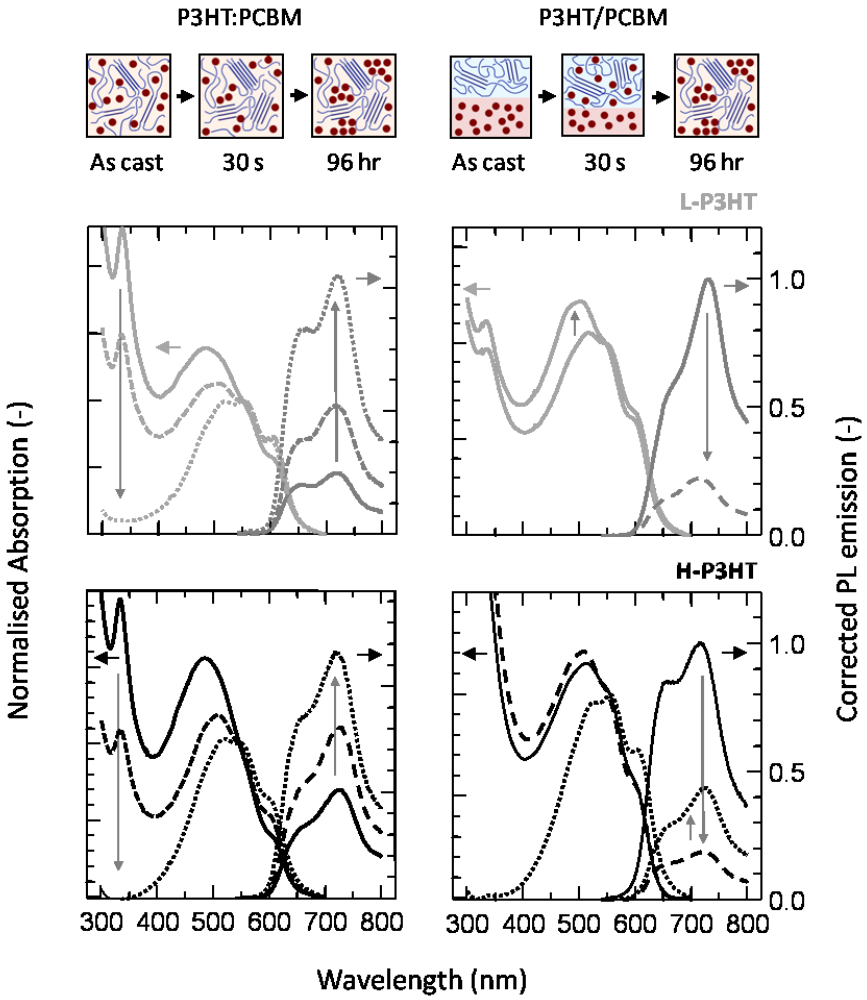


Figure 4.4: Evolution of optoelectronic and structural properties of P3HT:PCBM and P3HT/PCBM systems with processing, thermal annealing and molecular weight. **Top panel**: Schematics illustrating the structural evolution of P3HT:PCBM 50 wt% blends (left) and P3HT/PCBM bilayers (right) as deduced from the UV-vis and PL data presented in the two lower panels. The blend system exhibits the most intermixed structure. Annealing for 30 s enhances the fraction of polymer aggregates. Annealing for longer times additionally promotes the crystallisation of PCBM. The bilayer system, exhibits a higher fraction of aggregates initially; annealing for 30 s promotes interdiffusion of PCBM, disrupting some polymer aggregates. Annealing for 96 hours promotes macroscopic crystallisation of PCBM. **Middle panel**: UV-vis and PL spectra obtained for systems of L-P3HT:PCBM. **Bottom panel**: UV-vis and PL spectra of H-P3HT:PCBM binaries. A comparison is shown for all systems: as-cast (*i.e.* as-prepared) (solid lines), and annealed at 150 ^{o}C for 30 s (dashed) and 96 hours (dotted). (UV-Vis absorption spectra were normalised to the 0-1 vibronic transition (~550 nm). Photoluminescence spectra have been corrected for the absorption at the excitation wavelength 520 nm and then normalised to the emission of the as-cast sample.

Tellingly, considerable differences were observed between the spectra obtained for P3HT:PCBM thin films that were deposited from a common solvent (Figure 4.4 – left panels) and P3HT/PCBM bilayers (Figure 4.4 – right panels). The as-cast blend films featured noticeably larger contributions from the absorption related to the non-aggregated (*i.e.* molecularly largely disordered) polymer fractions, when compared to that of the as-cast bilayers (Figure 4.4, solid lines). This is

consistent with the fact that the as-cast blend films also exhibit a suppressed 0-0/0-1 absorption ratio – a further indication that the polymer chains are more poorly aggregated in these systems. These observations imply that in the as-cast P3HT:PCBM blends, the fullerene indeed acted as vitrifier, preventing molecular ordering in the polymer– as found previously, while in the as-cast P3HT/PCBM bilayers– the polymer is relatively well aggregated as it could order in a reasonably unhindered manner leading to the enhanced 0-0/0-1 absorption feature. Note in addition, that for both the blend and bilayer systems, the L-P3HT showed a higher 0-0/0-1 absorption ratio when compared to the H-P3HT; this enhanced aggregation of L-P3HT was attributed to the differences in kinetics of ordering between the two different donor polymers, with the low molecular weight material being able to order more readily. These observations appear to correlate with grazing-angle incidence wide-angle X-ray scattering (GIWAXS) (Figure 4.5), whereby the L-P3HT:PCBM blend exhibits more intense/sharper reflections corresponding to molecularly more ordered P3HT when compared to H-P3HT:PCBM blends. Upon short annealing (30 s / 150 °C) the P3HT:PCBM blends showed a significant change in their optical absorption behaviour (Figure 4.4 – left panels; dashed lines) independent of the molecular weight of the polymer. In both the L-P3HT and H-P3HT systems there is a noticeable increase in 0-0/0-1 absorption ratio with respect to the as-cast films. This is accompanied by a decrease in the higher-energy (lower wavelength) absorption, corresponding to a reduction of the disordered polymer fractions (Figure 4.4). These observations are all consistent with the picture of the polymer aggregating upon annealing and, as a consequence, expelling at least a certain fraction of the PCBM molecules, as schematically depicted in Figure 4.4, left panel. The latter picture is supported by the fact that annealing also leads to significantly enhanced photoluminescence (PL) (4x and 2x increase for L-P3HT and H-P3HT respectively), consistent with the two components phase separating, as schematically depicted in Figure 4.4, top left panel.

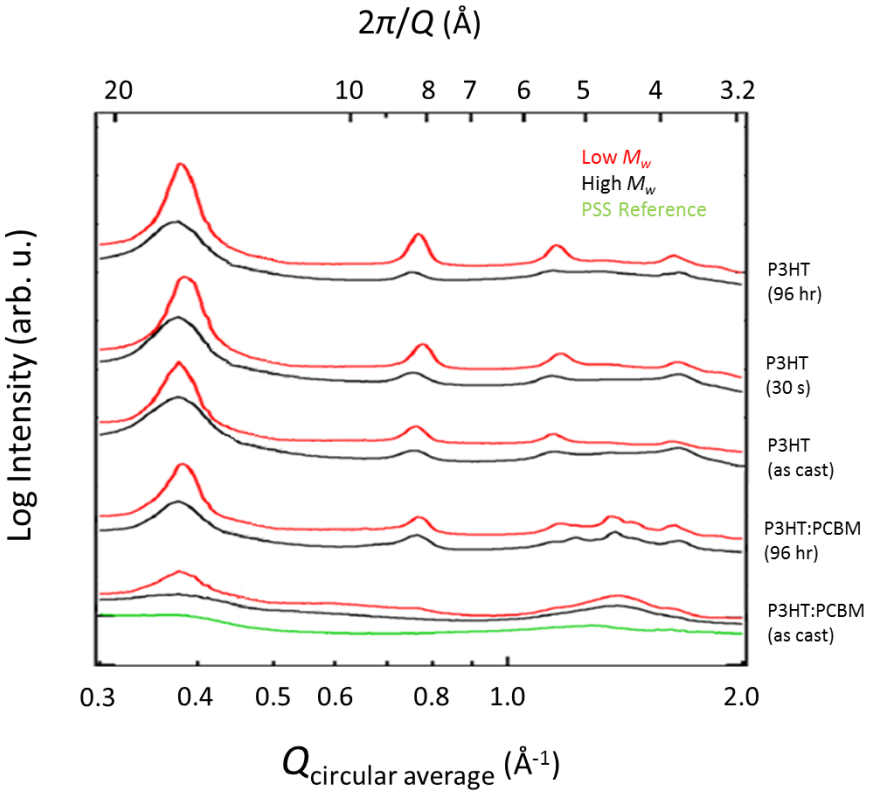


Figure 4.5: Grazing-angle incidence wide-angle X-ray scattering of neat P3HT and P3HT:PCBM blends for L-P3HT (red) and H-P3HT (black). The intensity plotted in the integrated circular average of the scattering pattern. Samples were annealed at 150 ^{o}C, for the time indicated in brackets, with the exception of the *as cast* samples. The circular average was used to reduce the effect of any differences in edge-on orientation between samples.

Annealing of the P3HT:PCBM blends for a further 96 hours at 150 ^{o}C to drive the systems more towards their quasi-thermodynamic equilibrium state,[13] resulted in additional changes in their UV-vis absorption behaviour (dotted lines, Figure 4.4, left panels). Firstly, the fullerene absorption around ~340 nm is greatly reduced during this additional annealing; this has been previously ascribed to the crystallisation of the PCBM into microscopically large crystals[13] that were observed in optical microscopy (Figure 4.6). Near-edge X-ray absorption fine structure (NEXAFS) was utilised to confirm and quantify the reduced content of the fullerene within the polymer matrix yielding fullerene contents of ~5.2 and 7.1 wt% for H-P3HT and L-P3HT, respectively (Figure 4.6). For the blend films comprising H-P3HT:PCBM (Figure 4.4, bottom panels), the 0-0 absorption transition became more pronounced upon this treatment while for the binary structures fabricated with L-

P3HT (Figure 4.4, middle panels) no further increase in the degree of aggregation was found, supporting the picture that the ordering of L-P3HT:PCBM blend films is kinetically less hindered due to the predominantly un-entangled nature of this short-chain P3HT.

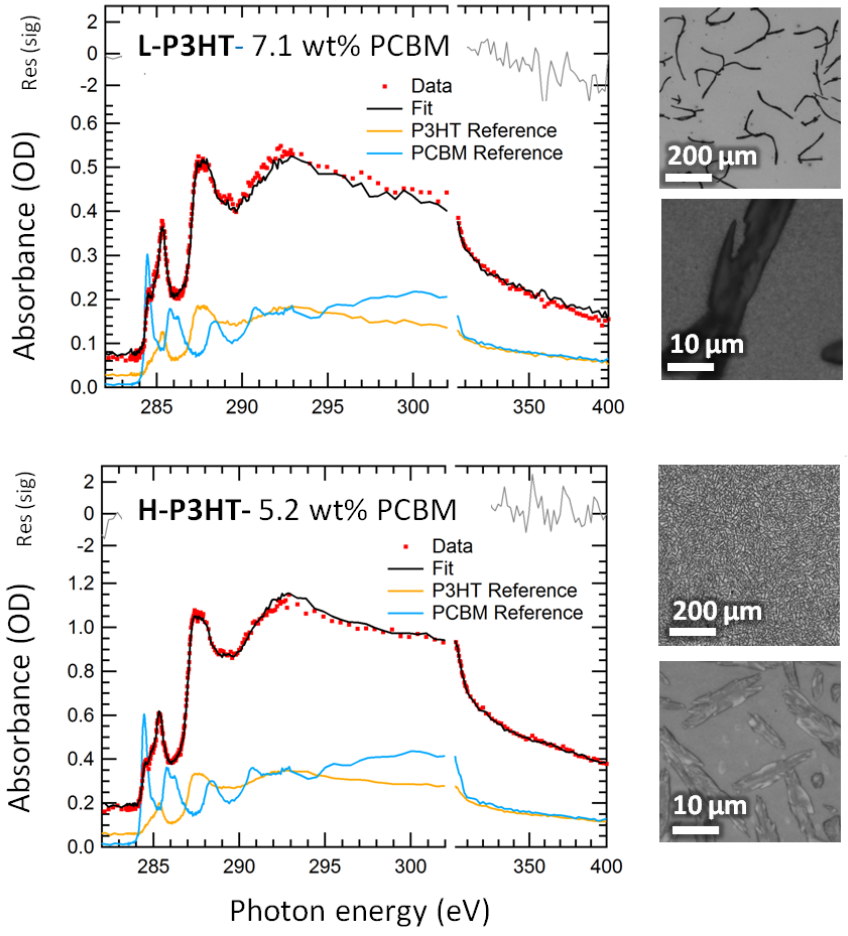


Figure 4.6: Near edge X-ray absorption fine structure (NEXAFS) spectra and microscope images of 96 hour annealed blend films (150 ^{o}C) comprised of PCBM blended with L-P3HT (top) and H-P3HT (bottom). NEXAFS spectra show measured data, fit and residuals. From these fits the PCBM content of the polymer matrix was calculated. Optical micrographs (right) display the macroscopic crystals of PCBM.

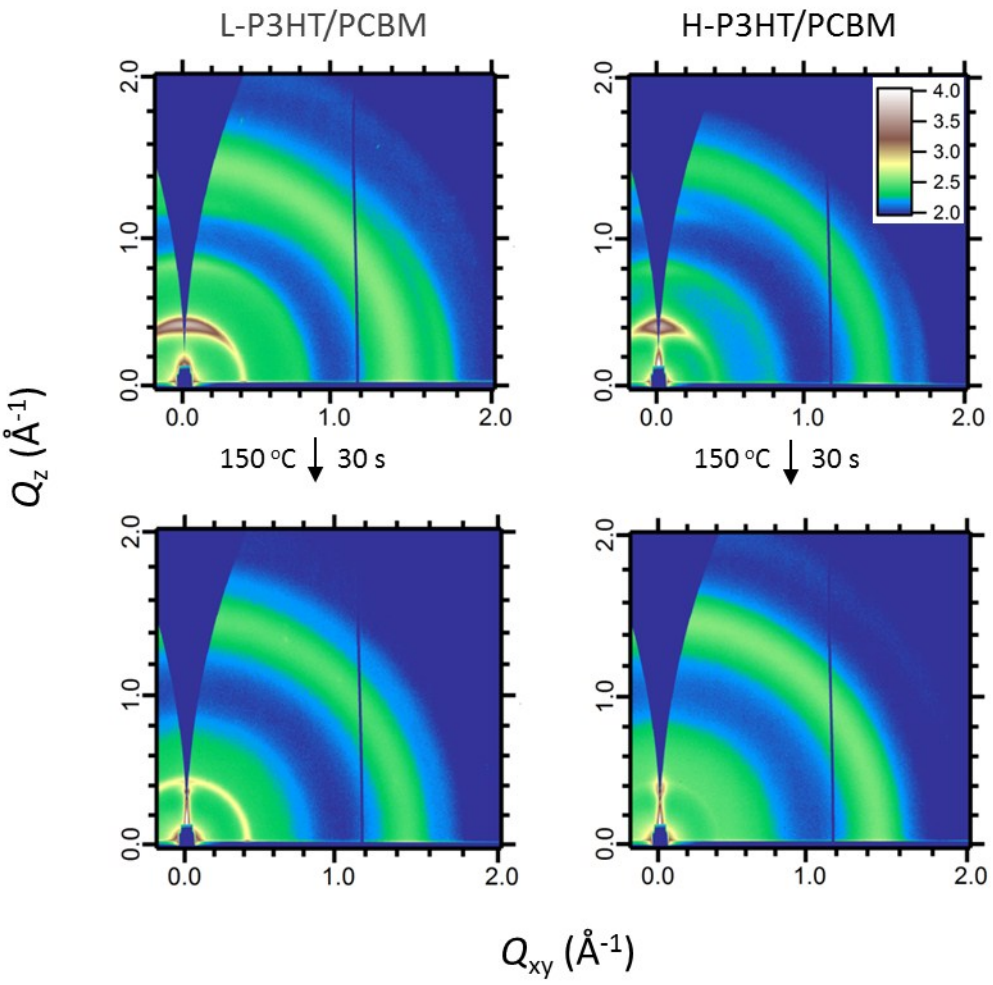


Figure 4.7: Grazing-angle incidence wide-angle X-ray scattering patterns of as-cast and annealed P3HT/PCBM bilayers. **Left**: L-P3HT/PCBM bilayers, as-cast (top) and annealed at 150 °C for 30s (bottom). **Right**: H-P3HT/PCBM bilayers, as-cast (top) and annealed at 150 °C for 30 s (bottom).

In stark contrast to the blend films, L-P3HT/PCBM and H-P3HT/PCBM-bilayers showed a significant increase in their disordered absorption feature at low wavelengths already upon annealing for 30 s, accompanied by a small decrease in the relative 0-0 transition (Figure 4.4, right panel; dashed lines). This strongly suggests that interdiffusion of the PCBM molecules into the polymer layer disrupts the aggregated P3HT moieties, as previously postulated,[10] leading to this observed changes in the UV-vis spectra. In accord with the former observation is the fact that such short-annealed bilayers displayed –in strong disparity with the P3HT:PCBM blend systems– a five-fold *decrease* in PL when compared to the as-prepared bilayers (Figure 4.4, right panels), concurrent

with a higher degree of intermixing of the fullerene into the polymer. These observations appear to agree with initial GIWAXS measurements where changes in the -diffraction are observed (Figure 4.7). The latter is more pronounced in bilayers comprised of H-P3HT, possibly supporting that the diffusion of PCBM may disrupt the aggregation of P3HT for this molecular weight. The dependence of this effect on molecular weight is consistent with a previous report using lower molecular weight P3HT (M_w = 42.2 kg/mol) where diffusion of PCBM did not strongly disrupt P3HT order.[15] Note, though, that in H-P3HT/PCBM systems prolonged annealing (96 hours / 150 °C) resulted in an increase in the PL compared to the short-annealed system, suggestive of the components phase separating during this treatment.

It is clear from the UV-vis, PL spectroscopy data and complementary GIWAXS measurements that the two processing protocols discussed here lead to entirely different phase morphologies in the various P3HT:PCBM and P3HT/PCBM systems investigated here. As a consequence, the resulting architectures follow different solid-state structure developments upon further post-deposition treatment, such as annealing. It is therefore evident that the D-SIMS and TAS data presented in Figure 4.1 and Figure 4.2 address different microstructures and, hence, require greater understanding to be compared directly. Because the four systems –*i.e.* H-P3HT:PCBM, L-P3HT:PCBM, H-P3HT/PCBM, L-P3HT/PCBM– provide a range of different phase morphologies, it is however also clear that obtained is a means to elucidate how aggregation, phase separation and intermixing affect the optoelectronic processes. Indeed, the largest portions of intermixed phase are found in the as-cast H-P3HT:PCBM blend films and L-P3HT/PCBM bilayer structures that were annealed for 30 s at 150 °C, while prolonged annealing of H-P3HT:PCBM leads to a system that comprises a considerable fraction of relatively pure phases. A well-defined two-phase system is obviously provided by the as-prepared bilayers (see Figure 4.4 for schematic illustrations of the various microstructures).

When comparing the binaries of highest/lowest intermixing, it is intriguing to find that the highest charge generation deduced from the Δ*OD* measured in TAS is found for the most intermixed

structures: *i.e.* as-cast H-P3HT:PCBM blend films and short-annealed H-P3HT/PCBM bilayers (Figure 4.8). The stronger the systems phase separate, driven by annealing of P3HT:PCBM blend thin-films, the lower the measured Δ*OD*; as-prepared bilayers feature the lowest charge generation.

Table 4.1: Relative PL intensity, PL quenching (PLQ) and dissociated polaron yield (ΔOD) of P3HT-PCBM systems**.**

		Photoluminescence		**TAS**	
		Rel. intensity	PLQ	m*ΔOD/OD*	m*ΔOD/PLQ*
Blend	(wt%)	(%)	(%)	(at 400 ns)	
H-P3HT	(100)	100	0	0	N/A
	(95)	33	68	0.13	0.19
	(50)	8	92	0.2	0.22
L-P3HT	(100)	100	0	0	N/A
	(95)	20	80	0.09	0.11
	(50)	14	86	0.16	0.19
Blend: evolution with thermal annealing					
H-P3HT:PCBM	(as cast)	8	92	0.3	0.33
H-P3HT:PCBM	(annealed, 30 s)	13	87	-	-
H-P3HT:PCBM	(annealed, 96 hr)	18	82	0.2	0.24
L-P3HT:PCBM	(as cast)	14	86	0.19	0.22
L-P3HT:PCBM	(annealed, 30 s)	28	72	-	-
L-P3HT:PCBM	(annealed, 96 hr)	57	43	0.12	0.28
Bilayer: evolution with thermal annealing					
H-P3HT/PCBM	(as cast)	89	11	0.02	0.18
H-P3HT/PCBM	(annealed, 30 s)	18	82	0.18	0.22
H-P3HT/PCBM	(annealed, 96 hr)	39	61	-	-
L-P3HT/PCBM	(as cast)	86	14	0.08	0.57
L-P3HT/PCBM	(annealed, 30 s)	20	80	0.16	0.20

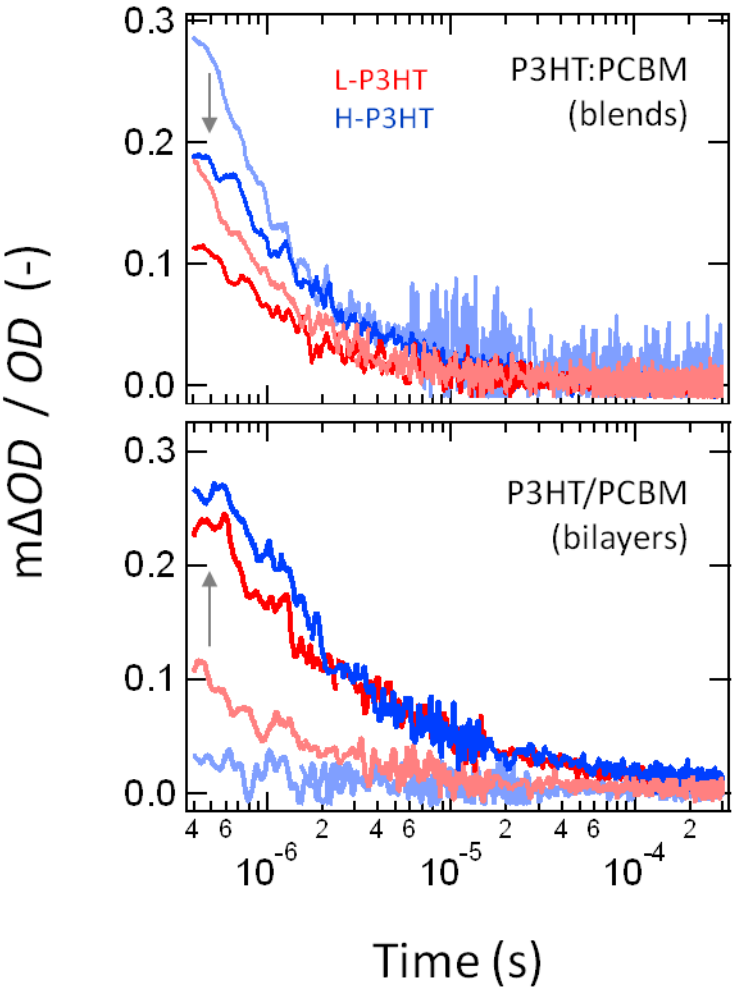


Figure 4.8: Transient absorption signals: phase purity dependence of dissociated polaron yield (Δ*OD*) of L-P3HT (red) and H-P3HT (blue) systems for P3HT:PCBM blends (top) and P3HT/PCBM bilayer (bottom) systems, following pulsed laser excitation at 520 nm at an excitation intensity of 2 µJ cm^{-2} and a probe wavelength of 980 nm. Data for as-cast samples are shown in lighter shades. Annealed samples are shown in darker shades. The bilayer samples were annealed at 150 ^{o}C for 30 s, corresponding to the most mixed state of the bilayers. The blend samples were annealed at 150 ^{o}C for 96 hours, corresponding to the most phase pure state of the blends.

Next, the difference in the transient absorption signal amplitudes of the various systems are considered. The question that arises here is why such differences are observed in the Δ*OD* for the various P3HT:PCBM samples; whether the difference originates from variation in exciton quenching at the donor/acceptor interface or, rather, whether the dissociation of charge transfer states into free photogenerated charge carriers (geminate recombination) is influencing the observed trend. The summarised Δ*O*D signal intensities are shown in Table 4.1. They are normalized for variations in the density of absorbed photons due to variations in film optical density at the excitation

wavelength, Δ*OD*/*OD* and variations in PL quenching (*PLQ*) Δ*OD*/*PLQ* observed between the blend films. It is apparent that for the as cast blends and annealed bilayer films, these changes in Δ*OD* signal intensities, and therefore yield of dissociated polarons, do not correlate with the variation in PL quenching observed between the films. As such, these variations in polaron yields cannot be assigned primarily to changes in the efficiency of exciton dissociation. Rather, as has been concluded previously for other materials systems,[40,43] the observation in variation of the polaron yield is more reasonably assigned primarily to variations in geminate recombination losses on the pico-nanosecond timescales and, thus, to the variations in the efficiency of dissociation of interfacial charge transfer (CT) states into free charges.

4.3 Conclusion

Our observations give clear guidelines on how to optimise the photo-physical processes leading to charge generation in OPV systems by providing for a certain degree of miscibility between the donor and acceptor material. Indeed, our results highlight the importance of an intermixed phase in the processes of exciton quenching and charge generation in these systems. It is important to underline, however, that it seems critical that these intermixed phases co-exist with relatively phase-pure regions (*e.g*. crystalline P3HT moieties), in agreement with recent findings.[44] In fact, full miscibility, *i.e.* formation of a one-phase system comprised of a solid solution appears not to be desirable.[15,17,45] Structures comprising low PCBM fraction, where rather complete intermixing can be expected, consistently showed lower charge generation independent of the processing protocols selected. This is because geminate recombination processes very likely will limit charge generation and device performance.[39] On the contrary, for binaries comprising 50 wt% of the fullerene where some fullerene aggregation can be expected, higher Δ*OD* values were measured. The optimum amount of intermixing still needs to be quantified and may vary from system to system; clearly, it will also depend on the lateral length scales of the phases created.

In addition, it is evident that compromises need to be reached between optimising excited state quenching, charge generation (which according to our study are favoured by phase morphologies comprising considerable fractions of an intermixed phase along with phase-pure regions) and the subsequent processes resulting in best device performance. Indeed, highest solar cell efficiencies for P3HT:PCBM systems comprising 50 wt% PCBM are obtained after annealing of solution-cast active layers – that is in a system of lower excited state quenching where larger quantities of relatively phase-pure domains of the two components can develop. Our findings moreover should assist in designing new OPV materials and aid in advancing reliable processing protocols without the need of time-consuming trial-and-error procedures.

In conclusion, our observations show the significance and intricacy of the processes leading to the structural evolution of BHJs, including: diffusion, phase separation and frequently, the interplay between crystallisation and vitrification. These processes have been shown to have a significant effect on the photo-physical processes leading to polaron formation and are believed to be strongly affected by the degree of geminate recombination which acts as a loss mechanism, tuneable by the processing route employed. Furthermore it is proposed that the molecular weight of the polymer can be used as a tool to optimise the microstructure not only by the chain extended/semicrystalline nature of L-P3HT and H-P3HT, respectively, but also because of the difference in rate of ordering seen between the two materials. Consideration of the sensitive interplay of structural processes is of paramount importance to realise a microstructure that allows formation of a certain fraction of intermixed phase. Thereby, the dependence of these processes on the initially prepared microstructure needs to be taken into account. Inducing more crystalline structures, for instance (as realised here in as-cast bilayers) reduces not only interdiffusion of the two components but also limits our means to readily induce partial phase separation. Annealing can lead to higher intermixed structures, but in other cases to more pronounced phase segregation depending on the initial solid-state microstructure, phase morphology and the ‘intrinsic’ miscibility of the system. Note in this context that changes in microstructure can also influence other

properties such as the ionisation potential of the material. Clearly, intimate knowledge of the chemical interaction potential and crystallisation behaviour between the two components will thus be a highly useful tool to predict the thermodynamically more favoured state. Such considerations can be expected to be even more relevant for systems that have a low tendency to molecularly order, such as some of the more complex donor:acceptor polymers or many of the newly developed electron accepting materials where the driving force to crystallise and, hence, phase separation is dominated by the mutual miscibility of the key components. Relatively straight-forward techniques, such as PL and UV-vis spectroscopy, thereby provide highly valuable insight in the structural features of these systems.

4.4 Materials and methods

Solutions: were prepared from chlorobenzene, by dissolving the solute at 80 ^{o}C with stirring. All of the substrates were washed sequentially in: deionised water (with 0.1 vol%) detergent); acetone and iso-propanol for 15 minutes each with ultrasonication, followed by blow-drying with nitrogen.

Blend films: were fabricated by dissolving the polymer and fullerene at appropriate ratios, so the total solute concentration was 20 mg/ml in chlorobenzene. These solutions were then spin-coated at 1200 rpm onto pre-cleaned glass substrates and dried under vacuum for 24 hours. At this point sample measurements were carried out, which are termed *as-cast*. Thermal annealing was carried out in a vacuum oven for 30 s (short annealed) and 96 hours (long annealed) in the dark and are termed *short*- and *long-annealed* within the chapter.

Bilayers: were fabricated by spin-coating PCBM 30 mg/ml at 800 rpm for 60s onto a first substrate (glass for UV-Vis, PL and TAS or SiO_2 for d-SIMS, GIWAXS samples were made on Si substrates while those for STXM were made on PSS-coated glass substrates). P3HT was then spin-

coated 20 mg/ml at 1200 rpm for 60 s onto a SiO_2 substrate. The two bilayer component layers were left under vacuum for 48 hours to aid removal of residual solvent. The P3HT layer was then delaminated using a 5 vol% solution of HF in water and subsequently floated onto a bath of deionised water. The free-floating P3HT films were then picked up by PCBM coated substrate. The bilayers were then placed under vacuum for 12 hours the aid lamination. Thermal annealing was then carried out for 30 s (short annealed) and 96 hours (long annealed). Samples prepared for D-SIMS and TEM had a subsequent layer of polystyrene floated on top to aid intensity and sputter rate calibration of the D-SIMS. Ongoing work has demonstrated good agreement with the elemental and larger fragment signals, implying that, in this case, elemental signals provide a good tool for probing molecular vertical composition.

Depth profile secondary ion mass spectrometry (D-SIMS): An Ion TOF 5 SIMS was used to measure depth profiles of bilayer samples. All samples were sputtered using a 1kV Cs^+ (~75 nA) beam across a 250 x 250 µm square. Analysis was carried out using a Bi_3^+ (~1 pA) beam over the central 50 x 50 µm region of the sputter crater with charge compensation and negative ions were collected.

Near-edge X-ray absorption fine structure (NEXAFS): was conducted at Beamline 5.3.2.2 of the ALS.[44] During measurement, the chamber was filled with 1/3 ATM He. Miscibility values of long annealed samples were determined from absorbance measurements following previously described procedures.[45]

Grazing-angle incidence wide-angle x-ray scattering (GIWAXS): measurements were carried out at Beamline 7.3.3. of the Advanced Light Source using a Dectris Pilatus 1M photon counting detector. Samples were measured at an incident angle of ~0.13^o, above the critical angle so the X-ray beam penetrated to the substrate. The photon energy used for GIWAXS was 10 keV. Air scatter which provides a background signal was reduced using helium gas.

Transmission electron microscopy (TEM): To characterise the morphology and thickness of the polymer layers an electron transparent cross-section of the polymer films on Si/SiO_2 was prepared using a focussed ion beam (FIB) dual beam system (FEI Helios NanoLab). Initially, the surface of the polymer films was coated with a thin (~15 nm) chromium layer to provide a conductive surface. A platinum strap was then deposited onto the surface to protect surface features. The region surrounding the Pt strap was then milled using 30 kV Ga^+ ions creating a lamella. The lamella, when extracted and attached to a TEM grid, was thinned using the Ga^+ beam, operated at successively lower accelerating voltages and beam currents. The prepared specimen was examined using an FEI Titan 80-300 TEM operated at 300 kV in STEM mode, with incoherently scattered electrons collected using a high angle annular dark field (HAADF) detector to form the images. The brightness and contrast of the HAADF detector are optimised to provide maximum contrast between the polymer layers. Since the cross-section was taken parallel to a cleaved crystalline edge of the Si/SiO_2 substrate, the diffraction pattern produced from the substrate can be used to tilt the lamella so that the substrate surface is parallel to the electron beam, ensuring the interfaces within the polymer films are also parallel to the electron beam.

UV-vis absorption: All measurements reported in this thesis utilised a Perkin-Elmer Lambda 35 spectrophotometer, an increment of 1 nm and acquisition rate of 980 nm/min. Displayed data are (1 – transmission) and therefore encompass both absorption and scatter.

Photoluminescence: All measurements reported utilised a Horiba Spex Fluormax-1 spectro-fluorometer with an acquisition angle of 60^o. Slit widths were set at 5 nm, and an excitation wavelength of 520 nm was used.

Transient absorption spectroscopy: excitation of the sample film was under a nitrogen (and oxygen) atmosphere and pumped with a Nd:YAG laser (Lambda Photometrics). The excitation wavelength used was 520 nm, with a pump intensity of between 2-4 $\mu J\ cm^{-2}$ using a repetition frequency of 20 Hz. The halogen lamp used was a 100 W quartz (Bentham, IL 1) with a stabilised

power supply (Bentham, 605). The probe light source was 980 nm, which had been previously ascribed to $P3HT^{+}$ polarons.[1] The probe light passing through the sample film was detected with a silicon photodiode (Hamamatsu Photonics, S1722-01). The signal from the photodiode was pre-amplified and sent to the main amplification system with an electronic band-pass filter (Costronics Electronics). The amplified signal was collected with a digital oscilloscope (Tektronics, TDS220), this was synchronised with a trigger signal of the pump laser pulse from a photodiode (Thorlabs Inc., DET210). To reduce stray light, scattered light and sample emission, a pair of monochromators and appropriate optical cut-off filters were placed before and after the sample.

4.5 References

1. M. A. Green, K. Emery, Y. Hishikawa, W. Warta and E. D. Dunlop, *Progress in Photovoltaics: Research and Applications*, 2012, **20**, 12-20.
2. Y. Liang, Z. Xu, J. Xia, S.-T. Tsai, Y. Wu, G. Li, C. Ray, and L. Yu, *Advanced Materials*, 2010, **22**, E135–E138.
3. N. Blouin, A. Michaud, and M. Leclerc, *Advanced Materials*, 2007, **19**, 2295–2300.
4. T.-Y. Chu, S. Alem, P. G. Verly, S. Wakim, J. Lu, Y. Tao, S. Beaupré, M. Leclerc, F. Bélanger, D. Désilets, S. Rodman, D. Waller, and R. Gaudiana, *Applied Physics Letters*, 2009, **95**, 063304.
5. M. C. Scharber, M. Koppe, J. Gao, F. Cordella, M. A. Loi, P. Denk, M. Morana, H.-J. Egelhaaf, K. Forberich, G. Dennler, R. Gaudiana, D. Waller, Z. Zhu, X. Shi, and C. J. Brabec, *Advanced Materials*, 2010, **22**, 367–70.
6. H. Bronstein, Z. Chen, R. S. Ashraf, W. Zhang, J. Du, J. R. Durrant, P. S. Tuladhar, K. Song, S. E. Watkins, Y. Geerts, M. M. Wienk, R. a J. Janssen, T. Anthopoulos, H. Sirringhaus, M. Heeney, and I. McCulloch, *Journal of the American Chemical Society*, 2011, **133**, 3272–3375.
7. J. Hou, H.-Y. Chen, S. Zhang, G. Li, and Y. Yang, *Journal of the American Chemical Society,* 2008, **130**, 16144–5.
8. H. Lu, B. Akgun, and T. P. Russell, *Advanced Energy Materials*, 2011, **1**, 870–878.
9. M. Pfannmöller, H. Flügge, G. Benner, I. Wacker, C. Sommer, M. Hanselmann, S. Schmale, H. Schmidt, F. a Hamprecht, T. Rabe, W. Kowalsky, and R. R. Schröder, *Nano Letters*, 2011, **11**, 3099–3107.

10. N. D. Treat, M. A. Brady, G. Smith, M. F. Toney, E. J. Kramer, C. J. Hawker, and M. L. Chabinyc, *Advanced Energy Materials*, 2011, **1**, 82–89.

11. N. D. Treat, A. Varotto, C. J. Takacs, N. Batara, M. Al-Hashimi, M. J. Heeney, A. J. Heeger, F. Wudl, C. J. Hawker, and M. L. Chabinyc, *Journal of the American Chemical Society*, 2012, **134**, 15869–15879.

12. B. A. Collins, E. Gann, L. Guignard, X. He, C. R. McNeill, and H. Ade, *Journal of Physical Chemistry Letters,* 2010, **1**, 3160–3166.

13. B. Watts, W. J. Belcher, L. Thomsen, H. Ade and P. C. Dastoor, *Macromolecules*, 2009, **42**, 8392-8397.

14. H. W. Ro, B. Akgun, B. T. O. Connor, M. Hammond, R. J. Kline, C. R. Snyder, S. K. Satija, A. L. Ayzner, M. F. Toney, C. L. Soles, and D. M. Delongchamp, *Macromolecules* 2012, **45**, 6587-6599.

15. D. Chen, F. Liu, C. Wang, A. Nakahara, and T. P. Russell, *Nano Letters*, 2011, **11**, 2071–2078.

16. W. Yin and M. Dadmun, *ACS Nano*, 2011, **5**, 4756–4768.

17. B. A. Collins, Z. Li, J. R. Tumbleston, E. Gann, C. R. McNeill and H. Ade, *Advanced Energy Materials*, 2013, **3**, 65-74.

18. J. A. Bartelt, Z. M. Beiley, E. T. Hoke, W. R. Mateker, J. D. Douglas, B. A. Collins, J. R. Tumbleston, K. R. Graham, A. Amassian, H. Ade, J. M. J. Fréchet, M. F. Toney and M. D. McGehee, *Advanced Energy Materials,* 2013, **3**, 364-374.

19. W. Chen, T. Xu,F. He, W. Wang, C. Wang, J. Strzalka, Y. Liu, J. Wen, D. J. Miller, J. Chen, K. Hong, L. Yu and S. B. Darling, *Nano Letters*, 2011, **11**, 3307–3713

20. D. M. Delongchamp, R. J. Kline and A. Herzing, *Energy and Environmental Science*, 2012, **5**, 5980-5993

21. W. Chen, M. P. Nikiforov, and S. Darling, *Energy and Environmental Science*, 2012, **5**, 8045-8074

22. B. A. Collins, J. R. Tumbleston and H. Ade, *J. Phys. Chem. Lett.*, 2011, **2**, 3135-3145 23. K. Vakhshouri, D. R. Kozub, C. Wang, A. Salleo, and E. D. Gomez, *Physical Review Letters*, 2012, **108**, 026601.

24 H. Hoppe and N. S. Sariciftci, *Journal of Materials Research*, 2004, **19**, 1924-1945

25. J. Piris, T. E. Dykstra, A. A. Bakulin, P. H. M. Van Loosdrecht, W. Knulst, M. T. Trinh, J. M. Schins, and L. D. A. Siebbeles, *Journal of Physical Chemistry C*, 2009, **113**, 14500–14506.

26. I. A. Howard, R. Mauer, M. Meister, and F. Laquai, *Journal of the American Chemical Society*, 2010, **132**, 14866–14876.

27. F. Etzold, I. A Howard, R. Mauer, M. Meister, T.-D. Kim, K.-S. Lee, N. S. Baek, and F. Laquai, *Journal of the American Chemical Society*, 2011, **133**, 9469–9479.
28. M. Tong, N. E. Coates, D. Moses, and A. J. Heeger, *Physical Reviews B*, 2010, **81**, 125210.
29. G. Grancini, M. Maiuri, D. Fazzi, a. Petrozza, H.-J. Egelhaaf, D. Brida, G. Cerullo, and G. Lanzani, *Nature Materials*, 2012, **11**, 1–5.
30. P. A. Troshin, H. Hoppe, J. Renz, M. Egginger, J. Y. Mayorova, A. E. Goryachev, A. S. Peregudov, R. N. Lyubovskaya, G. Gobsch, N. S. Sariciftci, and V. F. Razumov, *Advanced Functional Materials,* 2009, **19**, 779–788.
31. P. Schilinsky, U. Asawapirom, U. Scherf, M. Biele, and C. J. Brabec, *Chemistry of Materials*, 2005, **17**, 2175–2180.
32. P. J. Flory and J. Rehner, *Journal of Chemical Physics*, 1943, **11**, 521-526.
33. O. G. Reid, J. A. Nekuda Malik, G. Latini, S. Dayal, N. Kopidakis, C. Silva, N. Stingelin, and G. Rumbles, Journal of *Polymer Science Part B: Polymer Physics*, 2012, **50**, 27–37.
34. M. Brinkmann and P. Rannou, *Advanced Functional Materials*, 2007, **17**, 101–108.
35 R. J. Kline, M. D. McGehee, E. N.Kadnikova, J. Liu, J. M. J. Fréchet, *Advanced Materials*, 2003, **15**, 1519-1522
36. A. J. Ferguson, N. Kopidakis, S. E. Shaheen, and G. Rumbles, *Journal of Physical Chemistry C*, 2011, **115**, 23134–23148.
37. C. Müller, T. A. M. Ferenczi, M. Campoy-Quiles, J. M. Frost, D. D. C. Bradley, P. Smith, N. Stingelin-Stutzmann, and J. Nelson, *Advanced Materials*, 2008, **20**, 3510–3515.
38. A. F. Nogueria, I. Montanari, J. Nelson, J. R. Durrant, C. Winder, N. S. Sariciftci and C. Brabec, *Journal of Physical Chemistry B*, 2003, **107**, 1567-1573
39. T. M. Clarke, A. Ballantyne, S. Shoaee, Y. W. Soon, W. Duffy, M. Heeney, I. McCulloch, J. Nelson and J. R. Durrant, *Advanced Materials*, 2010, **22**, 5287-5291
40. H. Ohkita, S. Cook, Y. Astuti, W. Duffy, S. Tierney, W. Zhang, M. Heeney, I. McCulloch, J. Nelson, D. D. C. Bradley and J. R. Durrant, *Journal of the American Chemical Society,* 2008, **130**, 3030-3042.
41. F. C. Jamieson, E. B. Domingo, T. McCarthy-Ward, M. Heeney, N. Stingelin, and J. R. Durrant, *Chemical Science*, 2012, **3**, 485–492.
42. a) J. Clark, C. Silva, R. H. Friend, and F. C. Spano, *Physical Review Letters*, 2007, **98**, 206406. b) J. Clark, J.-F. Chang, F. C. Spano, R. H. Friend, and C. Silva, *Applied Physics Letters*, 2009, **94**, 163303–163306.
43. S. Shoaee, T.M. Clark, C. Huang, S. Barlow, S. R. Marder, M. Heeney, I. McCulloch and J. R. Durrant, *Journal of the American Chemical Society*, 2010, **132**, 12919-12926

44. S. Shoaee, S. Subramaniyan,H. Xin, C. Keiderling, P. S. Tuladhar, F. C. Jamieson, S. A. Jenekhe, J. R. Durrant, *Advanced Functional Materials*, 2013, **23**, 3286-3298.
45. B. A. Collins, Z. Li, C. R. McNeill and H. Ade, *Marcomolecules*, 2011, **44**, 9747-9751.
46. R. S. Loewe, P. C. Ewbank, J. Liu, L. Zhai, R. D. McCullough, *Macromolecules,* 2001, **34**, 4324.
47. A. Hexemer, W. Bras, J. Glossinger, E. Schaible, E. Gann, R. Kirian, A. MacDowell, M. Church, B. Rude, H. Padmore, *Journal of Physics: Conference Series,* 2010, **247**, 012007.
48. A. L. D. Kilcoyne, T. Tyliszczak, W. F. Steele, S. Fakra, P. Hitchcock, K. Franck, E. Anderson, B. Harteneck, E. G. Rightor, G. E. Mitchell, A. P. Hitchcock, L. Yang, T. Warwick, H. Ade, *Journal of Synchrotron Radiation*, 2003, **10**, 125.
49. B. A. Collins, H. Ade, *Journal of Electron Spectroscopy and Related Phenomena*, 2012, **185**, 119.

Chapter 5

Fullerene-induced vitrification of semiconducting donor polymers

5.1 Introduction

Organic photovoltaics have seen a rapid increase in performance over recent years, with certain polymer:fullerene blends now attaining efficiencies of around 10%. This improvement has mainly been due to materials development. However, there is still a lack of key understanding of why certain acceptors work well only in combination with certain donors.[1] Moreover, small variations in the chemical structure of the active materials can lead to significant differences in device performance,[2-4] rendering materials design often to be intricate and cumbersome trial-and-error exercises.

One reason for these differences that are observed in devices even for very similar materials is that the manipulation of the chemical structure can (in the case of RR-P3HT) result in an alteration of the energy levels,[1, 5] which, in the case of the LUMO of the acceptor, should either promote charge dissociation or increase the open circuit voltage (V_{oc}) with a given donor. Chemical changes lead, however, also to a different miscibility of the two components, which can affect OPV device characteristics considerably.[6, 7] There is, hence, a strong drive to improve our understanding of the interplay of: solubility in a given solvent; mutual miscibility of the two components and their aggregation/crystallisation behaviour, on the final photo-physical properties of such donor:acceptor blends. More specifically, in-depth insights are required about the solubilities of donor and acceptor in a given solvent and how this influences the solidification of each material during solution casting and, indeed, the solidification sequence. This in turn strongly determines to what extent the materials can molecularly order and whether vitrification dominates solidification, which results in the formation of a kinetically trapped solid solution. If the materials crystallise –at least partly– during casting, knowledge has to be obtained whether coarse phase separation occurs, resulting often in the formation of large, relatively pure domains. Conversely, if miscibility of the components is high or ordering of at least one component is hindered, a single highly intermixed phase may be generated.

In order to address how these phenomena and resulting phase morphologies affect the processes relevant in photovoltaic devices, we selected donor:acceptor systems utilising three different C_{60} fullerene derivatives as the acceptor, namely, [6,6]-phenyl-C61-butyric acid methyl ester (PCBM), bis(1-[3-(methoxycarbonyl)propyl]-1-phenyl)-[6.6]C62 (bis-PCBM), 1',1'',4',4''-tetrahydro-di[1,4] methanonaphthaleno[5,6]fullerene-C60 (ICBA) (structures shown in Figure 5.1 A). These show significant promise in terms of both device performance[8, 9] and for scale-up of production. They also have different aggregation and crystallisation behaviour which should affect their miscibility with the donor. As the donor we chose for similar reasons to use a polymer with well understood and measureable crystallisation behaviour, *i.e*. poly(3-hexylthiophene-2,5-diyl) P3HT, with the highest molecular weight that was available, in this case "H-P3HT" (M_n=70, M_w=135 kg/mol) This allows for a clearer comparison of the effect of the respective fullerene on the formation of molecularly ordered domains within the polymer and the resulting fractions of mixed and pure phases that will be present in the final structure. Furthermore, P3HT, unlike many polymers shows distinct phase transitions observable during thermal analysis, thereby providing an additional tool to probe certain structural characteristics of such blends.

5.2 Results and discussion

We first set out to gain an initial understanding of the fullerene's influence on the structural formation of the polymer and, hence, the one of the corresponding blends, by studying the thermal behaviour of the selected H-P3HT:fullerene systems. To this end we measured the polymer's melting temperature as a function of fullerene content for blends spanning the entire composition range (Figure 5.1 B). We observe a clear melting point depression of the H-P3HT upon addition of either fullerene which means that the melting point of the polymer in a blend with a given fraction of the respective fullerene, T_m, is lower than the melting temperature of the neat polymer, T_m^0. Thereby, a

similar trend is found for all three systems. The similarity in melting point depression implies that the different fullerene:polymer blends display comparable Flory-Huggins interaction parameter (χ_{pf})

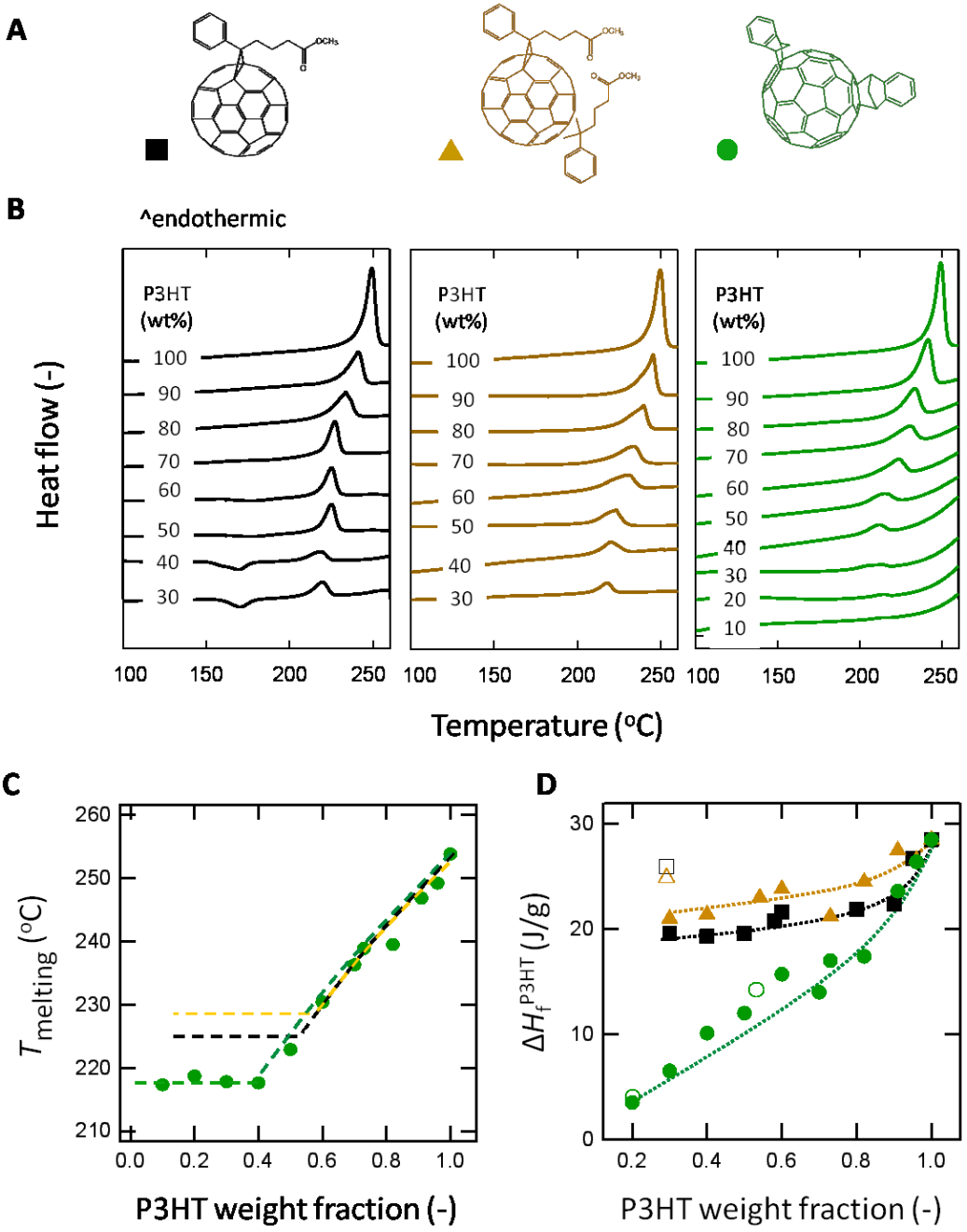


Figure 5.1: Thermal behaviour of three H-P3HT:fullerene blends, showing clear differences between the binaries systems. **A:** Chemical structures of the fullerenes investigated here: PCBM (left, squares), bis-PCBM (middle, triangles) and ICBA (right, circles). The same symbols are used for each fullerene throughout this chapter. **B:** Differential scanning calorimetry first heating thermograms (heating rate = 10 ^{o}C/min) of P3HT:fullerene binaries cast from solution and of a P3HT content as indicated: ICBA (left), bis-PCBM (middle) and PCBM (right). **C:** Non-equilibrium binary phase diagram deduced from the end-of melting of the various polymer:fullerene blends obtained in **B**. Overlaid lines are as a guide for the eye. **D:** Fusion endotherm of P3HT (ΔH_f^{P3HT}) as measured for the different binaries with ICBA (green), bis-PCBM (yellow) and PCBM (black). The ΔH_f^{P3HT} was extracted from the integral of the melting endotherm and normalised for the mass of polymer in the sample, thus, enabling comparison of the degree of crystallinity of the polymer in the different blends.

as deduced from the combination of Gibbs free energy change of melting and the Flory-Huggins solution theory[10] (Equation 5.1):

$$\frac{1}{T_m} - \frac{1}{T_m^0} = \frac{R}{\Delta H_f^{P3HT}} \left(\frac{v_p}{v_d}\right) (v_d - \chi_{pf} v_d^2) \qquad \textit{Equation 5.1}$$

where ν_d *is* the volume fraction of fullerene, R is the ideal gas constant, ΔH_f^{P3HT} is the enthalpy of fusion of the polymer, and v_p and v_d are the monomer volumes of the polymer (P3HT) and diluent (fullerene) respectively. This observation would imply that the miscibility of the three fullerenes with H-P3HT is comparable. Accordingly, one would expect similar amount of intermixed phases to be present within these blends. However, the opposite is observed: strong variations are found for the three systems with respect to the extent the different fullerenes quench the H-P3HT's photoluminescence (PL) — with the photoluminescence quenching (PLQ) giving a direct indication of the degree of molecular mixing of the two components (Figure 5.2). Indeed, while all blends exhibit increased quenching with fullerene content, those comprising bis-PCBM consistently display the highest PL emission (*i.e*. the lowest PLQ) across the entire composition range, while the lowest PL (highest PLQ) is observed for binaries comprising ICBA, with an interim behaviour found for PCBM-containing blends. This suggests that the presence of more intimately mixed phases are present in H-H-P3HT:ICBA- and H-P3HT:PCBM-blends compared to H-P3HT:bis-PCBM binaries despite the fact that the χ_{pf} seem to be comparable for the three systems.

The question arises what causes this observed discrepancy between our thermal analysis data (*i.e*. comparable χ_{pf} values of the three blends, indicating a similar miscibility between the selected fullerenes and P3HT) and the observed photoluminescence quenching of those systems. One obvious reason is that the solidification mechanisms between the three systems are drastically different. For instance, highly intermixed, quenched 'solid solutions', where a substantial fraction of

the polymer is frozen into a finely intermixed state with the fullerene, may form depending on the fullerene selected and blend composition, as has been shown for P3HT:PCBM binaries.[11]

The presence of such a highly intermixed solid solution observed in solution cast blends may be strongly influenced by vitrification during solution casting. The phenomenon of vitrification is essentially a trapping of the microstructure of system (comprised of one or more materials) and is achieved by bringing the system to a temperature or composition in the glassy regime. (*e.g*. by rapidly cooling a material to below the glass transition temperature, $T_{g,}$ or by rapid removal of a plasticizer, such as a solvent during solution casting). As the system is no longer able to freely reorganise, the microstructure attained at the point of vitrification will be retained, even if it is not the thermodynamically most favourable state, hence resulting in kinetic trapping of the structure. For this reason we consider vitrification in the context of a polymer:fullerene:solvent ternary blend, where the interplay between plasticizing effect of the solvent and the reported vitrifying effect of fullerene may strongly influence the polymers ability to order and hence the microstructure that is formed.[11] It is worthwhile to note that by changing the chemical structure of the fullerene employed, the T_g of the fullerene may also alter.

To investigate whether the H-P3HT had ordered to different extents within the solution cast binaries, we measured the integral of the melting peak ascribed to H-P3HT within the various blends (Figure 5.1 D), which is directly correlated to the polymer's degree of crystallinity and, hence, gives an indication how strongly a given fullerene hinders its crystallisation. Thereby, lower integral signifies a stronger vitrifying effect of the acceptor on the polymer. The relative degree is crystallinity (rDoC) is calculated via Equation 5.2:

$$\mathrm{rDoC} = \frac{\Delta H\mathrm{f\ P3HT\ (blend)}}{\Delta H\mathrm{fP3HT\ (P3HT)}} \qquad \textit{Equation 5.2}$$

where ΔH_f^{P3HT} (blend) and ΔH_f^{P3HT} (P3HT) are the enthalpy of melting for the blend and neat material respectively.

Table 5.1: A table showing the melting enthalpies of P3HT when blended with the three different fullerenes at two compositions. All values are normalised to the measured melting of neat P3HT (28.9 J/g) to yield the relative degree of crystallininity (rDoC).

H-P3HT:fullerene (weight ratio)	**H-P3HT:ICBA**	**H-P3HT:PCBM**	**H-P3HT:bis-PCBM**
60:40	0.55	0.76	0.84
30:70	0.23	0.68	0.74

For all three systems, there is a clear reduction in rDoC with increasing fullerene loading, supporting this previously forwarded picture that fullerenes can act as vitrifier for H-P3HT. The lowest rDoC is consistently observed for ICBA blends, followed by binaries comprising PCBM, with bis-PCBM containing systems always exhibiting the highest rDoC. A summary of the degree of crystallinity of the polymer within the blend relative to neat P3HT are displayed in Table 5.1. All blends retain, though, a certain crystalline fraction of the polymer even at high content of the fullerenes.

Based on these data we suggest a structural picture where the polymer can crystallise to the greatest extent in the binary comprising bis-PCBM, which results in more prominent phase separation with H-P3HT and, hence, the lowest amount of PL quenching. At the other side of the spectrum are the ICBA-containing blends; ICBA acts as the strongest vitrifier, inhibiting the crystallisation of P3HT during the casting process most, in agreement with our PLQ data.

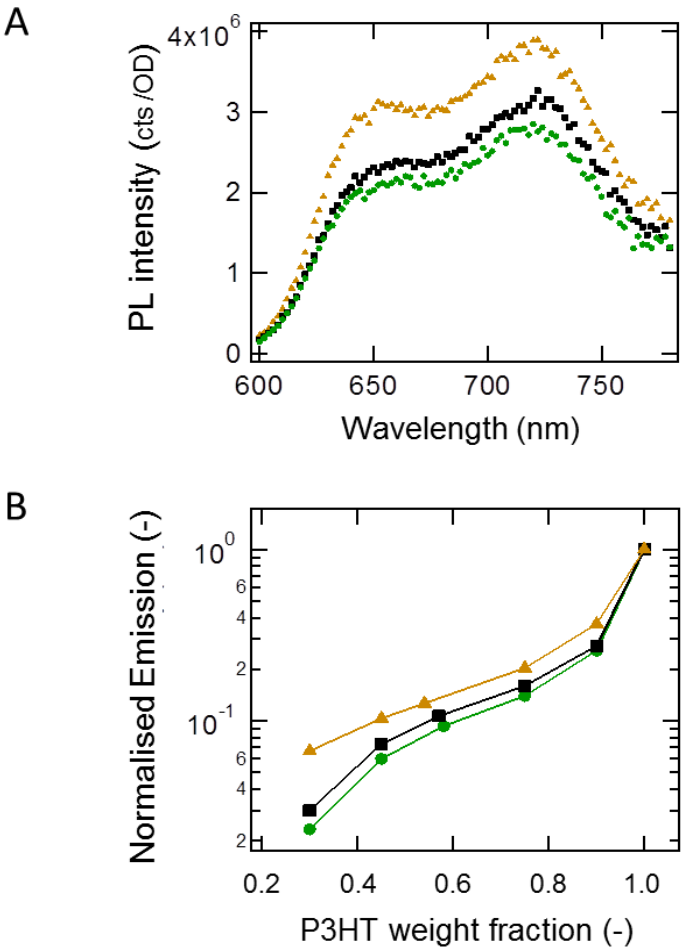


Figure 5.2: PL emission characteristics of pristine solution-cast P3HT:fullerene blends, showing clear differences in emission intensity. **A:** Corrected emission of blends comprising ~55 wt% P3HT and: ICBA (green circles), bis-PCBM (orange triangles) and PCBM (black squares) respectively (corresponding to the optimised OPV devices discussed subsequently). **B:** Normalised PL intensity of the different blends plotted as a function of composition. All data has been corrected for differences in number of absorbed photons at the excitation wavelength of 520 nm and normalised to the emission of neat P3HT.

Note in this context that these H-P3HT:ICBA solid solutions that form upon blending seemed to be rather stable. For instance, annealing H-P3HT:ICBA blends (30:70 weight ratio) at 165 °C for 1 hour did not lead to any increase in rDoC (Figure 5.1 D, open circles). In strong contrast, for H-P3HT:PCBM and P3HT:bis-PCBM binaries, an increase in the rDoC is recorded during an identical heat treatment. In the case of the H-P3HT:PCBM blend micron sized fullerene crystals (similar to those displayed in Figure 4.6 bottom) are observed. These observations, in conjunction with the found, higher values for rDoC

(open squares and triangles) suggest that the quenched amorphous solution is less stable in these systems containing PCBM and bis-PCBM.

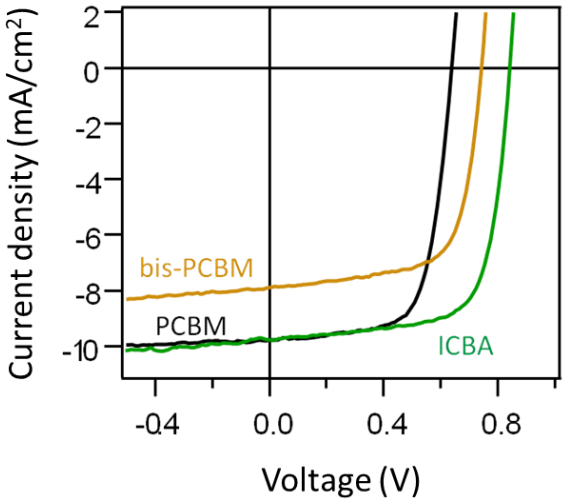


Figure 5.3: *J-V* characteristics of H-P3HT:fullerene devices optimised for thickness and composition (P3HT content: ~55 wt %) after annealing at 165 °C for 7 minutes.

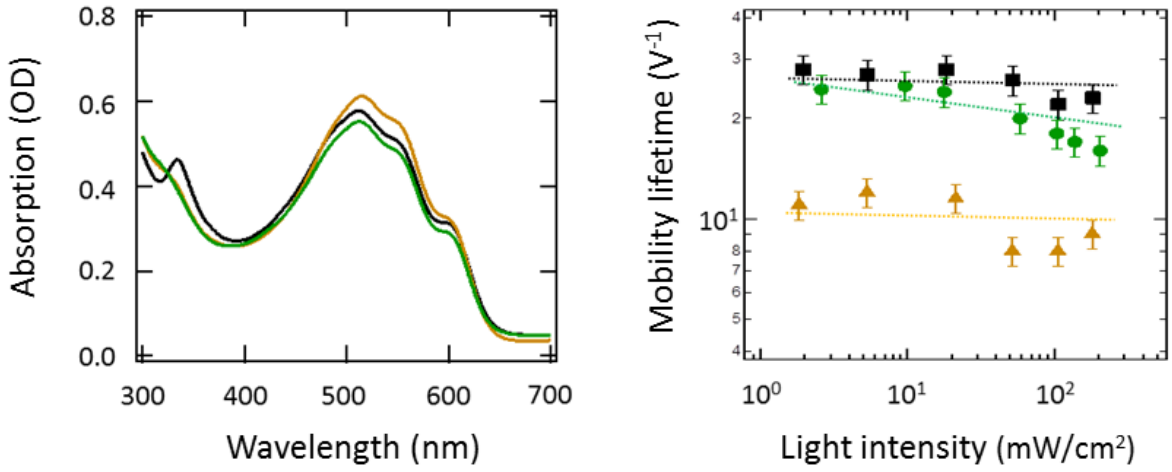


Figure 5.4: Optoelectronic features of H-P3HT:fullerene blends (P3HT content: ~55 wt %). **Left**: Absorption spectra of P3HT:fullerene blends prepared under the same conditions as those used for OPV devices, showing similar absorption profiles for all three systems. **Right**: Hecht Analysis for devices made with such P3HT:fullerene blends showing the mobility-lifetime product as a function of light intensity for systems comprising PCBM (black squares), ICBA (green circles) and bis-PCBM (orange triangles). All devices appear to exhibit relatively independent mobility lifetime as a function of light intensity.

Intriguingly, the different tendencies towards vitrification of the various blends seem to correlate with the J_{sc} of OPV devices fabricated with them (~55 wt % H-P3HT; Figure 5.3). The differences in Voc are ascribed to the subsequently higher LUMOs of PCBM, bis-PCBM and ICBA as reported previously.[8, 9] The highest J_{sc} is observed for the blends comprising the greatest fraction of solid solution (H-P3HT:ICBA and H-P3HT:PCBM), compared to the more prominently phase-separated P3HT:bis-PCBM binary. Since the three systems had similar absorption profiles (Figure 5.4, left) we can eliminate differences in number of absorbed photons as the origin of this difference in J_{sc}.

To investigate the photophysical origin of the differences in photo-collected charge efficiency for the different blends, the mobility-lifetime product was used as a tool to probe the recombination mechanism. The mobility-lifetime is the average free charge carrier mobility (of both holes and electrons) multiplied by the lifetime of these free charge carriers, and hence relates to the probability of collecting these carriers.[12] It can be modelled from the shape of the *JV* curve of an OPV device. If the free charge generation is linear with the incident light intensity, the light intensity can be used as a tool to effectively vary the number of free charge carriers generated within the device, thus enabling the effects of charge carrier concentration to be probed. If the mobility-lifetime is independent of light intensity (and hence carrier concentration) then the recombination mechanism is ascribed as mono-molecular, whereas if the mobility lifetime product reduces with increasing light intensity then a greater tendency towards bimolecular recombination is ascribed.[12]

The mobility-lifetime was therefore used to assess whether the differences in vitrification/microstructure affected recombination processes in the corresponding active layers (Figure 5.4, right). Across the light intensities probed, all three systems exhibited generally mono-molecular recombination characteristics, implying a similar recombination mechanism in all cases. This is significant as it indicates that even with drastically varied fractions of finely intermixed and crystalline material, recombination mechanism in all cases appears comparable for all the

P3HT:fullerene systems investigated. Based on our observations we attribute the difference in J_{sc} of the devices to a change in conversion of the absorbed photons into free charge carriers. For the systems where smaller fractions of intermixed solid solution co-exist with phase-pure polymer (deduced from rDoC) and likely phase-pure fullerene domains, less charges are generated supporting the picture that exciton dissociation occurs in finely intermixed phases as long as minority fractions of a phase pure donor and/or acceptor are present.[13, 14] In agreement with this model is also the fact that we observe modest increase in fill factor of 0.66, 0.67 and 0.70 when changing the fullerene from bis-PCBM, PCBM and ICBA, respectively. This indicates more bias-independent charge collection efficiency in the systems containing higher intermixed fractions.

This structural picture is further corroborated by grazing-angle incidence wide-angle X-ray scattering (GIWAXS) (Figure 5.5), whereby the 2D scattering plots solution-cast blends of H-P3HT:fullerene (annealed for 7 minutes, 165 ^{o}C) are displayed (Figure 5.5. A) for compositions of 30 and ~55 wt% of P3HT. Within these blends the lamellar reflections of P3HT (labelled (100), (200) and (300) in Figure 5.5 A, centre-top panel), are seen to differ in intensity depending on both the composition and fullerene present. The intensity of these peaks is related to the rDoC of the P3HT, and thereby gives an indicator of how much of the P3HT is ordered within the different samples. Line plots (Figure 5.5. B) are taken through the centre of the lamellar reflections (*i.e.* a vertical line, at Q_{xy} =0) and clearly show the blends comprising the higher P3HT composition have more intense lamellar reflections, implying a higher rDoC, which is concurrent with our DSC measurements. Interestingly the PCBM and ICBA samples are comparable in both compositions, whereas in both cases the blends with bis-PCBM exhibit more intense lamellar reflections, indicative of a higher rDoC of P3HT.

Clearly, in the binary blends investigated here, there appears to be a delicate balance between the amount of solid solution and the more phase-pure fractions. The systems that constitute the largest amount of intermixed fraction in conjunction with phase-pure domains (PCBM- and ICBA-

comprising blends), more efficiently collect photo-generated charge. In contrast, the system where more pronounced phase separation occurs (H-P3HT:bis-PCBM blends) shows a lower short-circuit current, which we attribute to the lower charge generation and collection efficiency.

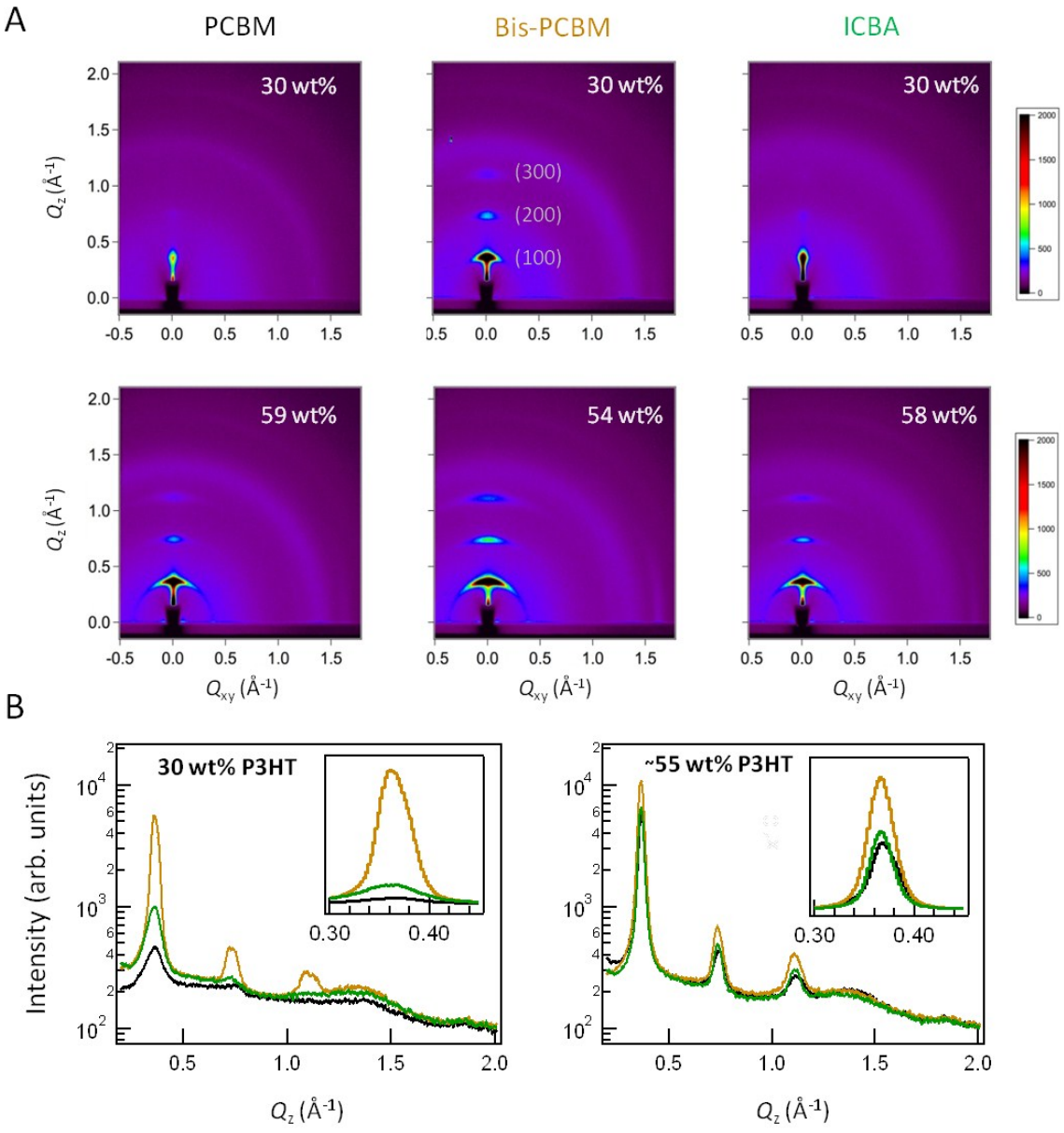


Figure 5.5: GIWAXS data obtained for H-P3HT:fullerene blends (P3HT composition shown inset) annealed at 165 °C, for 7 minutes. **A:** 2D-scattering patterns of blends comprising 30 wt% (top) and ~55 wt% (bottom, corresponding the most efficient OPV devices fabricated with each fullerene) P3HT and, respectively, PCBM, bis-PCBM and ICBA. For reference, the positions of the lamellar reflections have been labelled in the middle graph. **B:** Scattering intensity of the Q_z (vertical) line plot taken from the 2D images shown in A. Systems of a 30 (left) and ~55 (right) wt% of H-P3HT; blended with PCBM (black), bis-PCBM (orange) and ICBA (green). Inset shows the (100) diffraction on a linear scale to aid comparison.

This latter picture is consistent with data we obtain on H-P3HT/fullerene bilayers where the vitrification of the polymer is limited because in the absence of the fullerene the polymer can molecularly order and aggregate first as a neat polymer film is cast, which is then laminated onto a fullerene layer. The fullerene diffuses into the pre-aggregated polymer at various temperatures, after annealing for 30 s, (Figure 5.6 A), with all fullerene exhibiting a clear increase in intermixed quantity with increasing temperature. Additionally, it appears that when the quantity of fullerene that has diffused into the polymer is plotted against the intensity of the PL (Figure 5.6 B) that all systems appear to collapse onto a similar curve. Since the polymer was able to order prior to introduction of the fullerene it may suggest that in the case of the bilayer samples, it is the quantity of the fullerene that is present within the polymer layer that dictates the PLQ.

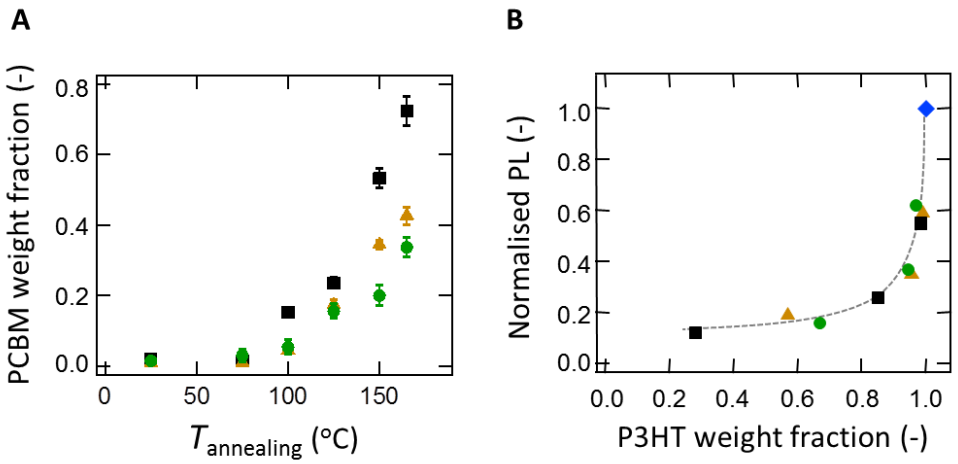


Figure 5.6: Evolution of the structural and optoelectronic properties of P3HT/fullerene bilayers. **A:** Evolution of fullerene content in the polymer layer after annealing for 30 s at a given temperature, as deduced from D-SIMS profiles and calibration curves. **B:** Normalised PL values for the different bilayers after annealing: H-P3HT/PCBM (black squares), H-P3HT/ICBA (green circles) and H-P3HT/bis-PCBM (orange triangles) plotted against fullerene content within the P3HT layer.

5.3 Conclusions

In conclusion, it is clear that while the fullerenes investigated here exhibit relatively similar miscibilities as deduced from DSC and D-SIMS, drastic differences in the degree of vitrification of the

donor polymer upon solution casting with these fullerenes was observed. The vitrification can lead to the formation of a kinetically trapped solid solution, which has significant influence on optoelectronic processes within the blend. In systems where a kinetically trapped solid solution was present, the most efficient PLQ – *i.e.* highest exciton dissociation – was observed. It is important to note, though, that thermal analysis confirms that even for blends comprising ICBA, phase pure P3HT regions co-exist, leading to efficient charge extraction. In systems with the most prominent phase separation, the least efficient PLQ and lower short circuit current were observed.

Our results highlight the governing influence of fullerene-induced vitrification and emphasize the delicate balance of phases required for most efficient device performance. The effects of vitrification during solution casting could be observed to persist even after thermal annealing, highlighting the importance of the processing memory during solution casting on the final microstructure and, terminally, device performance. These findings may help answering the questions related to why certain fullerenes do not make efficient solar cells with some polymers, or at certain blend ratios. They also give insights why many of the more rigid polymer currently used in OPVs (*e.g.* thieno[3,2-b]thiophene-diketopyrrolopryrrole containing polymers) typically require larger fractions of fullerene for realising optimum device performance.

5.4 Materials and methods

Bilayer fabrication: Bilayers were fabricated via spin-coating fullerene (30 mg/ml) onto a pre-cleaned substrate at 1000 rpm for 60 s. This film was then stored under vacuum for two days to aid removal of residual solvent. Polystyrene sulphonate (PSS) was spin-coated onto a different substrate (8 mg/ml in deionised water) at 3000 rpm for 45 s and subsequently dried under vacuum for 1 day. On top of this layer, P3HT (15 mg/ml in chlorobenzene) was spin-coated at 1200 rpm for 45 s, followed by 2000 rpm for 7 s. This stack was then dried under vacuum for two days. Following

drying, the P3HT film was delaminated and floated onto a bath of water where it was picked up using the PCBM-covered substrate. The bilayers were dried under vacuum for a subsequent 2 days to remove any residual water. Samples were then annealed in the dark for 30 s at the temperatures indicated in the main text and rapidly cooled on an ambient metal block. Further preparation of D-SIMS samples was carried out as previously reported (chapter 4). Optical samples were prepared on glass substrates, and D-SIMS samples on SiO_2.Thermal annealing of samples (as indicated in the main text with annealing temperature) was carried out for 30 s under nitrogen.

Blend fabrication: Blend samples were prepared by dissolving the appropriate polymer:fullerene ratio (20 mg/ml total mass) in chlorobenzene to which 1.5 vol% chloronaphthalene was added. Spin-coating was carried out at 1200 rpm for 45 s, followed by 2000 rpm for 7 s. Optical samples were prepared on glass; GIWAXS samples on silicon wafer and OPV devices on ITO glass as discussed below. Samples that were thermally annealed (as indicated in the main text) were heated at 165 ^{o}C for 7 minutes under nitrogen.

Grazing-angle incidence wide-angle x-ray scattering (GIWAXS): measurements were carried out at Beamline 7.3.3. of the Advanced Light Source using a Dectris Pilatus 1M photon counting detector. Samples were measured at an incident angle of ~0.13^{o}, above the critical angle so the X-ray beam penetrated to the substrate. The photon energy used for GIWAXS was 10 keV. Air scatter which provides a background signal was reduced using helium gas.

Device Fabrication: Glass substrates coated with ITO were cleaned in acetone in an ultrasonic bath, followed by sequential washing in deionised water comprising 2 vol% soap, deionised water and isopropyl alcohol for 20 minutes each, followed by drying with nitrogen. A 40 nm layer of poly(3,4-ethylenedioxythiophene):poly(styrenesulfonate) (PEDOT:PSS) (Clevios PVP Al 4083) was coated via spin-coating at 4000 rpm, 40 s and then dried on a hotplate at 165 °C for 10 min. P3HT:fullerene blend solutions were subsequently deposited as described above. Solution concentration was varied between 19-23 mg/ml to vary the thickness of the active layer and blend

ratios between (1:1 and 1:0.7, polymer:fullerene by weight). The electrodes were then evaporated under vacuum (<10^{-6} Torr). Samarium was typically evaporated at around 0.7 Å/s, until a thickness of 15 nm was attained. Aluminium was typically evaporated at around 3 Å/s, until a layer around 75 nm thick was attained. Each substrate contained 5 solar cells each of which had an area of 0.06 cm^2. *J-V* characteristics of the devices were measured at 1 sun (AM 1.5G) under a nitrogen atmosphere. A Xenon lamp (Newport) and Keithley 2408 SMU were utilised for the measurement. The light intensity dependant *J-V* characteristics were measured using an array of 14 red 1 W LEDs under nitrogen. Light and dark measurements were measured sequentially using a Keithley 2400 source meter unit. As previously reported V_{oc} of around 0.64, 0.74 and 0.84 V were observed for PCBM, bis-PCBM and ICBA respectively, due the successively higher LUMOs these materials.

*Differential scanning calorimetry: w*as carried out on films that had been dried under vacuum for 4 days to remove residual solvent. Drop cast films were scratched from the substrate and placed into a DSC pan. Heating was carried out at 10 °C/min over a temperature regime of 40-270 °C under a nitrogen atmosphere, utilising a Mettler Toledo DSC822. Phase diagrams were constructed from the end-of-melting temperature.

UV-vis, PL and SIMS: were carried out as reported in chapter 4.

5.5 References

1. M. A. Faist, S. Shoaee, S. Tuladhar, G. F. A. Dibb, S. Foster, W. Gong, T. Kirchartz, D. D. C. Bradley, J. R. Durrant and J. Nelson, *Advanced Energy Materials*, 2013, **3**, 744-752.
2. P. A. Troshin, H. Hoppe, J. Renz, M. Egginger, J. Y. Mayorova, A. E. Goryachev, A. S. Peregudov, R. N. Lyubovskaya, G. Gobsch, N. S. Sariciftci and V. F. Razumov, *Advanced Functional Materials*, 2009, **19**, 779-788.
3. C. M. Amb, S. Chen, K. R. Graham, J. Subbiah, C. E. Small, F. So and J. R. Reynolds, *Journal of the American Chemical Society*, 2011, **133**, 10062-10065.

4. Z. Fei, M. Shahid, N. Yaacobi-Gross, S. Rossbauer, H. Zhong, S. E. Watkins, T. D. Anthopoulos and M. Heeney, *Chemical Communications*, 2012, **48**, 11130-11132.
5. A. A. Y. Guilbert, L. X. Reynolds, A. Bruno, A. MacLachlan, S. P. King, M. A. Faist, E. Pires, J. E. Macdonald, N. Stingelin, S. A. Haque and J. Nelson, *ACS Nano*, 2012, **6**, 3868-3875.
6. N. D. Treat, A. Varotto, C. J. Takacs, N. Batara, M. Al-Hashimi, M. J. Heeney, A. J. Heeger, F. Wudl, C. J. Hawker and M. L. Chabinyc, *Journal of the American Chemical Society*, 2012, **134**, 15869-15879.
7. B. A. Collins, Z. Li, C. R. McNeill and H. Ade, *Macromolecules*, 2011, **44**, 9747-9751.
8. M. Lenes, G.-J. A. H. Wetzelaer, F. B. Kooistra, S. C. Veenstra, J. C. Hummelen and P. W. M. Blom, *Advanced Materials*, 2008, **20**, 2116-2119.
9. Y. He, H.-Y. Chen, J. Hou and Y. Li, *Journal of the American Chemical Society*, 2010, **132**, 1377-1382.
10. P. J. Flory, *The Principles of Polymer Chemistry*, Cornell University Press, New York, 1953, ch. 13, pp. 563-571.
11. Y. Kim, S. A. Choulis, J. Nelson, D. D. C. Bradley, S. Cook and J. R. Durrant, *Journal of Materials Science*, 2005, **40**, 1371-1376.
12. R. A. Street, M. Schoendorf, A. Roy and J. H. Lee, *Physical Review B*, 2010, **81**, 205307-205307.
13. F. C. Jamieson, E. B. Domingo, T. McCarthy-Ward, M. Heeney, N. Stingelin and J. R. Durrant, *Chemical Science*, 2012, 485-492.
14. E. Buchaca Domingo, A. J. Ferguson, F. Jamieson, T. McCarthy-Ward, S. Shoaee, J. R. Tumbleston, O. G. Reid, L. Yu, M.-B. Madec, M. Pfannmöller, F. Hermerschmidt, R. R. Schröder, S. E. Watkins, N. Kopidakis, G. Portale, A. Amassian, M. Heeney, H. Ade, G. Rumbles, J. Durrant and N. Stingelin, *Materials Horizons*, 2013, DOI:10.1039/C1033MH00125C.

Chapter 6

Molecular-weight dependence on structural formation in conjugated polymer-polymer systems

6.1 Introduction

Polymer:polymer photovoltaics (PP-PVs) feature, in principle, a number of potential benefits when compared to polymer:fullerene systems. Firstly, it is generally easier to tailor the energy levels, and, hence, bandgap of polymers when compared to fullerenes, allowing for a greater tunability of their optoelectronic characteristics.[1] Secondly, the absorption coefficients of polymers are typically significantly higher than those of fullerenes, especially of those of the commercially available C_{60} derivatives.[2] Hence, more photons should be captured in polymer:polymer active layers. In addition certain fullerenes, such as PCBM(C60), are capable of macroscopically phase separating into large crystals over time, which was shown in chapter 4 to impact charge generation and to potentially be highly detrimental for the long-term stability of such devices. Furthermore, the rheological properties of polymer:polymer solutions may be more readily be manipulated than those containing polymer:small molecules; an aspect that will be critical if organic photovoltaics (OPVs) shall be produced in high-throughput fashion.

Despite the various potential benefits of PP-PVs, their performance has for a long time trailed behind that of polymer:fullerene devices in terms of power conversion efficiency. While typical systems can yield similar or higher V_{oc} to polymer:fullerene blends, the device performance is often limited by poor fill factor (FF), short circuit current (J_{sc}) or both.[1, 3, 4] These two attributes are intricately linked with the microstructure of the OPV active layer; the poor FF and J_{sc} has therefore been linked to the increased sensitivity of polymer-polymer blends to variations in processing, partly due to the greater tendency of macromolecular binaries to liquid-liquid phase separate.[5] Moreover, the effect of aggregation of the active, macromolecular components in solution on the final microstructure and phase morphology, and hence device performance needs to be further elucidated.[6]

Nonetheless, there have been dramatic improvements in the performance of PP-PVs recently,[1] with efficiencies increasing from just over 2%[7] to 6.4% (certified) in a few years. This

development has, in large part, been due to work by Polyera Corp., and suggests that the challenges faced by PP-PV are by no means unsurpassable. However, in order to further accelerate this evolution, more comprehensive understanding of the properties leading to microstructural formation of polymer:polymer active layers and the establishment of key structure/property/processing inter-relationships are required.

In this chapter focus is given to the effects of molecular weight of the donor and acceptor polymer on the resulting microstructure, the molecular weight is an intrinsic yet tuneable property of macromolecules that can be varied without changing the chemical nature of the individual moieties and can be expected to have an effect on a number of properties of such systems, including: crystallisation,[8-11] molecular diffusivity[12] and tendency to liquid-liquid phase separate.[5] Such changes in structural formation processes may result in different microstructures and phase morphologies, resulting in differing photo-physical behaviour.

Poly(3-hexylthiophene-2,5-diyl) (P3HT) and poly(3-hexylselenophene-2,5-diyl) (P3HS) were selected here as model systems, as they possess a number of valuable attributes. Firstly, the effect of weight-average molecular weight (M_w) on the microstructure of neat P3HT has been extensively studied[11, 13] and its entanglement threshold was identified. Furthermore, both materials are available in relatively similar molecular weights, produced via comparable synthetic routes, thereby allowing valid comparisons to be drawn. In addition, P3HT and P3HS are capable of at least partly crystallising, with the two polymers having discernibly different crystal lattices (see chapter 7), enabling a more comprehensive investigation into the nature of phases present in blend films. Furthermore, the difference in heteroatom (S *vs.* Se) permits differentiating the two polymers with depth profile secondary ion mass spectrometry (D-SIMS). The heteroatom also affects the LUMO level of the polymer,[14] whereby in the case of P3HS the LUMO is more stable (hence lower, leading to a smaller bandgap), due to the enhanced stabilisation of the LUMO provided by the Se atom relative to the S atom. This difference in the LUMO levels may also provide an interesting system

through which to study the processes occurring after photo-excitation. For example, after initial photo-excitation of the wider bandgap P3HT, it is feasible that a charge transfer event (*c.f.* P3HT-PCBM) may occur. A further interesting possibility would be that the exciton could be transferred to the lower bandgap material via an energy transfer process. The potential of this system to explore such sensitive photophysical processes provides further rational for its investigation. More discussion of the photophysical properties of such system are discussed in Chapter 7.

The intermixing of polymer binaries from bilayers structures provides a valuable route to investigate both the thermodynamics of mixing and the kinetics of macromolecular diffusion within different regimes. The thermodynamic interaction of the two materials can be investigated through use of the Flory-Huggins solution theory for two macromolecular species:[5]

$$\Delta G = RT\left[\left(\frac{\emptyset_{P3HT}}{N_{P3HT}}\right) ln\emptyset_{P3HT} + \left(\frac{\emptyset_{P3HS}}{N_{P3HS}}\right) ln\emptyset_{P3HS} + \chi_{P3HT-P3HS}\emptyset_{P3HT}\emptyset_{P3HS}\right]$$

Equation 6.1

where Δ*G* is the Gibbs free energy of mixing, *R* is the gas constant, *T* is the temperature, $\emptyset_{P3HT}$ and are $\emptyset_{P3HS}$ are the volume fractions of P3HT and P3HS respectively, N_{P3HT} and N_{P3HS} are the number of lattice sites occupied by a polymer chain and $\chi_{P3HT-P3HS}$ is the Flory-Huggins interaction parameter for the two materials. To better visualise the entropic and enthalpic contributions to the free energy as how this may affect the mixing behaviour of the two materials we can consider the components separately, the two entropic terms, *e.g.*

$$\left(\frac{\emptyset_{P3HT}}{N_{P3HT}}\right) ln\emptyset_{P3HT}$$

and the P3HS equivalent, are dependent upon the molecular-weight of the polymer (which is directly proportional to *N*), whereby increasing the molecular-weight will reduce the entropic benefit

of mixing. It is worthwhile to note here that the polydispersity of the polymers needs to be considered, when interpreting the above description of solution theory, which assumes that all polymer chains are the same length (*i.e.* a PDI of 1). In terms of the enthalpic contribution, the interaction parameter, $\chi_{P3HT-P3HS}$, is a monomeric quantity, which can in theory be either positive or negative and of varied magnitude, due to the structural similarity of the two monomers, one possibility is that the interaction parameter may be close to zero.

In terms of the kinetics of diffusion, the molecular weight of the polymers can have a substantial influence on the diffusion behaviour. For example, in the case of the low molecular weight polymers (below the entanglement threshold), diffusion is generally considered to occur via the Rouse model.[15] Whereby, the unentangled polymer chains slide past each other as if in a viscous medium. The rate at which occurs is related both to the molecular-weight of the polymer and also the monomeric "stickiness", termed the monomeric friction factor. Resulting in an inverse proportionality between the diffusivity (D_{Rouse}) and molecular volume (N):

$$D_{Rouse} \sim N^{-1}$$

In the case of the polymer chains above the entanglement threshold, the reptation model, as proposed by deGennes, is typically used to explain polymer diffusion.[12] This model considers the entangled polymer chain to move similarly to a Rouse chain but through a virtual tube as opposed to a viscous medium. This tube is influenced by the density of constraints (*e.g.* entanglements), which the virtual tube has to avoid, hence an increase in the entanglement density will provide a density number of constraints, past which the tube needs to meander. The diffusivity in the reptation regime can be considered inversely proportional to the square of the molecular volume in that:

$$D_{Reptation} \sim N^{-2}$$

6.2 Results and discussion

In order to focus on the interactions between the two polymers, we prepared P3HT/P3HS bilayers, building on the work described in the previous two chapters, and assessed the vertical distribution via D-SIMS. The weight-average molecular weights, M_w, for the selected P3HT and P3HS encompass a broad range from 7 to 100 kg/mol. For both P3HT and P3HS, a low and high molecular weight material were investigated (L-P3HT, H-P3HT, L-P3HS, H-P3HS). The low molecular weight materials (L-P3HT, L-P3HS) were chosen such that their chain lengths were sufficiently small for the molecules to adopt a non-entangled/chain-extended structure, while the higher molecular weight materials (H-P3HT, H-P3HS) were selected such that entanglements and tie-molecules[11] are present. Since previous calculations have highlighted that P3HS has a noticeably reduced backbone flexibility compared to P3HT,[16, 17] we expected the entanglement threshold for P3HS, *i.e*. the molecular weight at which first chain entanglements occur, for this polymer to be higher than for P3HT. Thus, a P3HS of higher molecular weight was selected to enhance the probability of chain entanglements. The number-average molecular weight (M_n), weight-average molecular weight and polydispersity index (PDI) are summarised in Figure 6.1 and Table 6.1. [NB. In the rest of this chapter the "L" and "H" prefixes denote the lower and higher M_w-samples of either material, respectively.] The molar mass distributions (as deduced from GPC measurements, Figure 6.1) give a clear indicator of the range of molar masses that are present within each of the materials. These samples appear to exhibit two trends with respect to their molar mass distribution, firstly it appears that as the M_n of the polymer increases, so does the absolute width of the distribution, with the H-P3HT (highest M_n) exhibiting the widest range of chain lengths. This is important as it highlights that even the high molecular weight polymer can still incorporate a significant fraction of polymer chains of substantially lower molar mass. The second observation to be made is that all distributions have a significant positive skew, resulting in a high molecular-weight "tail". It is worth highlighting here that as GPC is a technique that works differentiating molecules based on their size. This means that the in the case of polymers

with similar monomer size (*i.e.* P3HT and P3HS) that the reported values should be interpreted with caution, as the GPC will not take into account the difference in monomeric mass inparted by the heteroatom. As such, it may be prudent to interpret the GPC results as a relative measure of the degree of polymerisation of the two materials (hence, in this case not correcting for the monomer mass difference).

Table 6.1: Overview of number-average molecular weight (M_n), weight-average molecular weight (M_w), and polydispersity index (PDI) of the materials used in this chapter.

Material	M_n (kg/mol)	M_w (kg/mol)	**PDI** (-)
L-P3HT	5.1	7.2	1.4
H-P3HT	26	48	1.9
L-P3HS	8.3	16	1.9
H-P3HS	52	100	1.9

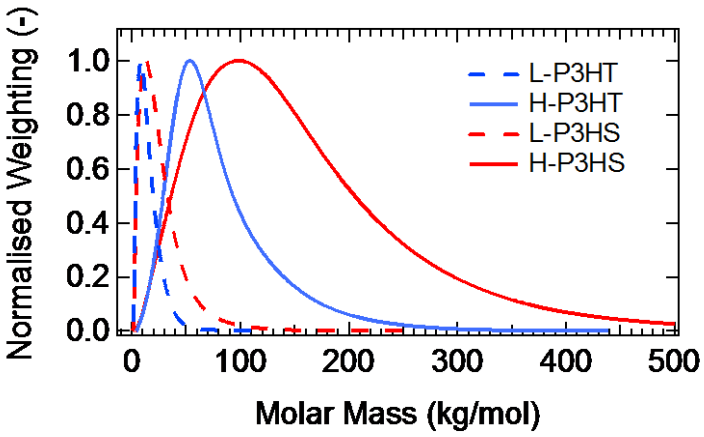


Figure 6.1: Molar mass distribution of the four materials investigated, as deduced by gel permeation chromatography (GPC) in chlorobenzene, and calibrated against polystyrene standards. It is important to highlight that these profiles are normalised to the maximum, not the integral, to aid visualisation of the large dispersion of molar masses present.

The molecular-weight dependence of intermixing of P3HT/P3HS bilayer structures was investigated using dynamic secondary ion mass spectrometry. Thereby, the depth profile was recorded of the pristine and annealed bilayers (see, Figure 6.2). The pristine bilayers of systems

containing a high molecular-weight material (Figure 6.2, bottom left/top and bottom right: open circles) exhibit distinct two layer structures, with a sharp change in signal at the central interface. In strong contrast, in the case of the low-M_w material pair (L-P3HT/L-P3HS) (Figure 6.2, top left: open circles), a small fraction of L-P3HS interdiffuses into the lower molecular weight P3HT layer, corresponding to around ~2% neat intensity. In fact, the Se-trace is flat within the L-P3HT region, implying that diffusion equilibrium has been attained. This suggests that the L-P3HS has significant mobility and tendency to mix into L-P3HT even at ambient temperatures.

Upon annealing at 190 °C for 70 hours all samples displayed some degree of intermixing (see filled symbols in Figure 6.2; Table 6.2 moreover summarises the amount interdiffused material in the various systems). It is clear that the most diffusion occurs between the two low molecular weight species. The L-P3HT/L-P3HS structures show complete loss of vertical contrast between the $^{34}S^-$- and $^{78}Se^-$-traces, characteristic of full vertical mixing. The H-P3HT/L-P3HS displays a flat two-layer profile, implying diffusion had come to equilibrium. However, it is also evident from our data that when exchanging L-P3HT with H-P3HT results in a considerable reduction of intermixing with L-P3HS from 50 to 16%.

An interim behaviour is observed for when the molecular weight of the P3HS is increased. L-P3HT/H-P3HS structures display a more complex diffusion behaviour. A relatively broad L-P3HT/H-P3HS interface develops after annealing due to partial interdiffusion (28% L-P3HT into H-P3HS; 25% H-P3HS into L-P3HT). In addition, an accumulation of H-P3HS at the air interface occurs as deduced from the enhanced ($^{78}Se^-$) signal at the top interface.

As expected, and in strong contrast to the other systems, H-P3HT/H-P3HS structures show little interdiffusion even after the used, prolonged temperature treatment. This can be deduced from the modest rise in intermixed signals in either layer: 3% of H-P3HT diffuses into H-P3HS layer compared to 16% when L-P3HS is used. 1% of H-P3HS interdiffuses into H-P3HT layer, compared to 18% when L-P3HS is used. The diffusion between these high molecular materials is likely influenced

by the substantial polydispersity within these samples and due to the shorter chains within each material, which would be expected to have both higher diffusivity and also a greater thermodynamics tendency to mix.[12, 5]

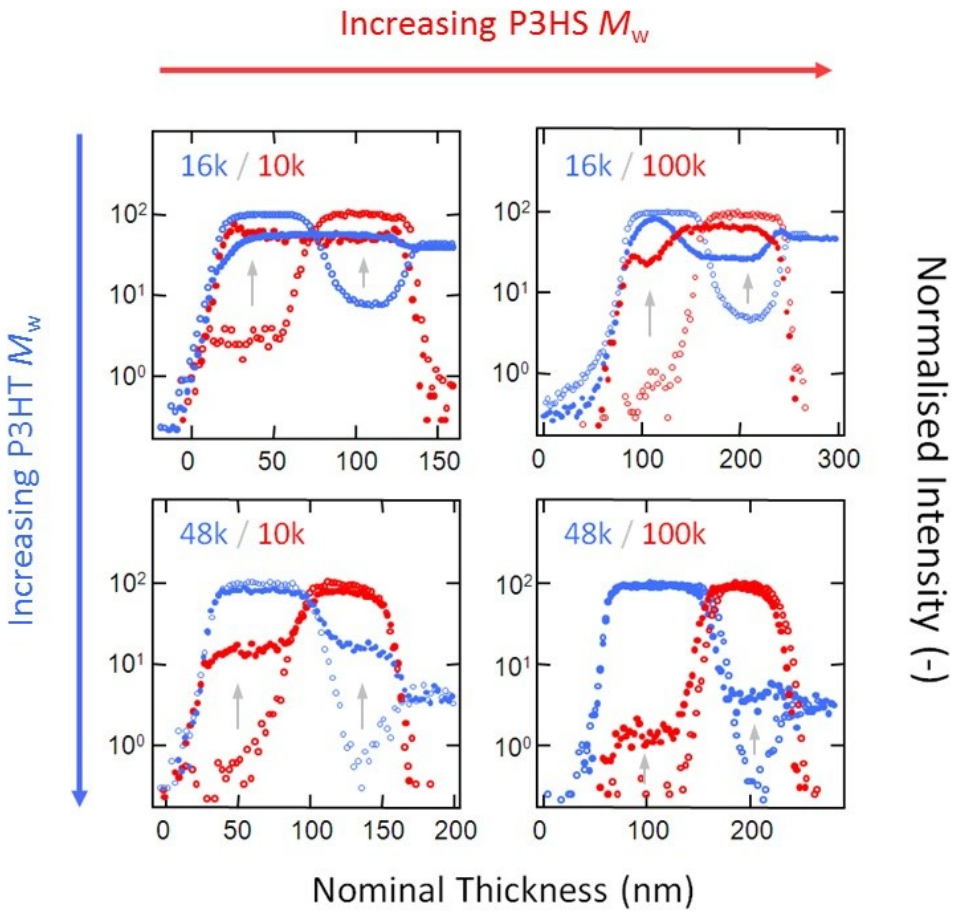


Figure 6.2: The molecular-weight dependence of intermixing of P3HT/P3HS bilayers as probed by D-SIMS: pristine bilayers (open circles) and annealed at 190 °C for 70 hours (filled circles). $^{34}S^-$-(blue) and $^{78}Se^-$ -traces (red) are shown allowing identification of the P3HT and P3HS, respectively. The inset labels give the M_w of the P3HT and P3HS used in the respective bilayer. Grey arrows denote the change in composition upon annealing.

Table 6.2: Quantification of interdiffused material after thermal annealing at 190 °C for 70 hours. All values are calculated against the intensity of the neat material.

	Intermixed signal (%)	
Bilayer	**P3HT**	**P3HS**
L-P3HT / L-P3HS	50	50
L-P3HT / H-P3HS	28	25
H-P3HT / L-P3HS	16	18
H-P3HT / H-P3HS	03	01

Having observed strong difference in the mixing behaviour as a function of molecular weight of the constituting polymers, focus is now turned to the structural evolution on shorter length scales. In order to ascertain whether crystalline regions form in such bilayer structures, as prepared and annealed, we performed grazing-angle incidence wide-angle X-ray scattering (GIWAXS) (Figure 6.3). To this end, we focused on the bilayers that exhibited the most varied mixing behaviour: *i.e.* L-P3HT/L-P3HS and H-P3HT/H-P3HS and exploited the fact that P3HS has an observably larger π-stacking (010) distance and a shorter lamellar stack (100) when compared to P3HT.

In the pristine bilayers, the lamellar peaks are observed along Q_z (*e.g.* ~0.4, 0.8 and 1.2 A^{-1}) as the convolution of two peaks with slight positional offset. This implies that populations of both crystalline P3HT and P3HS are present. Moreover, the pristine L-P3HT/L-P3HS exhibits more edge-on orientation than the H-P3HT/H-P3HS system. Interestingly, the L-P3HT/L-P3HS bilayer feature additional reflections in Q_z at ~0.5 and 1 A^{-1}, which originate from the P3HS (see chapter 7) and have been ascribed to a type-2 crystal form.[18, 19] This crystal form has recently been shown to capriciously develop in oligomeric thiophenes and selenophenes, due to a cross-over of kinetic and thermodynamic preferentiation of the type-1 and type-2 two structures.[10 19]

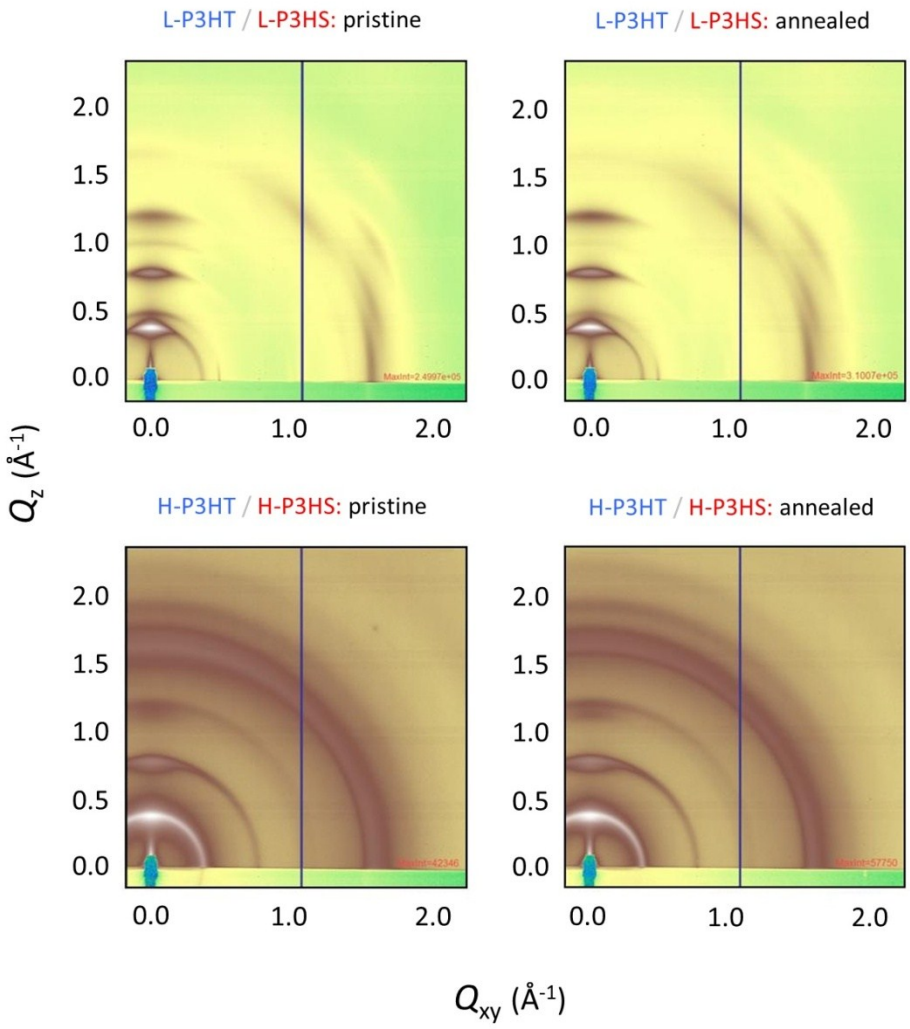


Figure 6.3: Grazing-angle incidence wide-angle X-ray scattering data obtained on P3HT/P3HS bilayers. **Top**: L-P3HT/L-P3HS, **Bottom**: H-P3HT/H-P3HS, pristine (left) and annealed (right) at 190 °C for 70 hours.

Upon annealing clear changes are discernable. Firstly, the L-P3HT/L-P3HS sample exhibits a dramatic reduction of the type-2 crystal reflections, consistent with the instability of this phase at elevated temperatures.[10] It is however also clear that there remain significant populations of crystalline P3HT and P3HS, although it appears that annealing reduces the preferential edge-on orientation of these crystallites.

The H-P3HT/H-P3HS system shows a clear sharpening of the definition between the P3HT and P3HS lamellar peaks, indicating that both materials develop a higher molecular order during annealing because crystallisation of these high molecular weight materials was more hindered

during casting when compared to their low molecular weight counterparts (see also chapter 4). Additionally the orientation of the high-M_w system does not appear to be affected by annealing, likely due to the reduced molecular mobility of these entangled polymer chains.

Clearly, in the case of the H-P3HT/H-P3HS bilayers, distinct layers can be fabricated of a certain degree of crystallinity and aggregation. The effect of annealing appears to result in a small enhancement in crystallinity in addition to diffusion of a minute amount of each material into the other layer. On the other side of the spectrum are the L-P3HT/L-P3HS systems, which exhibit a small fraction of intermixed material already before the heat treatment. Annealing leads to complete vertical mixing of the layers, however this intermixing appears not to affect the degree of crystallinity of either polymer.

The above observations give useful insight into the structural development and miscibility of the selected systems. Gratifyingly, the intermixing of P3HT/P3HS bilayers follows the observed trend expected for samples, in that, increasing the molecular-weight of the materials results in lower intermixing, as predicted by the Flory-Huggins solution theory.[5] A large tendency for intermixing is found for low-M_w pairs (L-P3HT/L-P3HS), which is highlighted by the fact that already at room temperature some interdiffusion occurs and thermal annealing leads to complete vertical intermixing. In strong contrast, high-molecular weight polymers stay more phase pure, but still display a small amount of intermixing, which is believed to be influenced by the polydispersity of the samples.. Annealing leads however to an increase in the degree of crystallinity of the two components. An interim behaviour is found for systems that comprise at least one polymer of relatively low molecular weight, which shows that the degree of mixing can be readily tuned by the selection of polymer. It appears plausible that all samples have attained a diffusion equilibrium after annealing, implying that the diffusion coefficients of the species were high enough to enable the local thermodynamic mixing equilibrium to be attained. The significant mobility of low-M_w materials at ambient temperature raises, however, questions about the structural stability of such blends

when used in solar cells. Detailed information on the structure/property/processing inter-relations of polymer:polymer blends need thus to be established to elucidate the effect of their different mixing behaviour with molecular on device performance as, prepared, annealed and over time.

6.3 Materials and methods

Materials: P3HS and L-P3HT were kindly supplied by Dr. Martin Heeney, Imperial College London. H-P3HT was purchased from Merck chemicals and used as received.

Gel permeation chromatography (GPC): The polymers were dissolved in high-performance liquid chromatography (HPLC) grade chlorobenzene at 10 mg/ml and measured at 80 ^{o}C. The resultant elution times were calibrated against polystyrene standards of known molecular weight distribution to yield the molar mass scale.

Bilayers: were fabricated by spin-coating P3HS 15 mg/ml (from chlorobenzene) at 1200 rpm for 45s onto a first substrate (SiO_2 for D-SIMS and Si for GIWAXS). P3HT was then spin-coated 15 mg/ml at 1200 rpm for 60 s onto a glass substrate that had been previously coated with PSS (5 mg/ml solution in deionised water, spin-cast at 300 rpm for 45 s). The two bilayer component layers were left under vacuum for 48 hours to aid removal of residual solvent. The P3HT film was then floated onto a bath of water and "scooped" up with the P3HS coated substrate. The resultant films were dried under vacuum for 48 hours and then annealed (at 190 ^{o}C, 7hours). These films were then capped with a thin (45 nm) layer of polystyrene (PS). The PS layer was spin-coated onto a silicon substrate at 8 mg/ml from a toleuene solution at 2000 rpm for 45 s. The polystyrene layer was then floated and laminated in a similar fashion to the bilayer production. The polystyrene layer within these samples serves two purposes, firstly it enables the analytical and sputter beams to stablise prior to probing the actual sample. Secondly the intensity of the molecular fragment signals (*e.g.* CH^-) observed in the capping layer can be used to calibrate between different measurements.

Secondary ion mass spectrometry (SIMS) depth profiling: the SIMS presented in this chapter was carried out at the University of California Santa Barbara, USA, using a Physical Electronics Quadropole 6650 – a technique that subtly different in experimental setup to the rest of the SIMS methodologies discussed in this thesis, but capable of yielding similar information. An O_2^+ beam at 2 kV, with current of ~45 nA was rastered over a 200 µm x 200 µm area, of which the central 15% was analysed. Negative ions were collected to ensure sufficient ion yields of both sulphur and selenium could be attained.

Grazing-angle incidence wide-angle x-ray scattering (GIWAXS): measurements were carried out at Beamline 7.3.3. of the Advanced Light Source using a Dectris Pilatus 1M photon counting detector. Samples were measured at an incident angle of ~0.13^o, above the critical angle so the X-ray beam penetrated to the substrate. The photon energy used for GIWAXS was 10 keV. Air scatter which provides a background signal was reduced using helium gas.

6.4 References

1. A. Facchetti, *Materials Today*, 2013, **16**, 123-132.
2. M. M. Wienk, J. M. Kroon, W. J. H. Verhees, J. Knol, J. C. Hummelen, P. A. V. Hal and R. A. J. Janssen, *Angewandte Chemie*, 2003, **115**, 3493-3497.
3. C. R. McNeill, J. J. M. Halls, R. Wilson, G. L. Whiting, S. Berkebile, M. G. Ramsey, R. H. Friend and N. C. Greenham, *Advanced Functional Materials*, 2008, **18**, 2309-2321.
4. X. He, F. Gao, G. Tu, D. Hasko, S. Hüttner, U. Steiner, N. C. Greenham, R. H. Friend and W. T. S. Huck, *Nano Letters*, 2010, **10**, 1302-1307.
5. P. J. Flory, *The Principles of Polymer Chemistry*, Cornell University Press, New York, 1953, ch. 13, pp. 554-558.
6. M. Schubert, D. Dolfen, J. Frisch, S. Roland, R. Steyrleuthner, B. Stiller, Z. Chen, U. Scherf, N. Koch, A. Facchetti and D. Neher, *Advanced Energy Materials*, 2012, **2**, 369-380.
7. E. Zhou, J. Cong, Q. Wei, K. Tajima, C. Yang and K. Hashimoto, *Angewandte Chemie*, 2011, **50**, 2799-2803.
8. F. Van Antwerpen and D. W. Van Krevelen, *Journal of Polymer Science*, 1972, **10**, 2423-2435.

9. E. Ergoz and L. Mandelkern, *Macromolecules*, 1972, **5**, 147-157.
10. F. P. V. Koch, M. Heeney and P. Smith, *Journal of the American Chemical Society*, 2013, **135**, 13699-13709.
11. F. P. V. Koch, J. Rivnay, S. Foster, C. Müller, J. M. Downing, E. Buchaca-Domingo, P. Westacott, L. Yu, M. Yuan, M. Baklar, Z. Fei, C. Luscombe, M. A. McLachlan, M. Heeney, G. Rumbles, C. Silva, A. Salleo, J. Nelson, P. Smith and N. Stingelin, *Progress in Polymer Science*, 2013, **38**, 1978-1989.
12. P. G. de Gennes, *The Journal of Chemical Physics*, 1971, **55**, 572-572.
13. C. Goh, R. J. Kline, M. D. McGehee, E. N. Kadnikova and J. M. J. Fréchet, *Applied Physics Letters*, 2005, **86**, 122110-122110.
14. M. Heeney, W. Zhang, D. J. Crouch, M. L. Chabinyc, S. Gordeyev, R. Hamilton, S. J. Higgins, I. McCulloch, P. J. Skabara, D. Sparrowe and S. Tierney, *Chemical Communications*, 2007, 5061-5063.
15. P. E. Rouse Jr, *The Journal of Chemical Physics*, 1953, **21**, 1272-1280
16. S. S. Zade, N. Zamoshchik and M. Bendikov, *Chemistry - A European Journal*, 2009, **15**, 8613-8624.
17. W. C. Tsoi, D. T. James, E. B. Domingo, J. S. Kim, M. Al-hashimi, C. E. Murphy, N. Stingelin, M. Heeney and J.-s. Kim, *ACS Nano*, 2012, **6**, 9646-9656.
18. T. J. Prosa, M. J. Winokur and R. D. McCullough, *Macromolecules*, 1996, 3654-3656.
19. L. Li, J. Hollinger, A. A. Jahnke, S. Petrov and D. S. Seferos, *Chemical Science*, 2011, **2**, 2306-2310.

Chapter 7

Energy transfer in polymer-polymer binaries

7.1 Introduction

Energy and charge transfer processes are critical phenomena across a range of molecular and macromolecular systems. For example, photosynthesis relies upon efficient energy transfer to channel photons harvested by multiple chromophores to reaction centres.[1] For optoelectronic devices, the ability to frustrate energy transfer is a promising strategy to enable white light emission of certain organic light emitting diodes (OLEDs);[2] while in the case of organic photovoltaic devices, the migration of both energy (excitons) and charges (polarons) are of utmost importance for efficiently generating and extracting charge carriers.

Because of their significance, the ability to control these processes and how they relate to the microstructure of organic photovoltaic devices are vividly discussed topics in the organic electronics field and have given rise to different strategies for device design and fabrication. An illustrative example here is the so-called cascade[3] or sensitized ternary[4-6] solar cell, which is believed to operate by sequential charge transfer steps and can be manipulated partially through tailoring of the energy level offset of the different materials. In addition, a number of studies on the role of energy transfer between different chromophores for photovoltaic applications have shown promising evidence of the positive effects of energy transfer on device performance. For example, Hesse *et al.* observed fluorescence energy transfer between a photo-excited dye and [6,6]-phenyl-C61-butyric acid methyl ester (PCBM), which leads to the enhancement of the power conversion efficiency (PCE) within ternary blends.[7] Furthermore, Honda *et al*. observed rapid energy transfer from poly(3-hexylthiophene-2,5-diyl) (P3HT) to a silicon phthalocyanine derivative (SiPc), within a P3HT:SiPc:PCBM ternary.[8] Thereby, it was suggested that the SiPc resided in an intermixed polymer:fullerene region and facilitated charge transfer, highlighting the perceived importance of microstructure and phase morphology in such blends. The potential role of energy transfer within organic photovoltaic blends, thus, raises interesting questions. The mechanisms by which energy

transfer occurs[9, 10] are, for instance, distinct from that of charge transfer and hence may respond differently to changes in the microstructure (*e.g.* ordering of phases, intimacy of mixing *etc.*).

However, despite the attractiveness of utilising energy transfer within organic photovoltaic blends, there is still no consensus on how the precise nature of the microstructure influences such energy transfer processes. Here we, thus, set out to understand how manipulation of the microstructure in terms of the distribution of the materials, the molecular ordering and phase composition can influence the system's ability to efficiently transfer energy. By employing different processing routes we are able to drastically alter the microstructure of polymer:polymer systems, starting from highly mixed or phase-separated systems, thus providing a valuable tool to investigate the structural origins of energy transfer.

7.2 Results and discussion

To investigate the effects of microstructure and phase morphology on the efficiency of the energy transfer process, a binary system comprised of P3HT and P3HS was selected in this study, which has a number of benefits, both in terms of available processing tools to manipulate the structural features of the two polymers and from an optoelectronic perspective. More specifically, the fact that P3HT and P3HS have similar HOMO levels but different LUMO levels[11] (as shown schematically in Figure 7.1 right) may facilitate energy transfer from the P3HT to P3HS. Another benefit of the P3HT:P3HS system is that there is significant overlap of the emission of P3HT with the absorption of P3HS (shown as the grey shaded region in Figure 7.2). This overlap may facilitate resonance energy transfer (RET),[9] as well as longer-range radiative energy transfer. Furthermore, the complementary absorption spectra of the two polymers (shown in Figure 7.1 left) enable selective excitation. Finally, the selection of a suitable molecular weight for both the P3HT and P3HS can be used as a tool to influence the mixing/demixing behaviour of the two components, as shown in the previous chapter.

Indeed, materials of low molecular weight (M_w of 7.2 and 16 kg/mol for P3HT and P3HS respectively) were selected for the present study as they permit partial interdiffusion of one component into the other.

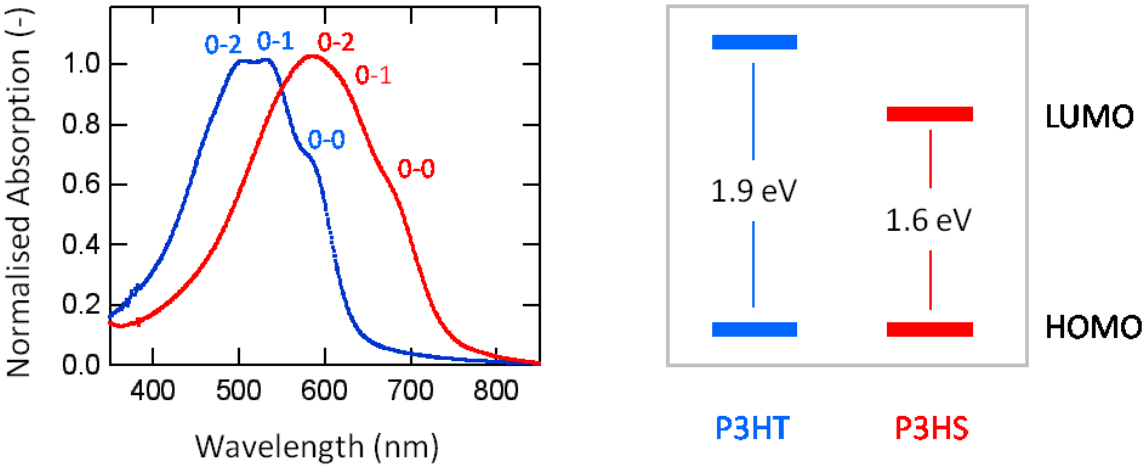


Figure 7.1: Absorption spectra and energy levels of P3HT (blue) and P3HS (red). **Left**: Normalised absorption of the neat P3HT (blue) and P3HS (red) films. The vibronic transitions observable have been labelled for both polymers. **Right**: Energy level diagram of P3HT (blue) and P3HS (red), as previously reported by Heeney *et al*. (reference 11), and the optical bandgap calculated from the absorption spectra, showing the clear reduction in bandgap of around 0.3 eV for the P3HS, which is ascribed to its LUMO position.

Having selected an appropriate pair of materials, we firstly focused on how the distribution and molecular ordering of the two components within binary structures would affect the energy transfer efficiency in such systems. We therefore prepared both laminated P3HT/P3HS bilayers and solution quenched P3HT:P3HS blends and annealed them at 165 °C for 30 minutes. Bilayer fabrication should allow both materials to partly crystallise and aggregate (see previous chapter), limiting interdiffusion during annealing and, hence, resulting in a 3-phase microstructure of relatively phase-pure P3HT and P3HS domains coexisting with an intermixed phase. In contrast co-deposition of P3HT and P3HS from a common solvent can be expected to lead to the formation of kinetically trapped, more intermixed structures.

This picture is confirmed by depth profile SIMS (Figure 7.3). The pristine bilayer displays distinct P3HT- and P3HS-rich layers, although a small amount of intermixing (~2%, based on relative signals) is observed. After annealing, the materials partly intermix as is evident from the enhanced signal of P3HT in the original P3HS layer and vice versa. In the case of the solution-cast blend, the materials are strongly intermixed with some segregation of the P3HT to the substrate and the P3HS to the air interface occurring. Annealing has only a minor effect for this system (dark symbols, Figure 7.3, right), highlighting the stability of the formed solid solution.

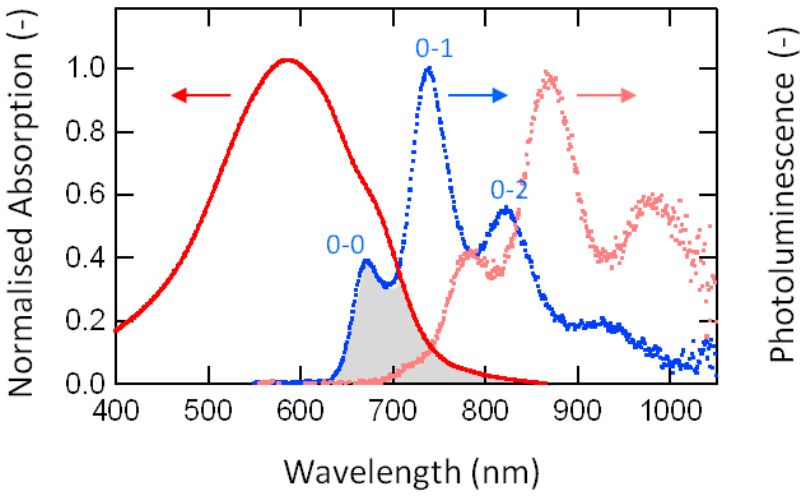


Figure 7.2: Spectral overlap of P3HT and P3HS thin films. Absorption of P3HS thin films: red solid line. Photoluminescence (PL) of neat P3HT and P3HS films: blue and red dotted lines, respectively. The vibronic transitions of P3HT are labelled; the same ascription applies to P3HS. The normalised overlap in P3HT emission and P3HS absorption is shaded grey. PL was measured at 10 K at an excitation wavelength of 405 nm.

These substantial differences in material distribution and phase morphology between P3HT/P3HS bilayers and P3HT:P3HT blends, as-cast and annealed, is supported by the grazing-angle incidence wide-angle X-ray scattering (GIWAXS) data summarised in Figure 7.4 and Table 7.1. In the case of the pristine bilayers, a superposition of reflections corresponding to the neat P3HT and P3HS are observed (Figure 7.4), similar to the bilayers' UV-vis absorption where distinct vibronic features originating from both neat materials are found (Figure 7.5). These findings are in agreement with our

SIMS data that indicates that lamination results in well-defined bilayers with negligible intermixing (Figure 7.3). Partial interdiffusion of the two components during annealing seems to not drastically affect long-range order as essentially identical X-ray patterns are observed for as-prepared and annealed bilayers; however, the evolution of a more pronounced absorption band around 500 nm indicates that on the shorter length scales, P3HT aggregation is disrupted, likely due to the P3HS diffusion into the P3HT layer.

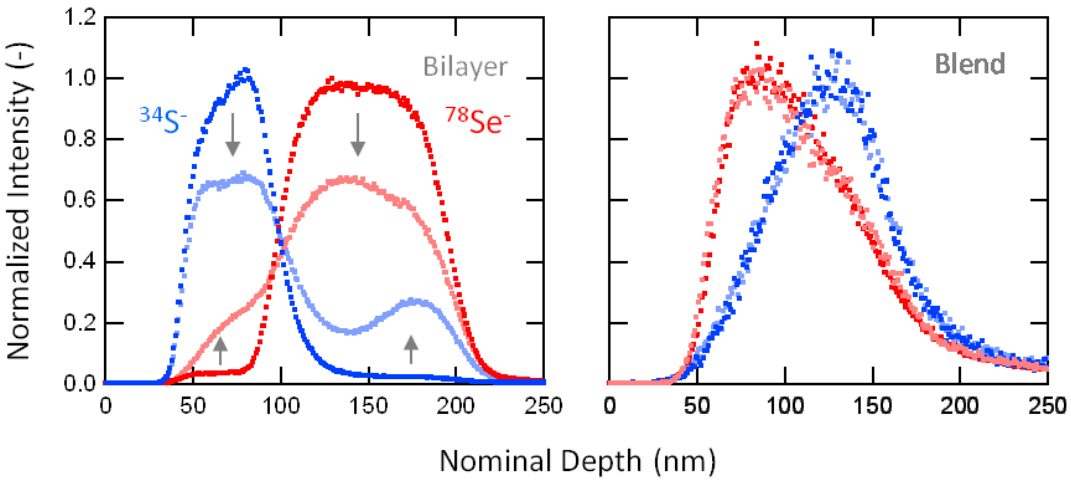


Figure 7.3: Vertical distribution of P3HT and P3HS through a bilayer and a blend thin film, pristine (dark) and after annealing at 165 °C for 30 minutes (light), determined from depth profile SIMS. **Left:** P3HT/P3HS bilayers. Grey arrows denote changes in composition upon annealing. **Right**: Solution-cast P3HT:P3HS blends (1:1 molar ratio).

In strong contrast, a single peak progression is observed in GIWAXS for as-cast P3HT:P3HS blend films (Figure 7.4, orange). The lamellar peaks appear to correlate well with the position of the P3HT reflections suggesting that the crystalline fraction of P3HT:P3HS blends are predominantly comprised of the former material. The vitrifying effect of P3HT on P3HS seems, however, to be limited to long-range order. The UV-vis absorption spectra of the pristine blend (Figure 7.5, left) shows well developed 0-0 transitions for both materials, implying that more local molecular aggregates are indeed present.

Table 7.1: Calculated intermolecular distances and estimated coherence length for neat P3HT, neat P3HS, P3HT/P3HS bilayers and P3HT:P3HS blend films (as-prepared and annealed), extracted from peak position of the (100) and (010) reflections of the two components. The full-width at half maximum (FWHM) was used to estimate the crystallite size using the Scherrer equation (K = 0.9) in the neat and blend systems. Superposition of the respective reflections of the crystalline P3HT and P3HS fractions in the bilayers made such a calculation impossible.

	π-stacking distance (010) (Å)		**Lamellar stacking distance (100) (Å)**		**Crystallite size (nm)**	
	Pristine	Annealed	Pristine	Annealed	Pristine	Annealed
P3HT	3.83	3.82	15.8	15.7	18	25
P3HS	3.92	3.92	15.3	15.2	21	29
Bilayer	3.91	3.91	15.2	15.3	-	-
Blend	3.88	3.93	16.1	16.1	19	20

Having established a structural picture of the various systems, as prepared and annealed, steady-state photoluminescence (PL) was utilised as a tool to deduce from which material emission was originating. Thereby P3HT was preferentially excited (excitation at 405 nm). Such data permits obtaining qualitative information on how the microstructure and phase morphology of binary architectures affect the energy transfer of P3HT to P3HS. The neat materials show a well-defined vibronic progression, with the 0-1 emission at 730 nm dominating the spectra (Figure 7.5, top right panel). Excitation of the pristine bilayer (dark green) leads to a photoluminescence response dominated essentially entirely by the P3HT emission. Cleary, in this highly phase separated system, energy transfer –not surprisingly– is completely frustrated.

Interestingly, partial intermixing during annealing of the bilayers (as observed in SIMS) starts to open energy transfer pathways, deduced from the increased contribution of the P3HS emission, although, a large portion of emission still occurs from the P3HT. The latter observation is supported by the fact that P3HT:P3HS blends, as-cast and annealed, exhibited emission originating solely from P3HS. Clearly, the more the two polymers are intermixed, the more energy is efficiently transferred to P3HS after excitation of the P3HT. In fully intermixed samples, no emission is observed from the P3HT. Our results, thus, strongly imply that the intimacy of mixing dominates the efficiency of energy transfer.

The degree of crystallinity and aggregation of the two components seem less critical since the P3HT fraction was of a similar state of order in all systems, both on long and short length scales; hence, the difference in optoelectronic response we observe cannot be explained on such structural arguments.

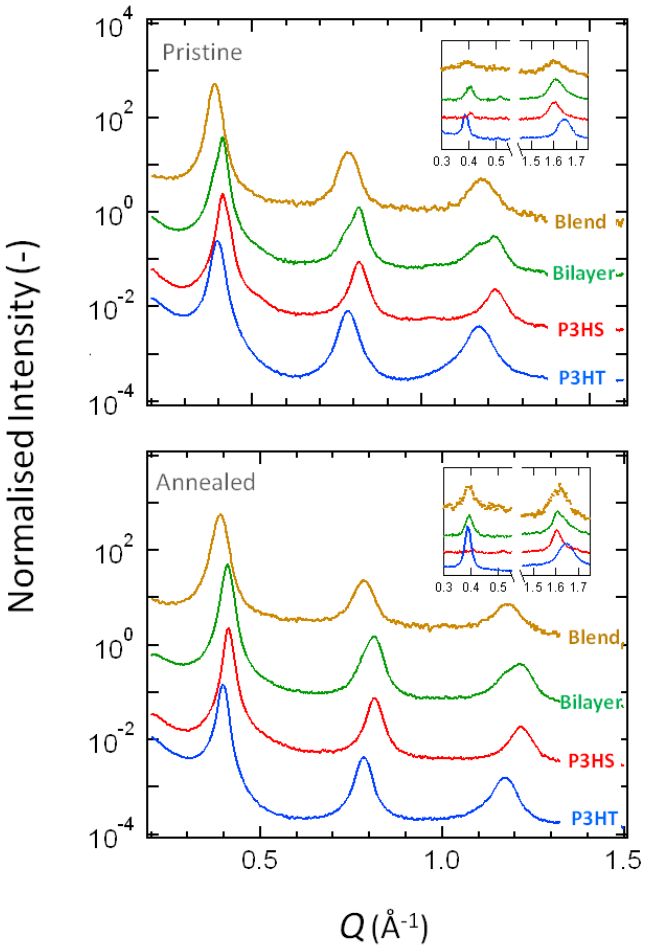


Figure 7.4: Grazing-angle incidence wide-angle X-ray scattering of neat P3HT (blue) and P3HS (red) films, P3HT/P3HS bilayers (green) and P3HT:P3HS blends (orange). The scattering intensity is plotted as a function of *Q*-space. **Top**: Pristine samples. **Bottom**: Samples annealed at 165 °C for 30 minutes. Insets show the corresponding in-plane integration, Q_{xy}. The plots displayed were calculated from the 2D scattering intensity plots in *Q*-space. Line profiles of for the vertical (Q_z direction at $Q_{xy} = 0$ – main figure) and horizontal (Q_{xy} direction at $Q_z = 0$ – inset figure) were taken.

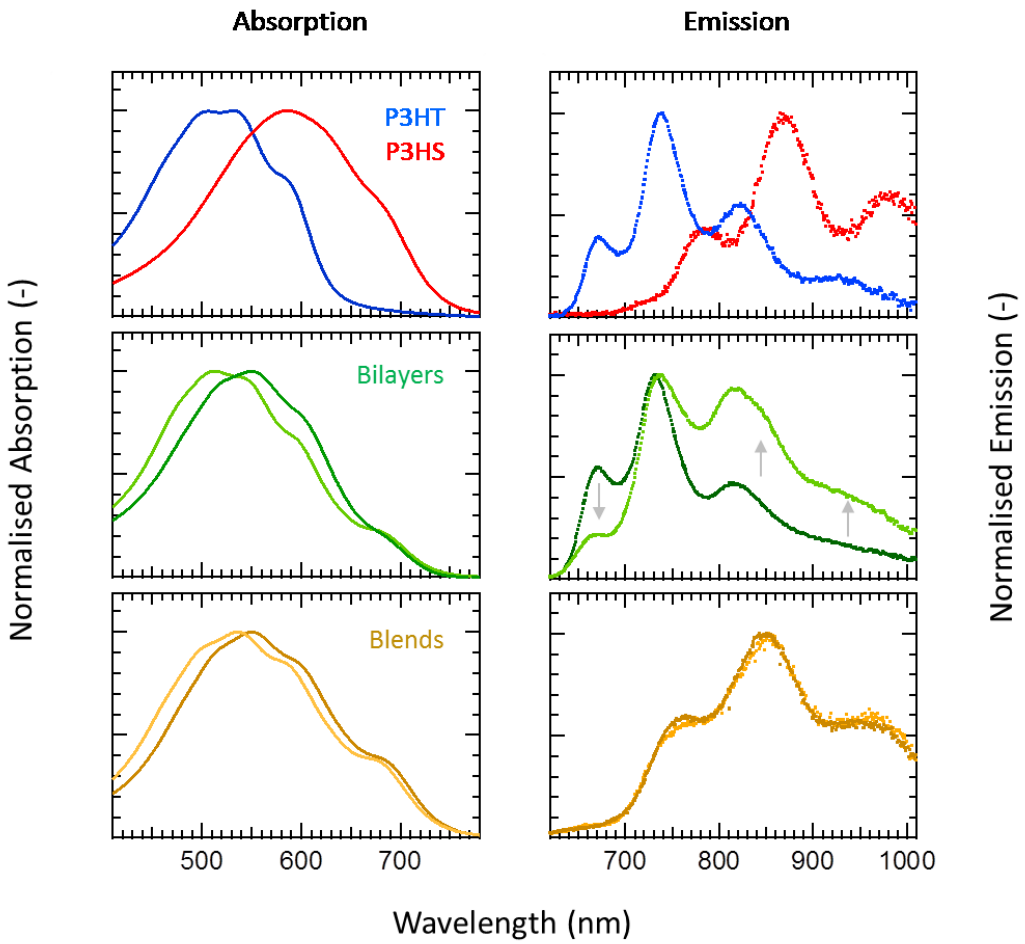


Figure 7.5: Normalised UV-Vis absorption (left) and photoluminescence (PL) (right) spectra of neat P3HT, neat P3HS, P3HT/P3HS bilayers and P3HT:P3HS blends. **Top**: Neat materials: P3HT (blue), P3HS (red). **Middle**: Bilayers: pristine (dark green) and annealed at 165 °C for 30 minutes (light green). **Bottom**: Blends: pristine (dark orange) and annealed (yellow). For PL measurements, all samples were excited at 405 nm and spectra recorded at 10 K to better resolve the vibronic structures allowing differentiation between the emission features of P3HT and P3HS.

The sole emission from P3HS in the solution cast blend of P3HT:P3HS is even more striking when we consider a similar binary system, which is also comprised of P3HT, blended in that case with the fullerene PCBM. In Chapter 4, we have, for instance, shown that the semicrystalline nature of P3HT, leading to a certain degree of phase segregation, limits the exciton quenching efficiency of such blends, as a fraction of excitons radiatively decayed before reaching a donor-acceptor interface (molecular or at domain boundaries). This radiative decay is a significant loss mechanism in P3HT:PCBM OPVs. In strong contrast, in the P3HT:P3HS system discussed here, no emission is observed from the P3HT suggesting that the process of energy transfer from P3HT to the lower

bandgap P3HS may provide a more efficient pathway for photovoltaic light conversion, when compared to the charge transfer processes occurring in P3HT:PCBM blends.

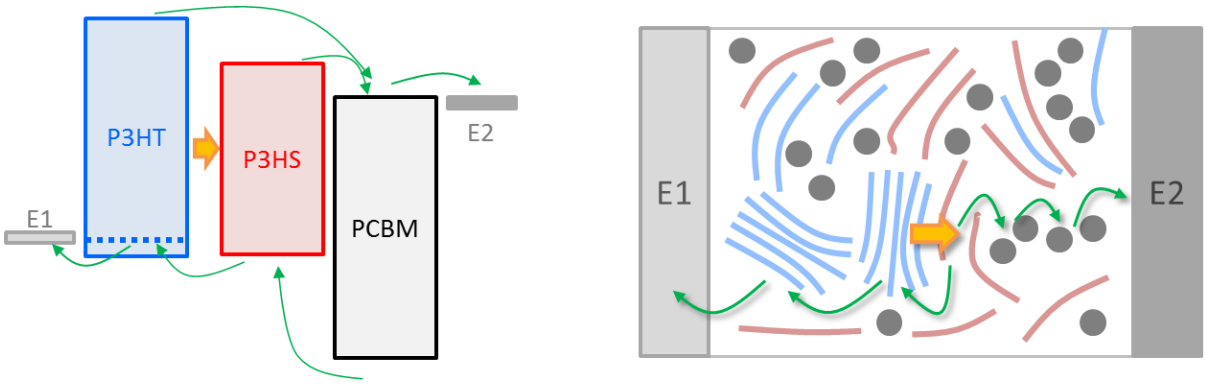


Figure 7.6: Energy level diagram and structural schematic showing the proposed mechanism for operation of a ternary OPV incorporating an energy transfer step. Two *p*-type materials such as P3HT (blue) and P3HS (red) are in this model blended with an *n*-type material (such as PCBM, shown in grey). **Left**: Proposed mechanism depicting the energy transfer step between P3HT and P3HS (orange). **Right**: Structural schematic depicting the energy transfer from the P3HT to P3HS, thereby mitigating the radiative loss pathway commonly observed in P3HT:acceptor blends.

Considering that efficient energy transfer from P3HT to P3HS can be realised, it may be possible to exploit this phenomena in a photo-excitation scheme as proposed in Figure 7.6. This scheme exemplifies a materials system displaying considerable energy transfer from an energy donor to an energy acceptor (orange arrow), as observed between P3HT (blue) and P3HS (red). If an electron accepting species, *e.g.* PCBM, is included in such a theoretical scheme this component would accept the electron from the energetically excited energy acceptor (here, the P3HS). In this hypothetical system, intimacy of mixing between the latter two components is necessary. This can be expected to occur for P3HS and PCBM because PCBM had been shown to have a significantly higher miscibility in P3HS when compared to P3HT.[12] Also, in P3HT:P3HS blends, P3HS crystallisation seems frustrated, which should lead to a good intermixing with the fullerene. Furthermore, the similar HOMO levels of P3HT and P3HS may facilitate charge separation, with the positive polarons being “funnelled” into the ordered fractions of the P3HT (Figure 7.6, blue dashed line). Such a

mechanism has previously been reported to provide a driving force for charge generation,[13, 14] thereby resulting in extraction of the charge carriers to their respective electrodes (denoted E1 and E2).

7.3 Conclusions

The efficiency of energy transfer between P3HT and P3HS was found to vary drastically with the intimacy of mixing between the energy donor and energy acceptor. In the case of the highly intermixed, solution-cast blends, emission occurred solely from the P3HS, indicative of efficient energy transfer between the two materials in such architectures. In contrast, pristine bilayer with little –if any—intermixing showed emission solely from the P3HT as a consequence of minimal energy transfer between the two components. The annealed bilayer where some but not complete intermixing occurred showed a 'composite' emission occurring from both the P3HT and P3HS. These findings strongly imply that the molecular intermixing where the two components are in close proximity is critical to enable efficient energy transfer.

The total absence of emission from P3HT in P3HT:P3HS blends is interesting when comparing their behaviour with the one of the somewhat analogous system of P3HT:PCBM. Both systems exhibit crystalline (or at least aggregated) moieties of P3HT that coexists with finely intermixed domains. In the P3HT:PCBM system, the polymer crystallites (aggregates) limit the blends ability to quench all excited states created from absorbed photons (as seen in chapter 4). This reduced exciton harvesting can constitute a significant loss mechanism in P3HT:PCBM OPV devices. In stark contrast, in the case of P3HT:P3HS blends, no emission is observed from the P3HT implying all energy is transferred to the P3HS. This mechanism of energy transfer may, thus, be employed as a process to more efficiently extract the energy of photo-excitations when compared to that of charge transfer. Indeed, efficient energy transfer occurs from P3HT to P3HS with no radiative loss which should open a strategy for improved photon-harvesting within a ternary donor:donor:acceptor structure, where

light is harvested by an energy donor, efficiently funnelled via energy transfer to an energy acceptor, and subsequent charge transfer from the latter species to an electron accepting material. The difference in mechanisms of energy and charge transfer processes, may allow for new molecular architectures and materials combinations to be realised for efficient harvesting of absorbed photons, thereby opening up new possibilities for the field of organic photovoltaics.

7.4 Materials and methods

Materials: L-P3HS and L-P3HT were kindly supplied by Dr. Martin Heeney, Imperial College London and used as received.

Blend film fabrication: blend solutions (15 mg/ml, total solute concentration in chlorobenzene) were created at a mass ratio of 1:1.2 (P3HT:P3HS) to provide approximately equivalent molar concentrations. The solutions were dissolved for 2 hours at 100 ^{o}C in the dark. Solutions were spin-coated (1200 rpm, 45 s) from hot solutions.

Bilayers: were fabricated by spin-coating P3HS 15 mg/ml (from chlorobenzene) at 1200 rpm for 45s onto a first substrate (SiO_2 for D-SIMS and Si for GIWAXS and glass for UV-vis and PL measurements). P3HT was then spin-coated 15 mg/ml at 1200 rpm for 60 s onto a glass substrate that had been previously coated with PSS (5 mg/ml solution in deionised water, spin-cast at 300 rpm for 45 s). The two bilayer component layers were left under vacuum for 48 hours to aid removal of residual solvent. The P3HT film was then floated onto a bath of water and “scooped” up with the P3HS coated substrate. The resultant films were dried under vacuum for 48 hours and then annealed (at 160 ^{o}C, 30 minutes). The D-SIMS samples were then capped with a thin (45 nm) layer of polystyrene (PS). The PS layer was spin-coated onto a silicon substrate at 8 mg/ml from a toleuene solution at 2000 rpm for 45 s. The polystyrene layer was then floated and laminated in a similar fashion to the bilayer production. The polystyrene layer within these samples serves two purposes,

firstly it enables the analytical and sputter beams to stablise prior to probing the actual sample. Secondly the intensity of the molecular fragment signals (*e.g.* CH^-) observed in the capping layer can be used to calibrate between different measurements.

UV-Vis absorption: All measurements reported in this thesis utilised a Perkin-Elmer Lambda 35 spectrophotometer, an increment of 1 nm and acquisition rate of 980 nm/min. Displayed data are (1 – transmission) and therefore encompass both absorption and scatter.

Photoluminescence: All measurements reported utilised a Horiba Spex Fluormax-1 spectro-fluorometer with an acquisition angle of 60^o. Slit widths were set at 5 nm, and an excitation wavelength of 520 nm was used.

Depth profile secondary ion mass spectrometry (D-SIMS): An Ion TOF 5 SIMS was used to measure depth profiles of bilayer samples. All samples were sputtered using a 1kV Cs^+ (~75 nA) beam across a 250 x 250 µm square. Analysis was carried out using a Bi_3^+ (~1 pA) beam over the central 50 x 50 µm region of the sputter crater with charge compensation and negative ions were collected.

Grazing-angle incidence wide-angle x-ray scattering (GIWAXS): measurements were carried out at Beamline 7.3.3. of the Advanced Light Source using a Dectris Pilatus 1M photon counting detector. Samples were measured at an incident angle of ~0.13^o, above the critical angle so the X-ray beam penetrated to the substrate. The photon energy used for GIWAXS was 10 keV. Air scatter which provides a background signal was reduced using helium gas.

GIWAXS analysis of binary systems: prior to analysing the binary systems the neat materials (P3HT, blue) and (P3HS, red) were analysed. Both neat materials appear to crystallise during solution casting as deduced from the clearly discernable lamellar (100) and π-stack reflections (010). The crystallite sizes were estimated using the Scherrer equation as modified for a plate detector using Equation 7.1:

$$D_{\mathrm{hkl}} = {2\pi K}/{\Delta q_{\mathrm{hkl}}} \qquad \textit{Equation 7.1}$$

where, D_{hkl} is the is the average grain size, K is the Scherrer constant (here fixed at 0.9 to enable relative comparison) and Δq_{hkl} is the peak broadening.[15]

7.5 References

1. E. Collini, C. Y. Wong, K. E. Wilk, P. M. G. Curmi, P. Brumer and G. D. Scholes, *Nature*, 2010, **463**, 644-647.
2. B. W. D'Andrade, R. J. Holmes and S. R. Forrest , *Advanced Materials*, 2004, **16**, 624–628
3. T. Ameri, J. Min, N. Li, F. Machui, D. Baran, M. Forster, K. J. Schottler, D. Dolfen, U. Scherf and C. J. Brabec, *Advanced Energy Materials*, 2012, **2**, 1198-1202.
4. M. Koppe, H.-J. Egelhaaf, G. Dennler, M. C. Scharber, C. J. Brabec, P. Schilinsky and C. N. Hoth, *Advanced Functional Materials*, 2010, **20**, 338-346.
5. a) S. Honda, T. Nogami, H. Ohkita, H. Benten and S. Ito, *ACS Applied Materials & Interfaces*, 2009, **1**, 804-810. b) S. Honda, H. Ohkita, H. Benten and S. Ito, *Advanced Energy Materials*, 2011, **1**, 588-598.
6. J. A. Mikroyannidis, D. V. Tsagkournos, S. S. Sharma, A. Kumar, Y. K. Vijay and G. D. Sharma, *Solar Energy Materials and Solar Cells*, 2010, **94**, 2318-2327.
7. H. C. Hesse, J. Weickert, C. Hundschell, X. Feng, K. Müllen, B. Nickel, A. J. Mozer and L. Schmidt-Mende, *Advanced Energy Materials*, 2011, **1**, 861-869.
8. S. Honda, S. Yokoya, H. Ohkita, H. Benten and S. Ito, *The Journal of Physical Chemistry C*, 2011, **115**, 11306-11317.
9. T. Förster, *Radiation Research Supplement*, 1960, **2**, 323-339.
10. S. Reineke, F. Lindner, G. Schwartz, N. Seidler, K. Walzer, B. Lüssem and K. Leo, *Nature*, 2009, **459**, 234-238.
11. M. Heeney, W. Zhang, D. J. Crouch, M. L. Chabinyc, S. Gordeyev, R. Hamilton, S. J. Higgins, I. McCulloch, P. J. Skabara, D. Sparrowe and S. Tierney, *Chemical Communications*, 2007, 5061-5063.

12. N. D. Treat, A. Varotto, C. J. Takacs, N. Batara, M. Al-Hashimi, M. J. Heeney, A. J. Heeger, F. Wudl, C. J. Hawker and M. L. Chabinyc, *Journal of the American Chemical Society*, 2012, **134**, 15869-15879.

13. E. Buchaca-Domingo, A. J. Ferguson, F. Jamieson, T. McCarthy-Ward, S. Shoaee, J. R. Tumbleston, O. G. Reid, L. Yu, M.-B. Madec, M. Pfannmöller, F. Hermerschmidt, R. R. Schröder, S. E. Watkins, N. Kopidakis, G. Portale, A. Amassian, M. Heeney, H. Ade, G. Rumbles, J. Durrant and N. Stingelin, *Materials Horizons*, 2013, DOI:10.1039/C1033MH00125C.

14. F. C. Jamieson, E. B. Domingo, T. McCarthy-Ward, M. Heeney, N. Stingelin and J. R. Durrant, *Chemical Science*, 2012, 485-492.

15. D.-M. Smilgies, *Journal of Applied Crystallography*, 2009, **42**, 1030-1034.

Summary

Organic semiconducting binaries present an interesting class of materials systems, which promise vast impact across a range of functional devices including solar cells and light emitting diodes. The complex interactions between the two materials allow for vast raft of microstructures to develop, terminally leading to dramatically different optoelectronic properties. For example, the ability of such systems to efficiently photo-generate charges was shown in this thesis to be highly dependent upon a delicate balance of intermixed and more phase-pure domains within the active layer. The balance between these phases was tuned via materials selection*, i.e*. polymers of varied molecular weight and fullerenes with different vitrifying effects.

Furthermore, manipulation of the microstructure was achieved here through variation of the processing route, thereby allowing structural formation processes to proceed to differing extents. For instance, in bilayer systems, aggregation and crystallisation of the polymer typically occurred to a greater degree (shown to limit the exciton quenching) compared to solution cast blends where the addition of the fullerene has a strong vitrification effect. Moreover, energy transfer between two different semiconducting polymers was demonstrated to correlate to the specific processing route followed, whereby highly efficient or highly frustrated transfer was achieved depending on the deposition technique selected.

In summary, in this thesis the optoelectronic properties of organic semiconducting binaries were shown to be inseparably linked to the processing route employed, and the subsequent microstructure evolved and different factors in the deposition of organic semiconductors have been inter-related to providing guidelines to aid the rational enhancement of such systems, from a bottom-up approach.

Curriculum vitae

Paul Westacott was born in Leicester, United Kingdom in 1986. After completing high-school at Groby College, he undertook a Bachelors of Science degree in Chemistry at the University of Nottingham, where he received a First class degree, as the third highest graduate of the year. After spending a year founding the *Charnwood Chilli Company*, he joined the group of Dr. Natalie Stingelin within the Centre for Plastic Electronics and Department of Materials at Imperial College London. He was awarded a scholarship as part of the first cohort of students within the Centre for Doctoral Training and in 2010 he received a Masters of Research (MRes) degree in Plastic Electronics with Distinction, finishing as the top graduate of 2010. For there on, he continued working in the research group of Dr. Stingelin, where he carried out the research presented in this thesis. Following his Ph.D. Paul began work within the Imperial Centre for Energy Policy and Technology investigating the impact of solar PV within the UK.